Influence of a PV insulation layer on the point load distribution of corrugated roofs

31/ 08 / 2023

Thesis committee

Prof.dr. Milan Veljkovic, TU Delft
Dr. Florentia Kavoura, TU Delft
Dr. Anis Mohabeddine, TU Delft
Dr.ir. P.C.J. (Pierre) Hoogenboom, TU Delft
Ir. Vladimir Škorić, ASK Romein
Ir. Goran Pavlovic, ASK Romein

Author

Abdulrazzak Al-Sharqi
4347854

Abstract

This research aims to investigate the influence of Polyisocyanurate (PIR) insulation on small surface load distribution on corrugated steel roofing sheets. PIR foams are used for thermal insulation in industrial buildings. The distribution of surface loads induced by solar panels support structure might be altered by PIR foams. This is completely ignored in the design calculations according to current standard which might results in overconservative designs. In this study, the following main question is going to be investigated using experimental and numerical methods: ‘’What is the influence of PIR insulation on the transverse distribution of small surface loads on corrugated steel roofing sheets?’’

The methodology involves conducting bending experiments to obtain strains and deflection data, which then are validated using numerical models. The experiments have been conducted on corrugated steel sheets supported by rollers. The PIR insulation is connected to the steel sheet by bolts, and a loading cylinder applies vertical force at the PIR insulation panel side. Two loading configurations are selected to simulate the representative loading conditions in real-life structures. Vertical deflections and strains in the bottom flanges of the corrugated sheet are measured during the experiments. The experimental data are used for the validation of the numerical models that are created by using ABAQUS FEA.

First, a linear F.E Model was developed and validated with experimental results up to the initiation of nonlinearities. The results of the linear models shows clearly that the PIR layer influence considerably the stress distribution in the adjacent ribs to the one of load application. A nonlinear analysis is conducted to determine the maximum load that the roof structure can resist. To capture geometrical nonlinearities more accurately, eigen buckling analysis was conducted to implement initial geometrical imperfections. Considering the imperfect initial geometry of the steel sheet and its plastic properties, maximum strength of the roof system could be estimated. As a note, the damage in the PIR insulation material was not considered as it is beyond the scope of this study, the material was assumed to be linear elastic.

The experiments demonstrate that the behaviour of the roof structure is primarily governed by the rupture of the PIR insulation, occurring prior to any yielding in the steel sheet. The linear numerical model predicts the behaviour of the roof structure within the elastic phase. The linear model can be used to study the influence of the several influencing parameters such as the dimension, PIR material properties and the loading conditions. Expanding the span from 2 to 6 meters with a single mid-span surface load increases the adjacent rib contribution by 20%, meaning that their normalized strain values relative to the load location's maximum strain grow by 20% in the elastic phase. The nonlinear model is employed to establish the force vs. displacement curve and identify the strength of the roof. The non-linear numerical models show that the ultimate load is found to be 8000 N when a single surface load is applied directly on the steel sheet. The experiments show yielding of the steel at 7300 N after the loading jack ruptures both the PIR surface and layer, then the jack reaches the profiled steel sheeting. For design purposes, it is recommended to exclude the influence of the PIR insulation beyond its elastic phase. Compression tests conducted on the specimen revealed damage within the PIR material at a load of 6250 N, which is considered the upper limit for the PIR's elastic phase.

Dedicated to my family.

Acknowledgements

This thesis was completed as the final requirement for the Master of Science in Civil Engineering program at Delft University of Technology. I am proud to have successfully accomplished finishing this thesis. I extend my gratitude to all my supervisors, whose guidance was instrumental in bringing this research to fruition. Without your invaluable assistance, this achievement would not have been possible.

I express my sincere appreciation to Dr. Florentia Kavoura for her weekly supervision, feedback, and teaching during challenging times. These experiences taught me a great deal and I am truly thankful. Her understanding of my scheduling conflicts arising from exams conducted concurrently with this research and experiments was remarkable. My heartfelt thanks go also to Dr. Anis Mohabeddine for his substantial contributions. I have gained invaluable insights into effective problem-solving through his mentorship. He has helped me a lot with the software ABAQUS and without his tips and guidance this would have not been possible. I also wish to acknowledge Dr. Pierre Hoogenboom for his insightful feedback and wealth of knowledge that provided new perspectives on problem-solving. Even brief feedback from him opened my eyes to alternative approaches and solutions. Professor Milan Veljkovic, I extend my appreciation for your expertise and constructive feedback. Your encouragement motivated me to deliver my best. Thank you for pushing me and help me to grow as a person and as a future engineer too.

I am grateful to Vladimir and Goran from ASK Romein, who generously shared crucial information that shaped this work. While unfortunate circumstances prevented us from completing the project together due to ASK Romein's bankruptcy, I hope you find satisfaction in the results of this research.

I would also like to thank the lab members – Giorgos, John, and my mentor Louis den Breejen – for their patience and extensive guidance. Louis, your diligent efforts in constructing the experimental setup and ensuring its accuracy were truly appreciated. Your mentorship enriched my lab experience, making it both enjoyable and informative.

Lastly, my heartfelt gratitude goes to my family for their unwavering support during both good and challenging times. This achievement is dedicated to you and your steadfast belief in me during my whole life. I can’t thank you enough for the daily support you have given me. I also want to extend my appreciation to my friends, who supported me throughout my academic journey at TU Delft, from my bachelor's to my master's degree. To those who have already graduated and to those embarking on their thesis journeys, I offer my best wishes from the bottom of my heart. May we celebrate your graduations next year with joy and pride!

Contents

1 Introduction

1.1 Context

Solar panels have become an increasingly popular source of renewable energy worldwide, including in the Netherlands. The Dutch government has also committed to the European Union's climate agreement, which aims to make the EU climate-neutral by 2050. As part of this agreement, the Netherlands has set ambitious targets to reduce greenhouse gas emissions and increase renewable energy production. The country has made significant strides in solar panel adoption, thanks to government policies, subsidies, and a growing interest in sustainable energy solutions (International Energy Agency, 2021).

Moreover, as a very dense country, space efficiency is a significant concern for the Netherlands. Thus, solar panels can provide a solution to generate electricity while optimizing the land use. Photovoltaic (PV) panels are increasingly being installed on flat roofs to meet the growing demand for green energy. This particularly relevant for steel industrial buildings which features large areas which is the focus of this study.

Solar panels can be integrated into the design of new buildings or added to existing ones as a retrofit. The placement of solar panels on rooftops can have a significant impact on the design process of the buildings. For example, the orientation and slope of the roof must be optimized to maximize the efficiency of the solar panels. Additionally, the load-bearing capacity of the roof must consider this additional point load and ensure that it can support this additional weight generated from the solar panels.

Several questions from engineers have been raised regarding the distribution of these loads and their implementation on a real-life structural analysis. Until now there has been a lack of research focusing on this matter. This thesis aims to fill this gap through experimental and numerical simulations of the representative roofing structure that consists of corrugated steel sheets and PIR insulation.

1.2 The roof-structure

Corrugated steel sheet roofing is a construction material used in various settings such as agricultural, industrial, and residential buildings due to its durability, ease of installation, and affordability. Similarly, corrugated plates are widely used in construction, particularly in decking, roofing, and sandwich plate core structures. On the other hand, PIR insulation is widely used in walls, roofs, floors, and ceilings of residential and commercial buildings, thanks to its high thermal resistance and low thermal conductivity. Polymeric foams are highly efficient thermal insulation materials due to the low thermal conductivity of the blowing agent gases that are trapped within their closed porous structures. The thermal conductivity of polyurethane and polyisocyanurate foam is one of their most notable properties, making them a popular choice for insulation (H. Zhang, 2017).

Multiple rubber feet are used in the detail of the support of the PV panels, so that the weight from the PV panels is applied as small surface loads on the top of the roof. These small surface loads include the self-weight of the PV panels, the weight of the ballast (concrete tiles), and the weight of any snow accumulation on the panels. The small surface loads applied on the roof must be carefully considered to ensure that the load capacity of the roof is not exceeded. An example of the PV panel on a roof top is shown in Figure 1.

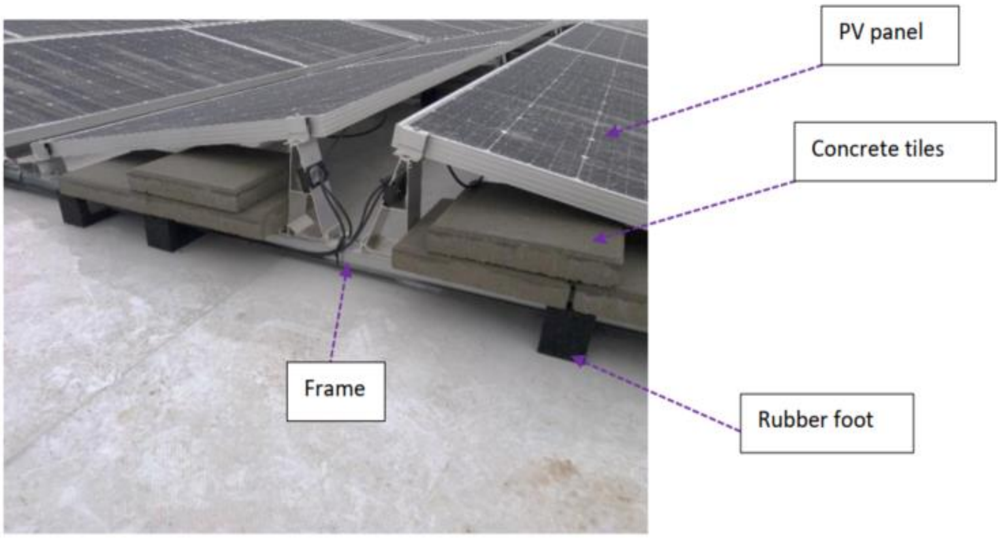

Figure 1 Placement of PV panel on the roof (ASK Romein, 2020).

1.3 Problem statement and research questions

In steel industrial buildings, corrugated steel sheets with PIR insulation, connected on the top of them by screws, are commonly adopted as a roofing system. PV panels are installed on the top of the PIR as shown in Figure 1. The PV panels apply small surface loads through multiple rubber feet on the roof structure. In current design practice, the point loads are applied without considering that a thick PIR might distribute the load on a rather larger area. This might lead to an overdesign and material waste as this issue was already raised by practitioners.

In this study, the following main question is going to be investigated using experimental and numerical methods:

‘’What is the influence of PIR insulation on the transverse distribution of small surface loads on corrugated steel roofing sheets?’’

To simplify the process of answering this main research question, it is necessary to divide this question into sub-questions.

1. “What are the variables that affect the load distribution in the steel sheeting due to the presence of PIR insulation?”

2. “What is the distribution angle of the load in the PIR insulation?”

3. “What are the failure criteria and what is the considered failure load of the roof structure?

1.4 Research approach

This study focuses on investigating the impact of PIR insulation on the transverse distribution of small surface loads on corrugated steel roofing sheets. To accomplish this objective, the study is structured around the following goals:

- Experimental research: Conducting bending tests to obtain the transverse load distribution in the steel sheet.

- Linear numerical model development: Creating a linear model and validating it using the experimental results.

- Using the linear model: Extending the analysis to longer spans to obtain results for the linear model.

- Nonlinear model development: Developing a nonlinear model with initial imperfections to establish the force vs. displacement curve in the steel sheet and determine the strength of the roof.

By addressing these objectives, the study aims to gain a detailed understanding of the influence of PIR insulation on the load distribution and structural behaviour of corrugated steel roofing sheets.

1.5 Thesis outline

To address the main research question and sub-questions, literature review is conducted to examine previous studies on load distribution in corrugated steel sheets and how to model the roof structure. Following that, the details of experiments conducted on a specific roof structure composed of a steel sheet and PIR insulation are presented to investigate whether small surface loads cause transverse distribution in the steel sheet. The experiments reveal the overall behaviour of the steel sheet and the PIR insulation along with their failure mechanism which differ for the two loading conditions.

A numerical model is then developed to simulate the geometry, boundary conditions, and loading of the experiment. The model is developed using ABAQUS FEA, a finite element software that predicts the distribution of loads in the corrugated steel sheet. The numerical model's results are compared to the experimental results to validate them. After the validation process for elastic properties, the model is then generated with the plastic properties in the steel sheet. Imperfections are also assumed in the steel sheet by taking a magnitude of a buckling mode shape resulting from axial compression. This magnitude of the buckling mode shape is introduced as an initial imperfection in the steel sheet, allowing for a new geometry considering imperfections.

After this, a post-buckling analysis is performed by applying the small surface load. Variables such as loading, span, or material properties can be modified in the numerical model to observe the distribution of load among the ribs of the corrugated steel sheet. The thesis concludes with discussions and answers to the research questions, summarizing the findings from the experiments, and numerical modelling. This research enhances the understanding of load distribution in corrugated steel sheets and provides valuable insights for designing and analysing roof structures.

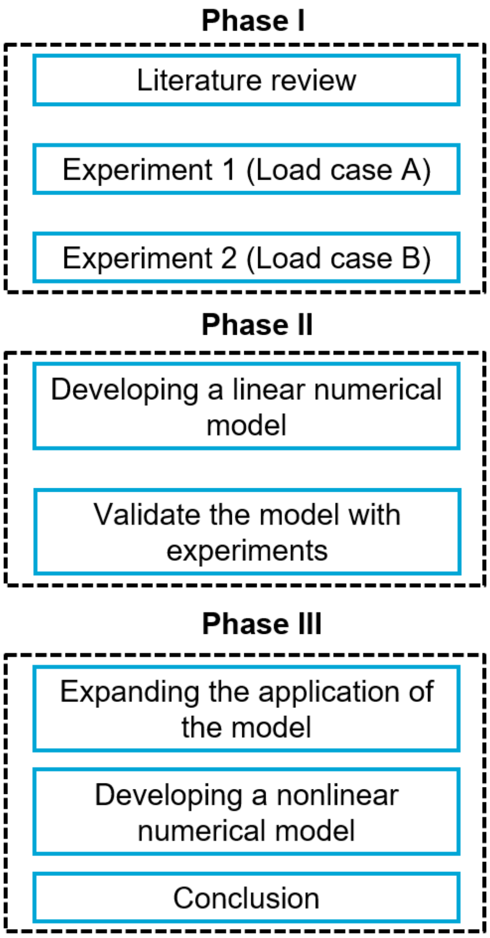

Figure 2 Thesis outline.

2 Literature study

The problem statement highlights the limited research available on load distribution in roof structures. Developing an accurate model for the steel and PIR insulation requires a comprehensive understanding of how cold-formed sheets are applied in real-structure scenarios and the material properties of PIR insulation. Modelling corrugated steel sheets in FEM software presents challenges due to real-structure imperfections not included in the model. The cold-formed steel sheets do not possess perfect geometry due to the rolling manufacturing process. Furthermore, the thinness of the cold-formed steel amplifies the impact of slight imperfections, leading to unsymmetrical outcomes. This chapter reviews relevant studies for understanding the behaviour of roof structures and to create a valid model. It explores aspects such as modelling the roof structure, identifying steel sheet imperfections, incorporating assumptions about imperfections, and considering the material properties of PIR insulation.

2.1 Orthotropic models of corrugated sheets in Finite element analysis

Corrugated sheets are widely used in various engineering applications, including roofing and shipbuilding. Analysing the behaviour of these sheets can be challenging, especially when using the finite element (FE) method, which requires significant computational effort. To address this issue, an alternative approach is to treat the structures as orthotropic plates with equivalent rigidity and stiffness. Previous investigations on trapezoidal corrugated sheet equivalent orthotropic plates have focused mainly on stability issues and flexural rigidity. Samanta & Mukhopadhyay (1997) covered static and dynamic analyses of trapezoidal corrugated sheets have been conducted based on equivalent orthotropic models that consider both extensional and flexural rigidities.

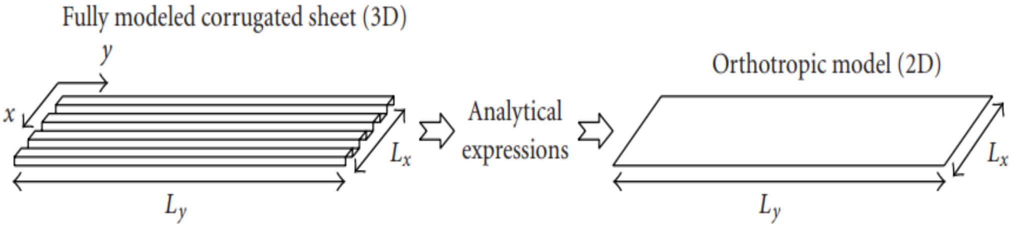

Figure 3 Modelling corrugated sheets as orthotropic plate (Samanta & Mukhopadhyay, 1997).

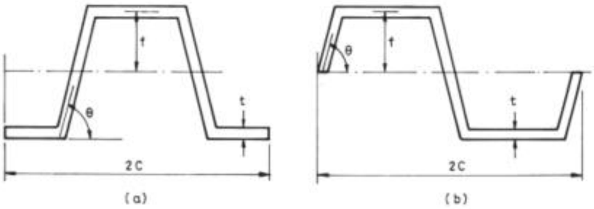

Figure 4 Corrugation of the steel sheet (Samanta & Mukhopadhyay, 1997).

Several examples were presented for trapezoidal corrugated sheets with varying numbers of corrugations and trough angles (Samanta & Mukhopadhyay, 1997). Table 1 shows the comparison of the central displacements of the shell model and the orthotropic model with different boundary conditions, number of corrugations and trough angle (Samanta & Mukhopadhyay, 1997). The results of the comparison between the two approaches are improved with an increase in the number of corrugations and trough angle. The applied boundary conditions are shown in Figure 5. The proposed approach is applicable to any trough angle and boundary conditions and can be extended to any type of corrugation (Samanta & Mukhopadhyay, 1997).

Table 1 Comparison of central displacements (cm) between shell and orthotropic model (Samanta & Mukhopadhyay, 1997)

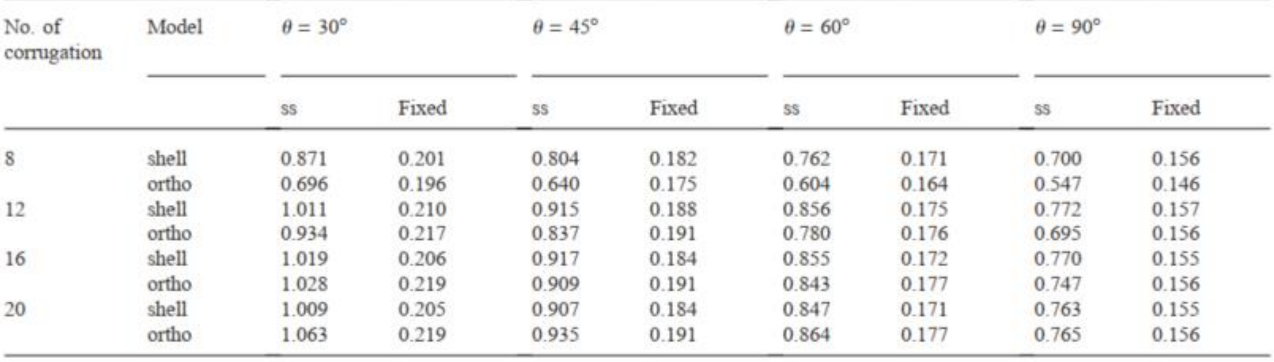

No. of corrugation	Model	$\theta = 30°$		$\theta = 45°$		$\theta = 60°$		$\theta = 90°$	
		ss	Fixed	ss	Fixed	ss	Fixed	ss	Fixed
8	shell	0.871	0.201	0.804	0.182	0.762	0.171	0.700	0.156
	ortho	0.696	0.196	0.640	0.175	0.604	0.164	0.547	0.146
12	shell	1.011	0.210	0.915	0.188	0.856	0.175	0.772	0.157
	ortho	0.934	0.217	0.837	0.191	0.780	0.176	0.695	0.156
16	shell	1.019	0.206	0.917	0.184	0.855	0.172	0.770	0.155
	ortho	1.028	0.219	0.909	0.191	0.843	0.177	0.747	0.156
20	shell	1.009	0.205	0.907	0.184	0.847	0.171	0.763	0.155
	ortho	1.063	0.219	0.935	0.191	0.864	0.177	0.765	0.156

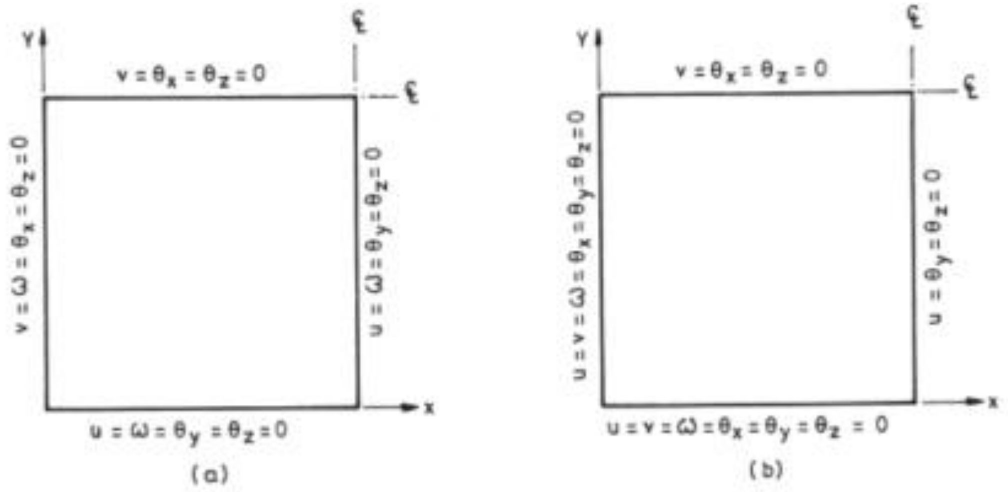

Figure 5 Definition of boundary conditions, simply supported (a) and clamped (b) (Samanta & Mukhopadhyay, 1997).

Figure 6 shows the central displacements obtained from both the linear and nonlinear numerical analyses of the two models. The results are presented for a sheet with 10 corrugations and a trough angle of 45 degrees. The applied boundary conditions are shown in Figure 5. Figures 7 and 8 present the displacement along the centreline in the x and y directions for both sets of boundary conditions. The number of corrugations in the sheet is set to 20 in both cases.

Overall, the results of the study demonstrate the validity and effectiveness of the proposed approach for the analysis of trapezoidal corrugated steel sheets. The inclusion of extensional and bending rigidities in the equivalent orthotropic plate model allows for more accurate nonlinear geometric analysis of folded plates. This approach can be useful in various engineering applications where corrugated sheets are used.

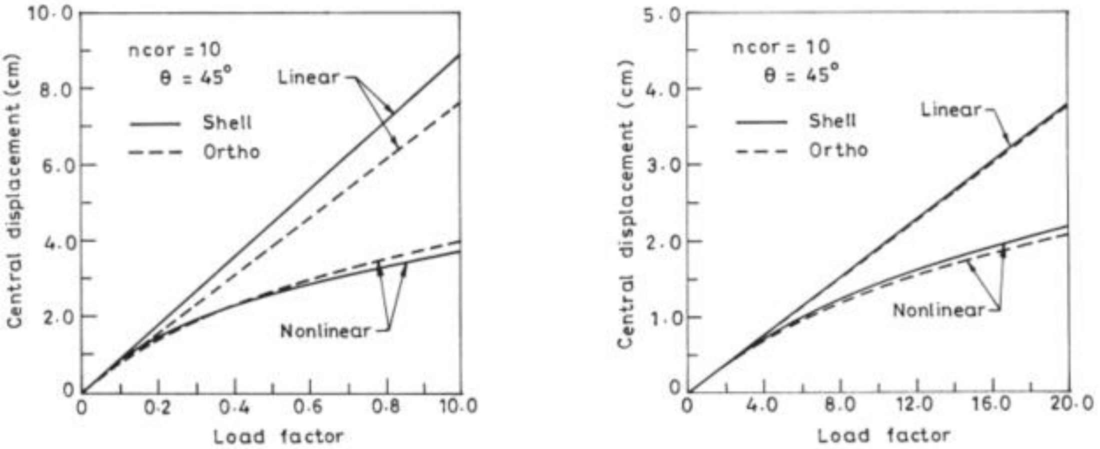

Figure 6 Comparison of nonlinear central displacement, simply supported (on the left) and clamped (on the right) (Samanta & Mukhopadhyay, 1997).

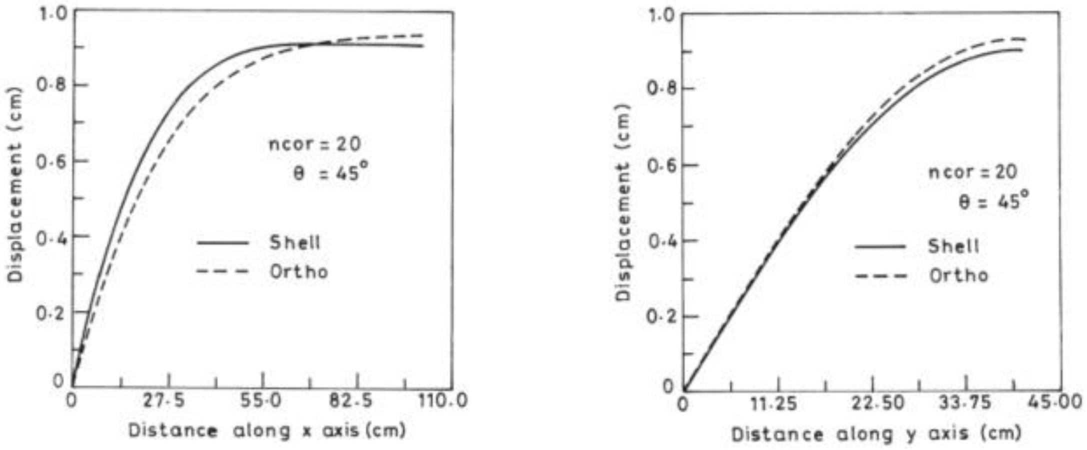

Figure 7 Simply supported: Displacement along the centre line, in X direction (left) and in the Y direction (right) (Samanta & Mukhopadhyay, 1997).

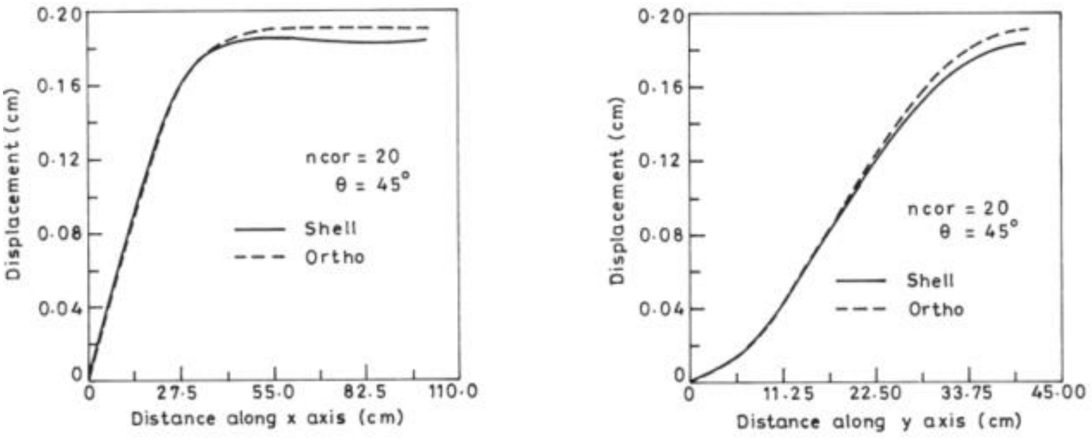

Figure 8 Clamped: Displacement along the centre line, in X direction (left) and in the Y direction (right) (Samanta & Mukhopadhyay, 1997).

2.2 Characterizing geometric imperfections and residual stresses

Thin-walled, cold-formed steel members such as corrugated sheets are widely used in construction due to their light weight, durability, and cost-effectiveness. However, their post-buckling behaviour can be difficult to predict due to the presence of imperfections, so making an accurate computational modelling is essential for effective design. One significant challenge in modelling these members is the characterization of geometric imperfections and residual stresses, which can have a significant impact on the behaviour of the structure.

To address this challenge, Lau (1988) has collected and analysed existing data and conducted experiments to develop simple rules of thumb and probabilistic concepts for modelling imperfections and residual stresses in cold-formed steel members (Lau, 1988). The two types of imperfections are shown in Figure 9. Type 1 rule of thumb is applied for width/thickness smaller than 200 and type 2 is for width/thickness ratio smaller than 100 (Schafer & Pekoz, 1998). The histograms of these imperfections are given in Figure 10.

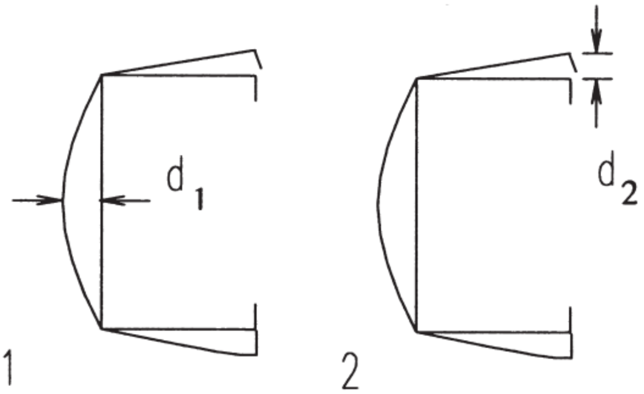

Figure 9 Definition of geometric imperfections (Schafer & Pekoz, 1998).

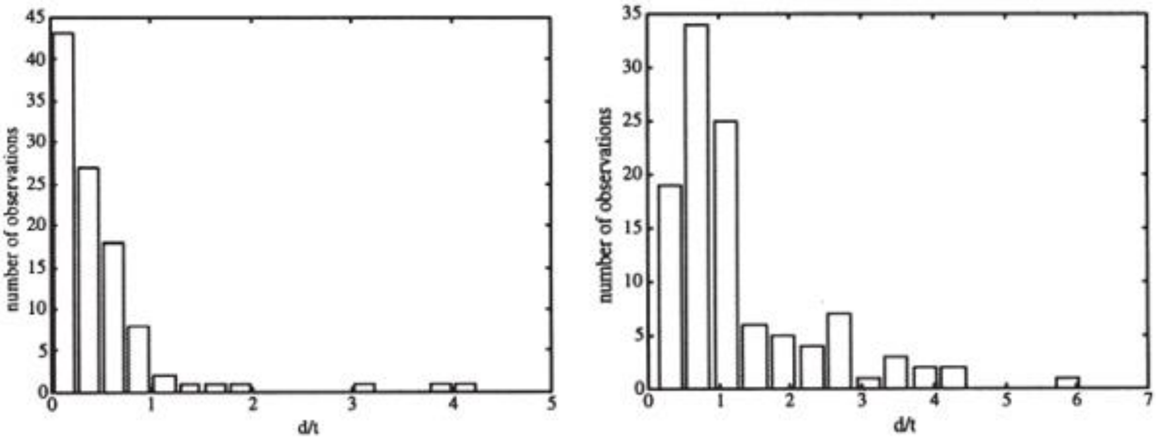

Figure 10 Histograms of type 1 imperfection (on the left) and type 2 imperfection (on the right) (Schafer & Pekoz, 1998).

One notable observation of this research is the absence of agreement regarding the appropriate distributions or magnitudes to utilize when modelling imperfections and residual stresses. However, the guidelines suggest that probabilistic distributions can be used to capture the variability of these factors, and that the magnitude of imperfections should be normalized to the member's cross-sectional dimensions (Schafer & Pekoz, 1998).

Residual stresses are stresses that remain in a material after it has been formed or welded and can affect the performance of the steel member under load. Computational modelling of residual stresses in cold-formed steel members is a challenge for analysts due to the lack of data and the complexity of the task. Residual stresses are often excluded from the analysis, or the stress-strain behaviour of the material is modified to approximate the effect of residual stresses. However, in cold-formed members, residual stresses are dominated by a through-thickness variation that leads to early yielding on the faces of cold-formed steel plates. This aspect of load-carrying behaviour is ignored unless residual stresses are explicitly considered in the analysis.

The study conducted by Schafer and Pekoz (1998) involved experimental investigations on residual stresses, using a total of 29 specimens, comprising 16 press-braked and 13 rolled samples. To simplify the analysis, residual stresses were categorized into two types: flexural and membrane stresses, because it is not realistic to measure through-thickness residual stress variations in thin plates experimentally (Key PW, 1993). Therefore, the available experimental measurements are limited to the surface faces of the plate (Schafer & Pekoz, 1998). The lack of data on residual stresses in cold-formed steel members has prompted the development of simple rules of thumb to estimate residual stresses.

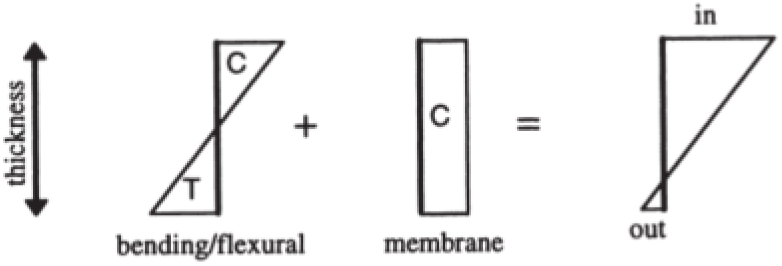

Figure 11 Flexural and membrane residual stresses (Schafer & Pekoz, 1998).

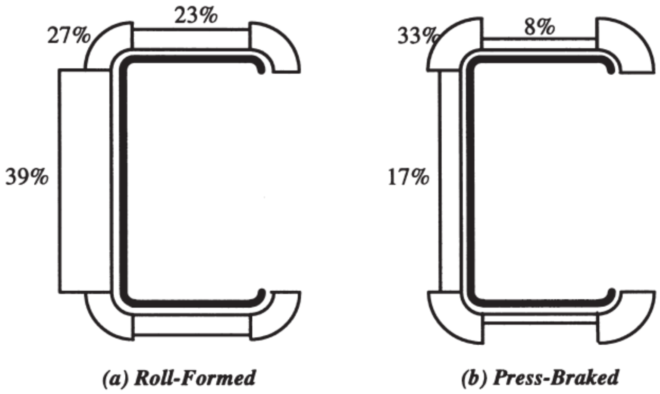

(a) Roll-Formed *(b) Press-Braked*

Figure 12 Average bending residual stresses as % of fy (Schafer & Pekoz, 1998).

In conclusion, understanding residual stresses and their effect on load-carrying behaviour is essential for accurate and reliable design of cold-formed steel members. Adequate computational modelling of residual stresses is challenging due to the lack of data and the complexity of inclusion. Simple rules of thumb may provide a useful estimation of residual stresses in the absence of experimental data.

2.3 Buckling analysis of corrugated sheets

To perform a buckling analysis, a specific section of the corrugated sheet was analysed by Wenberg & Stichel (2011) representing the area between two support beams. The dimensions of this section were 2271.5 mm (L_x) by 746.6 mm (L_y). Compression was applied in the corrugated direction (y-direction), with the long edges simply supported to simulate a continuous plate connected to the structural beams. The short edges were clamped. In Figure 13, the left-hand side illustrates the implementation of boundary conditions on the steel sheet, while the right-hand side demonstrates the span of the steel sheet, indicated as Ly, between two structural support beams.

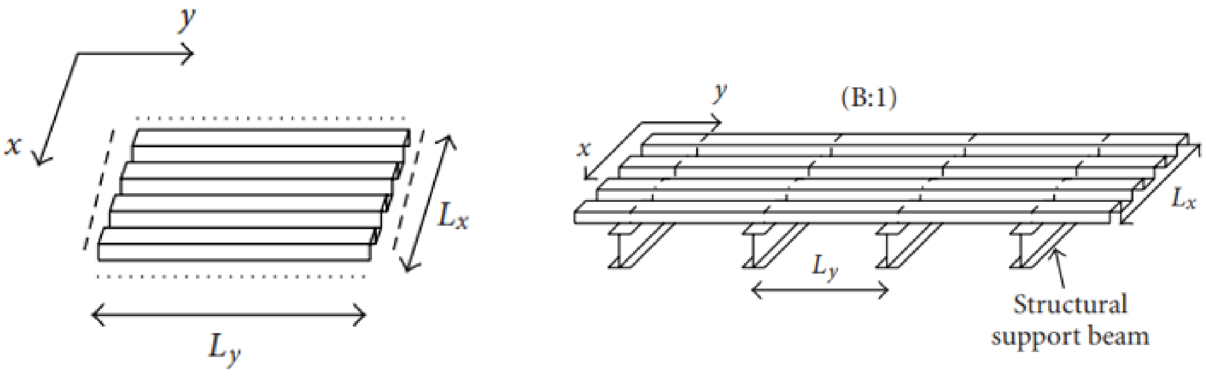

Figure 13 Application of boundary conditions to the steel sheet, clamped (dashed line) and simply supported (dotted line) (Wenberg & Stichel, 2011).

A half corrugation was analysed both analytically and using finite element (FE) analysis by Wenberg & Stichel (2011). A half corrugation with suitable boundary conditions buckles at a similar stress level to the entire sheet (Wenberg & Stichel, 2011). The geometry of the half corrugation beam is shown on the right-hand side of Figure 14, while the left-hand side of Figure 14 displays the full corrugation. The first buckling mode shapes of the half corrugation and the full sheet are presented in Figure 15.

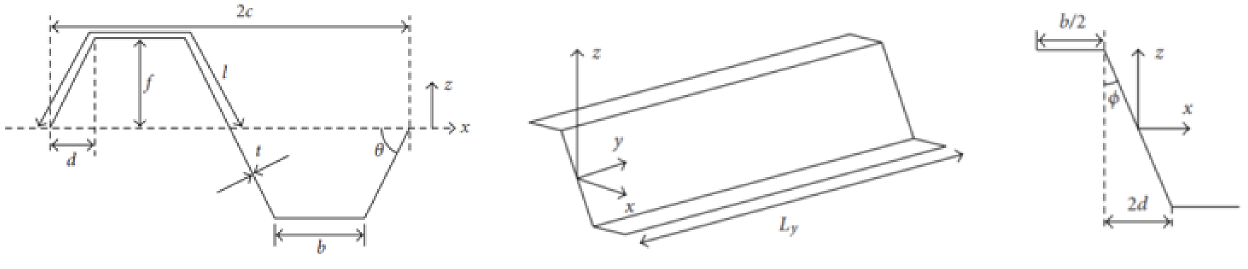

Figure 14 The geometry of full corrugation and half corrugation (Wenberg & Stichel, 2011).

The analytical buckling load for Euler buckling is determined using the equation provided below. In this equation, I_x represents the second moment of area of the cross-section, and l_e corresponds to the effective buckling length. When both edges are clamped, l_e is equivalent to half the length in the y-direction. To calculate the critical stress, the critical load is divided by the area over which the load is applied.

$$P = \frac{\pi^2 * EI}{l_e^2} \quad \& \quad \sigma = \frac{P}{A} \qquad (1)$$

The obtained critical stress is compared to the stress value from the finite element method. Also, an analytical local buckling stress is calculated with the following formula applying the same boundary conditions stated above (Wenberg & Stichel, 2011):

$$\sigma = \frac{(k * \pi^2 * E)}{(12 * (1 - \nu^2))} * \left(\frac{t}{l_b}\right)^2 = 3.6 * E * \left(\frac{t}{l_b}\right)^2 \qquad (2)$$

The study of Wenberg & Stichel concludes with Table 2 showing the critical stress from the different methods that are used.

Table 2 Comparison of the critical stress (Wenberg & Stichel, 2011).

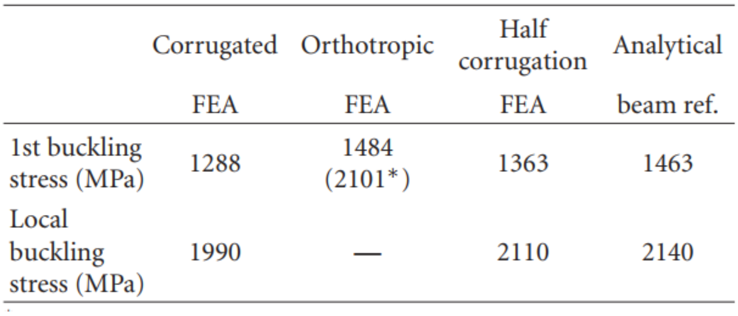

	Corrugated	Orthotropic	Half corrugation	Analytical
	FEA	FEA	FEA	beam ref.
1st buckling stress (MPa)	1288	1484 (2101*)	1363	1463
Local buckling stress (MPa)	1990	—	2110	2140

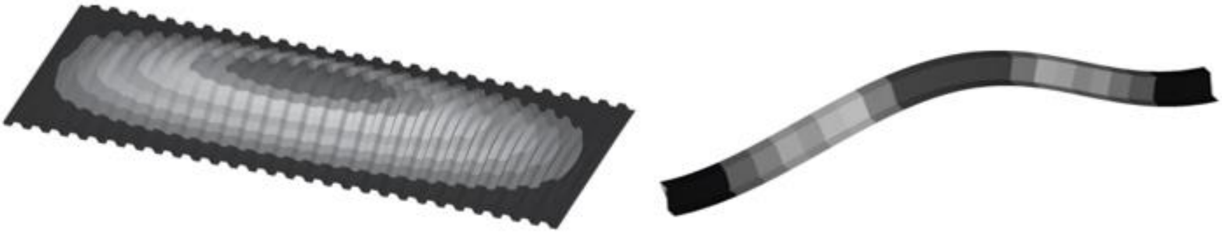

Figure 15 The 1st buckling mode shapes of the full sheet (left) & half corrugation (right) (Wenberg & Stichel, 2011).

The study concludes that the critical buckling stresses obtained from the half corrugation model and the analytical calculation have similar values, as shown in Table 2. The slight difference in the first critical buckling stress can be attributed to the inclination of the half corrugation's neutral axis to the xy-plane. However, the applied boundary conditions eliminate the effect of cross-section twisting.

2.4 PIR insulation material properties

PIR foams consist of a combination of polyurethane (PUR) and PIR groups. The urethanes are typically formed by combining polyfunctional isocyanates with molecules that have active hydrogen groups like multifunctional alcohols. The manufacturing process of Polyisocyanurate (PIR) foam polymer results in a stronger molecular structure when compared to traditional Polyurethane (PUR) foam. This is achieved by using highly cross-linked isocyanurate rings (Vitkauskiene, 2011). These improvements are reflected in the superior thermal stability, flame retardance, and mechanical behaviour of PIR (Czupryński, 2009). PIR is better suited than PUR for foam material applications that require these properties to be notable (Cabulis, 2014).

To characterize the PIR foam, compression and direct tensile tests were conducted in accordance with applicable normative rules. For the compression tests, ASTM C365 specifications were adopted, and 5 specimens were tested, resulting in an average compressive strength of 0.22 MPa (CoV = 10.67%) and elastic modulus of 5.81 MPa (CoV = 11.53%), as shown in Figure 16. The direct tensile tests followed the ASTM C297 guidelines, and 5 specimens were tested, resulting in an average direct tensile strength of 0.22 MPa (CoV = 15.52%) and elastic modulus of 4.79 MPa (CoV = 10.03%), as depicted in Fig. 1(b). The uniaxial compression and tensile tests were conducted in the direction parallel to the foam rise (Figueira, 2019).

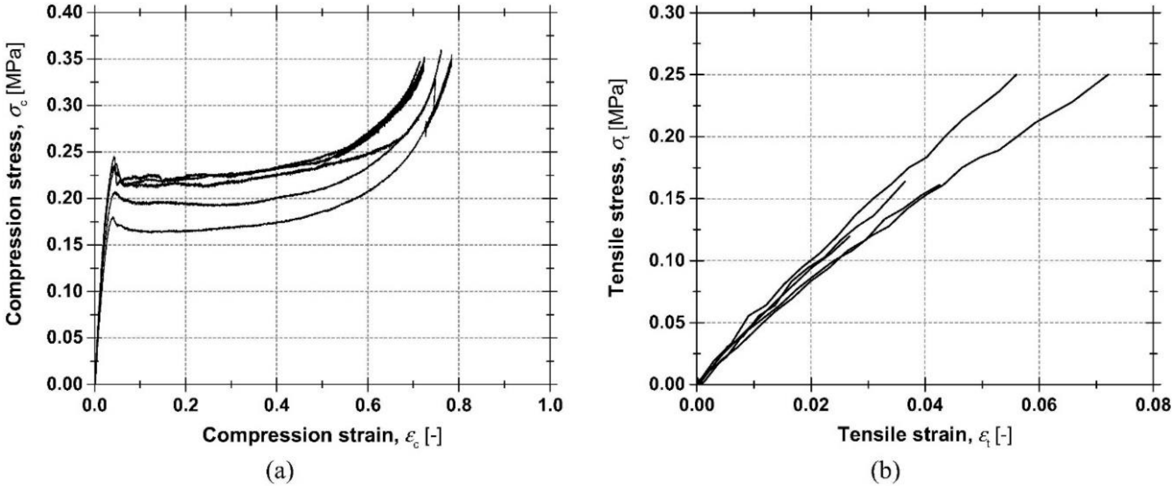

Figure 16 Stress-strain curves: (a) compression; (b) tensile (Figueira, 2019)

3 Experimental research

3.1 Methodology

To address the research questions, two separate experiments were conducted on specimens measuring 1.86 x 2.2 m², each under different load conditions. The main goal of the experiments is to see how the load is distributed among the steel ribs of the steel sheet due to the presence of the PIR insulation layer. The two load conditions are illustrated in Figure 17, where the applied surface has a rectangular shape with the dimensions of 250 mm by 70 mm and it is applied at the midspan of the specimen. These are two loading conditions which are representative on real-structures roofs. Load case A consists of two small surface loads that are applied above each rib. For load case B, there is one rectangular surface load of the same area as Load case A. However, the rectangular surface load is rotated by 90 degrees for load case B. In this chapter, the testing of both load cases and the results of the experiments are discussed.

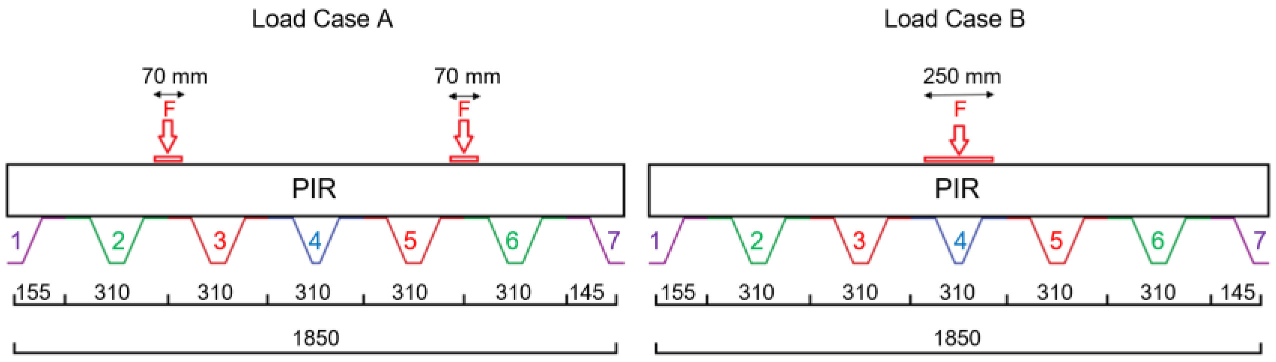

Figure 17 Load case A (on the left) and Load case B (on the right).

3.2 Specimens

The specimen consists of two connected corrugated steel sheets that are connected by bolts. Each sheet consists of 3 ribs which gives a total of 6 ribs for the total steel sheet. PIR insulation is placed on top of the steel sheet and the strips are connected to the steel sheets from below. The specimen details are explained further in detail in this chapter. Figure 18 shows the specimen where it is turned upside down, as the PIR is shown at the bottom of the specimen and the steel sheet being on top of it with the two strips connected to the steel sheet. PIR insulation is placed on top of the steel sheet as shown in Figure 17.

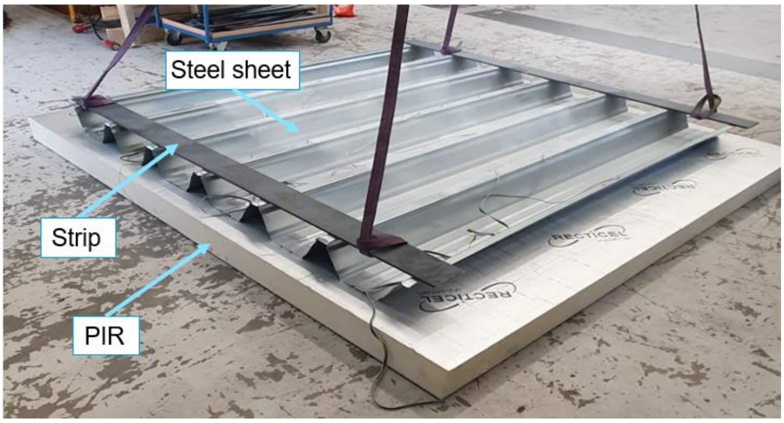

Figure 18 Lifting of the specimen (turned upside down).

3.2.1 Corrugated steel sheet

Two SAB135R/930 steel sheets are used in the experiments with thickness equal to 0.88 mm. The geometry of one steel sheet is shown in Figure 19, where it is shown that the steel sheet consists of 3 ribs. Two steel sheets of width equal to 930 mm are connected to each other resulting in a sheet of a total of 6 ribs as shown in Figure 20. The connection of the steel sheets is done by using self-tapping screws Hilti S-MS 01(S)S 4.8x20 with centre-to-centre distance of 300 mm. Also, the connection between the steel sheet and the strip is done by screws as well. The type of screws used for this connection is Hilti-X-ENP nails. The details of the connections are shown in Figure 20, where a zoomed in picture is shown for the connection.

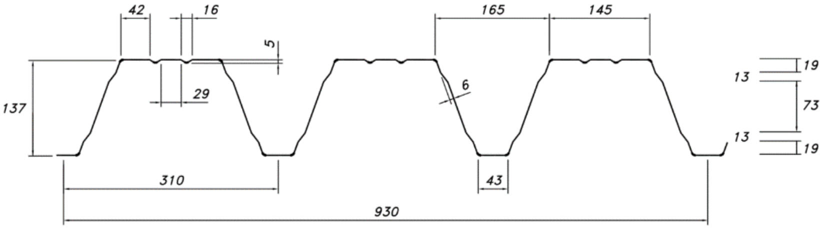

Figure 19 Geometry of the steel sheet - SAB135R/930.

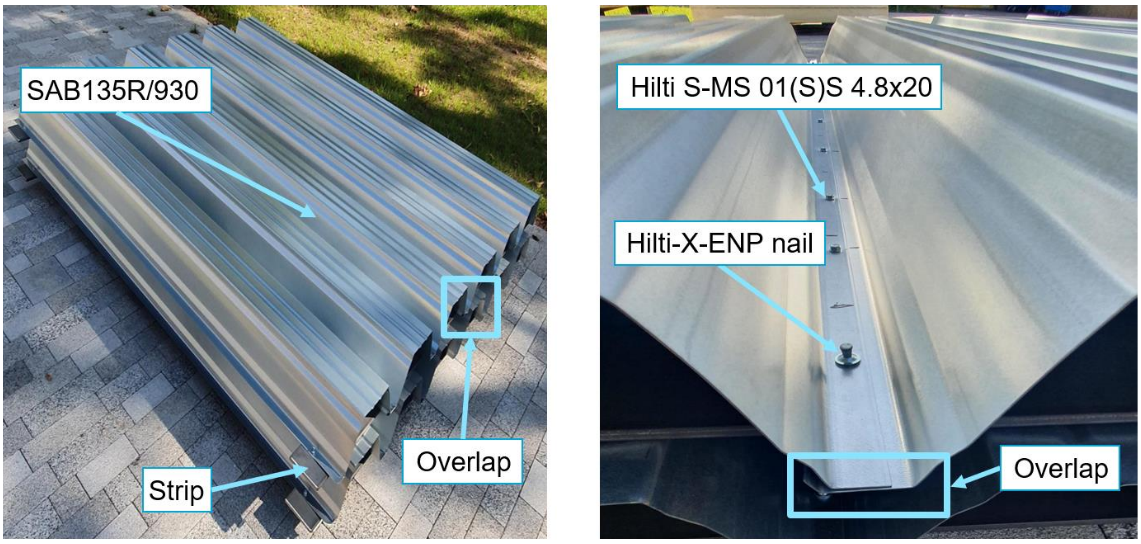

Figure 20 The connection between two steel sheets of type SAB135R/930.

3.2.2 PIR insulation

The dimensions of the available PIR insulations layers are 2400 mm by 1200 mm with a thickness of 140 mm. Since the span of the small-scale experiment is equal to 2 meters and the dimensions of the steel sheet being 2 multiplied by 930 mm which gives 1860 mm, multiple PIR insulation layers are placed next to each other and are connected to the steel sheet by EJOT J27-6.3x165-E16 bolts. The connection between the PIR insulation and the steel sheet is shown in Figure 21.

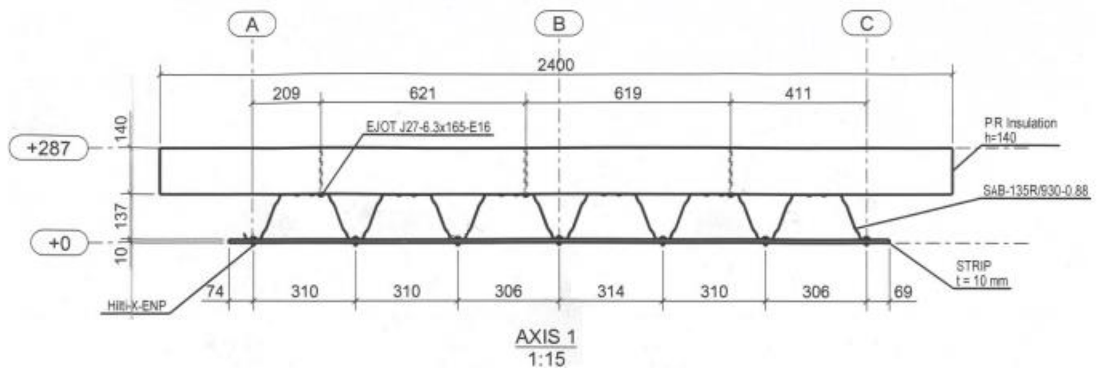

Figure 21 Connections in the specimen.

3.3 Loading configurations

For load case A, two load cells are used which are positioned at mid span. The available dimensions of the PIR layer are 2400 mm by 1200 mm, meaning that two PIR layers with these dimensions are used and placed next to each other. For load case B, one load cell is used, and it is applied at the middle of the PIR layer. Two PIR layers with these dimensions are used for this case as well. However, one layer is cut in half to make two 2400 mm by 600 mm layers. This is done to prevent the situation where the split between the PIR layers coincides with the load application location. The PIR layers are placed next to each other and are rotated. The configuration of the PIR layers for both load case A & B is shown in Figure 22. The blue rectangles represent the strips where the supports are applied. The span, which is the distance between the two strips, is equal to 2000 mm as shown in Figure 22.

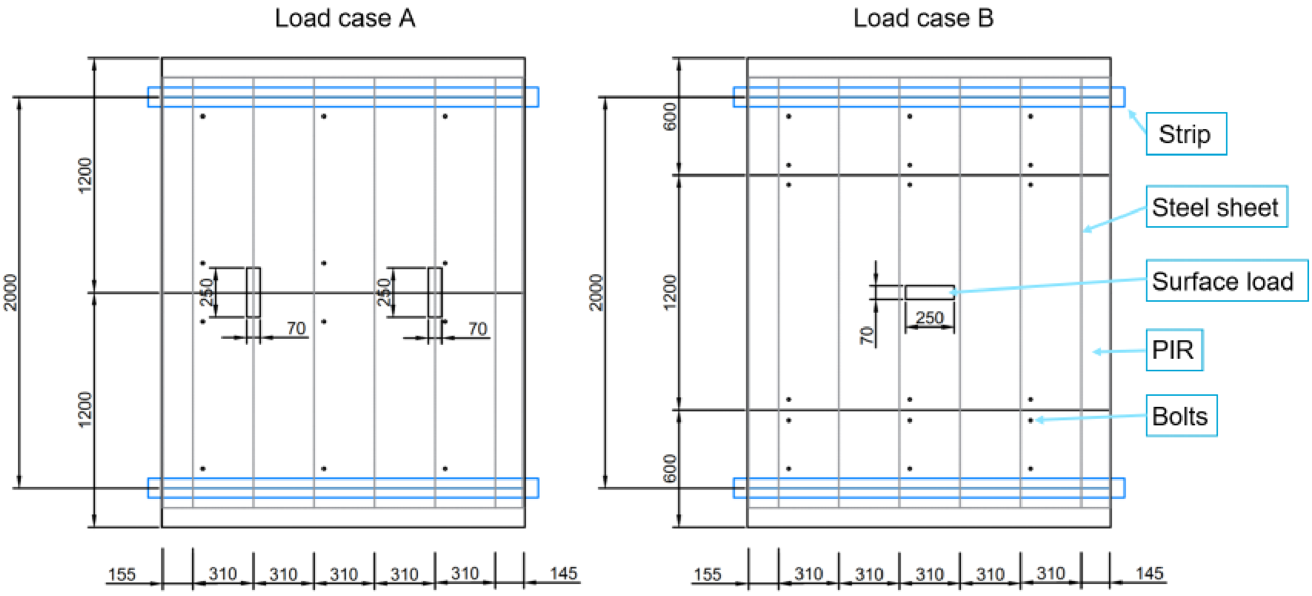

Figure 22 Top view of PIR for both load cases with the steel underneath highlighted.

3.4 Instrumentation

Figure 23 shows the instrumentation that is used for the testing of both experiments (2 load cases). The description of the instrumentation is stated below.

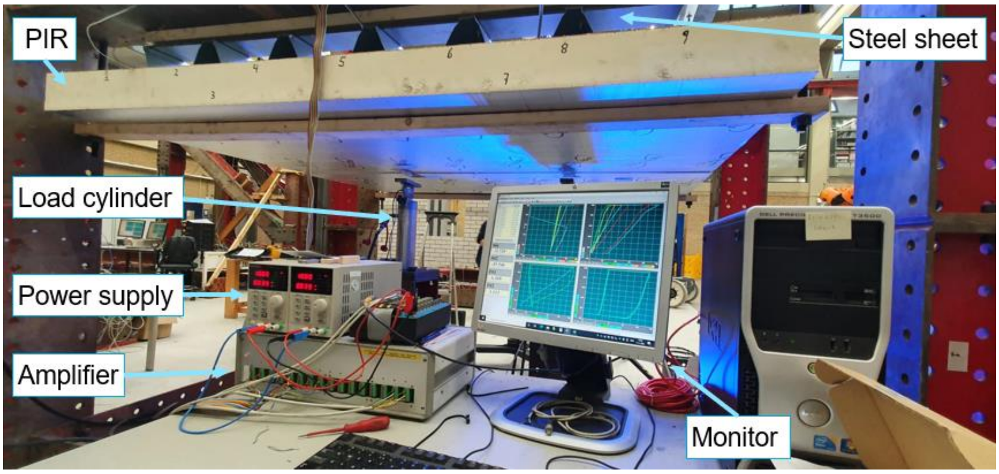

Figure 23 The specimen and the instrumentation used for testing.

Load cylinder
The hydraulic load cylinder provides the possibility of generating a force from a pressurized fluid that will lead to controlled loading situation on the specimen. The pressure is applied manually, Figures 23 and 24 show the load cylinders.

String potentiometers
A string potentiometer is a device that measures the position of a string by converting its linear motion into an electrical signal. It has a wire sliding part that moves along a resistive. The change in resistance between the sliding part and the resistive element generates an electrical signal that shows the position of the string. The string potentiometer is placed on the loading jack to measure the vertical displacement at load location. The applied string potentiometer on the load cell is shown in Figure 24.

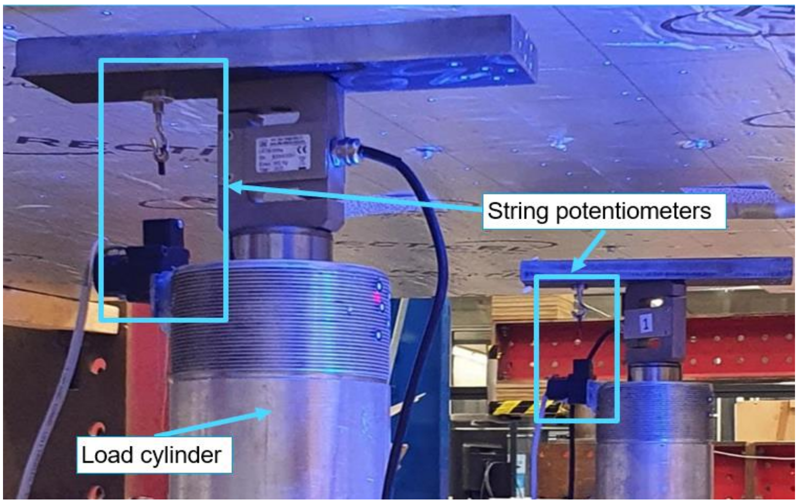

Figure 24 Load cylinders and string potentiometers.

Amplifier

A strain gauge amplifier is a device that is used to amplify the small electrical signals generated by a strain gauge. Due to this, the small electrical amplitudes are amplified which makes it possible to measure the strain gauges and to analyse the data. The amplifier is shown in Figure 23.

DIC System

On top of the conventional instrumentation (strain gauges and string potentiometers) for measuring the deflections on the specimens, a DIC system is used. DIC stands for "Digital Image Correlation" which is a system that uses cameras and computers to measure deformations, strains, and displacements. The cameras take multiple pictures when the object is being loaded. The data of the taken pictures are then imported into a computer software to get the analysis process starting. There are two cameras, shown in Figure 25 that take pictures of the specimen while being tested, one camera takes pictures of the top view (steel sheet) and the other one takes pictures of the bottom view (PIR insulation) simultaneously. The analysis is done by using the software GOM Correlate. GOM Correlate is a DIC software created by GOM (Gom, 2022), a company that specializes in technology for 3D metrology and testing. It allows the measurement of deformation and displacement in objects by using digital images as inputs.

Computer & Monitor

The applied load is shown on the computer while the specimen is being tested. The increase of the load and the full data of strain gauges, string potentiometer & DIC system are stored.

Support reaction cylinder (roller) with wood base

A cylinder of length equal to the length of the steel strip is placed above the strip. A wooden base is placed below the cylinder to implement the simply support characteristics. Two cylinders are used for the support reactions for the specimen. The support roller is shown in Figure 25.

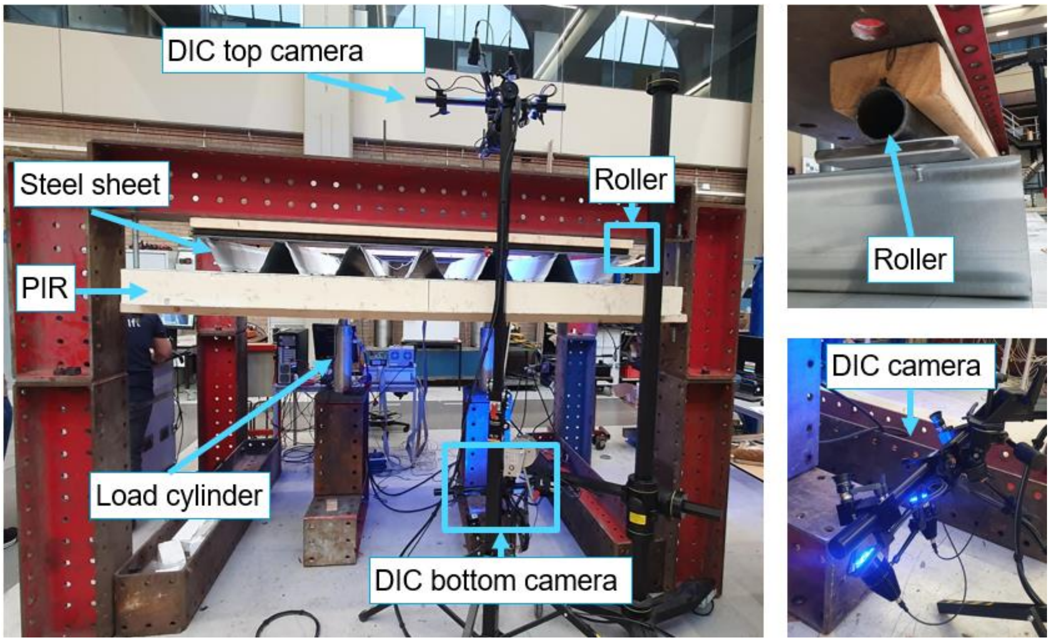

Figure 25 DIC cameras (measuring position 1) and support roller.

Strain gauges

Strain gauges are used to measure the strains of the steel in the longitudinal direction between the two supports. Strain gauges consist of thin foil pattern of conductive material that is attached to the clean steel surface. The strain gauge converts compression and tension forces into electrical resistance. The strain gauge resistance increases whenever a tensile strain is applied and decreases whenever compressive strain is applied. The strain gauge that is used in the experiments is of type FLAB-6-11. The gauge length is equal to 6 mm & the strain limit is 3%. The strain gauges use copper-nickel alloy in the grid and epoxy resin in the backing. The epoxy backing offers good insulation and is color-coded to match the material being tested for temperature compensation. The resistance of the strain gauge changes with the amount of strain on the object, usually a small change in the range of few parts per million to a few percent. To measure the strain accurately, the resistance change is compared to a reference resistor in a bridge circuit and amplified for accurate reading proportional to the strain on the object.

Figure 26 shows the application of a strain gauge on the steel sheet. As stated before, the strain gauges measure the longitudinal strains at the locations shown in Figures 27 and 28. FLAB-6-11 strain gauges give accurate results with an accuracy of 1%.

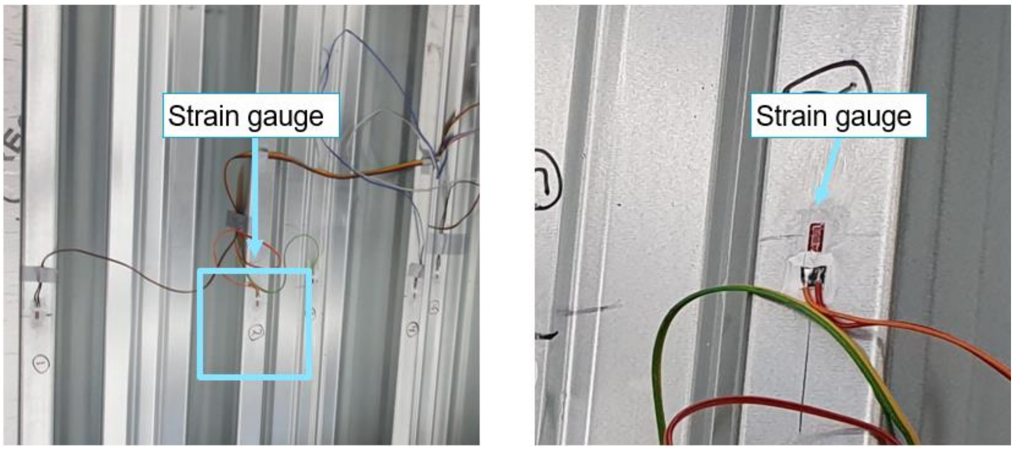

Figure 26 Strain gauge on the steel sheet.

The locations of the strain gauges are shown in Figure 27 for the first experiment (load case A) and in Figure 28 for the second experiment (load case B). The strain gauges are highlighted with red, orange, and blue squares with a specified number for each gauge. The red squared are for the gauges at mid span, the orange squares are used to indicate the gauges that are placed near the supports and the blue squared are used for the gauges of the webs. The black rectangles represent the projection of the load that is applied on the PIR layer.

A total of 9 strain gauges is used for the first experiment and 19 for the second experiment. The reason for the increased number of strain gauges for the second experiment is because of the changed loading condition as there are two additional strain gauges added near the load, these strain gauges are 16 and 17 at midspan. The addition of strain gauges 10-15 is done to investigate the strains near the supports and strain gauges 18 and 19 are added to investigate the strains at the webs at the location of loading.

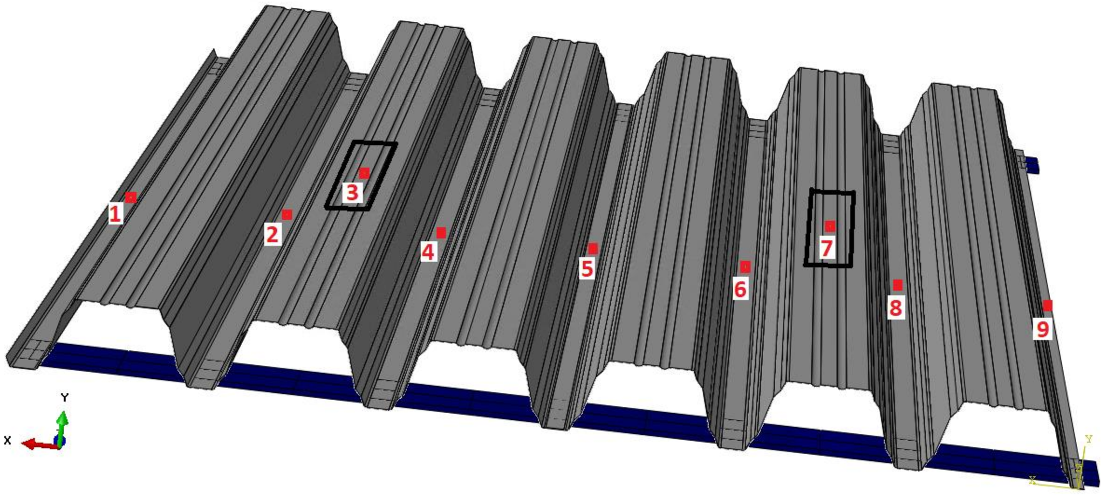

Figure 27 Locations of strain gauges for the first experiment (Load case A).

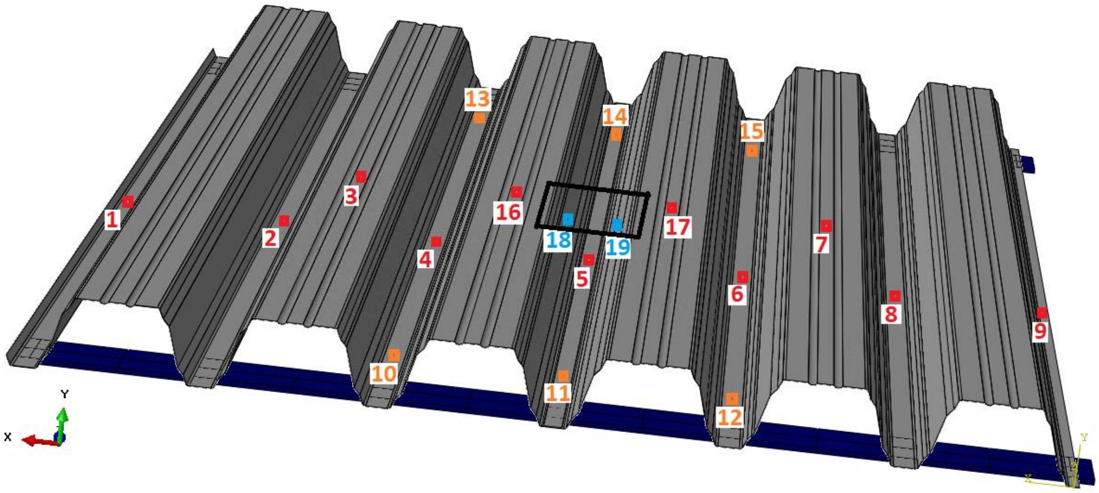

Figure 28 Locations of strain gauges for the second experiment (Load case B).

3.5 Experiment 1: Load case A

As explained above, the setup for the experiment is shown in Figure 25. The specimen was tested for the first experiment which was loaded with two surface loads resembling load case A (see Figure 18). The application of the loads is shown in Figure 24, the two load cells are shown where the applied hydraulic load is simultaneously done with equal force values at each location.

Figure 29 Application of two surface loads on 2 positions.

String potentiometers are placed at each load cell and the DIC cameras make pictures from top and bottom of the specimen. The DIC measures the vertical displacement of (glued) targets that are placed on the PIR insulation. On the other hand, on the steel sheet the specimen was painted white with a black sparkle pattern applied on top of the white paint so that the DIC camera can track the vertical displacement of these black points. Figure 30 shows the top and bottom view of the specimen where the (glued) targets at the bottom and contour at the top are applied. Also, on the top of the loading cylinder where the loading is applied, rubber feet were placed. The rubber is shown in Figure 31.

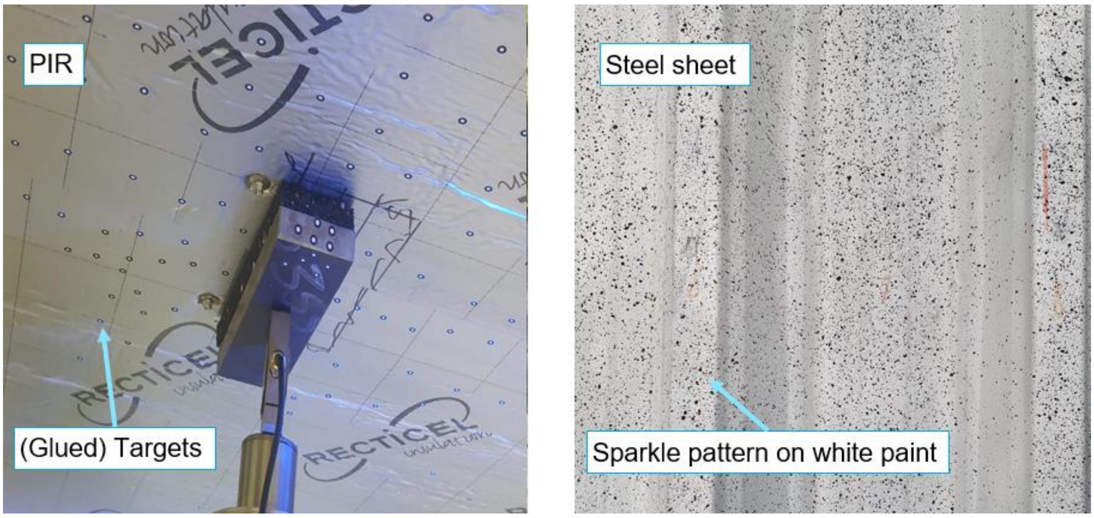

Figure 30 DIC (glued) targets on PIR (on the left) & DIC Contour on the steel (on the right).

The DIC cameras can only give accurate measurements for a certain size of measuring field with that being equal to 1.2 m by 0.9. To solve this, the DIC cameras are placed on different positions for different tests, because the two loads cannot be measured at once from the DIC. The specimen is tested four times, with the adjustment of the maximum applied load and the DIC camera location. The testing sequence was the following:

- Test01 (up to 1500 N): The DIC cameras are placed on position 1.
- Test02 (up to 1500 N): The DIC cameras are placed on position 2.
- Test03 (up to 3000 N): The DIC cameras are placed on position 2.
- Test04 (up to failure): The DIC cameras are placed on position 2.

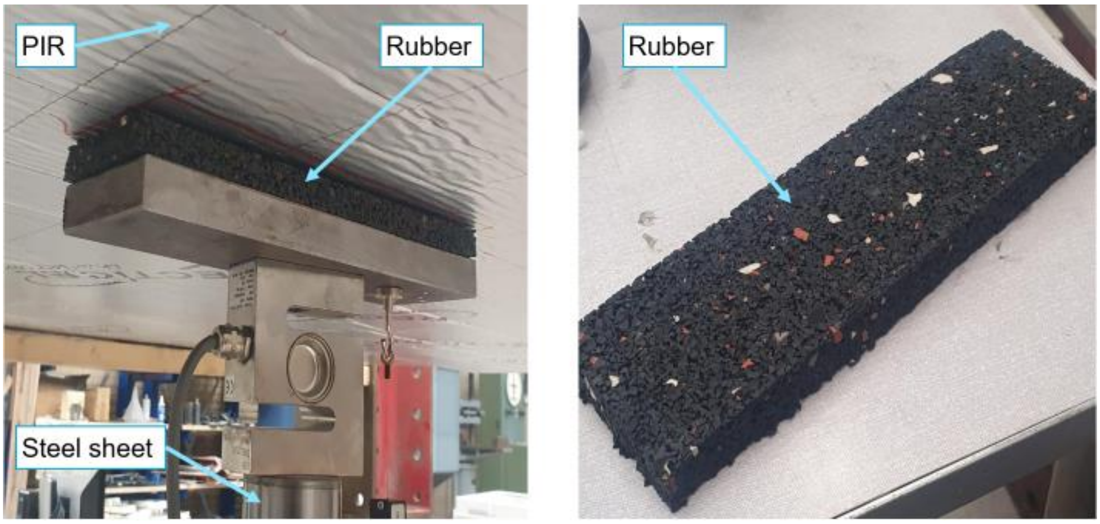

Figure 31 Application of rubber at load positions.

3.6 Results of experiment 1: Load case A

3.6.1 Force vs displacement diagrams at the two loading positions

Figure 32 shows the force vs displacement graph of the two load cells that are measured by the string potentiometers. The shown curves are obtained from the 4th test where the specimen was loaded until failure, which is equal to 4000 N. When looking at the graph, there is more displacement at the beginning at position 1 than position 2. However, both curves have a parallel relation for the displacement from a certain applied force which is equal to nearly 500 N. The two curves have therefore parallel linear relationship between 500 N up to the failure load of 4000 N.

The nonlinear development of both curves up to 500 N is caused by the behaviour of the rubber that is placed on the load cell as shown in Figure 32. The rubber is compressed and gives resistance to the compression but after a certain load the effect of the resistance is eliminated.

However, there is still difference between the two curves even between 500 N and 4000 N. This difference is constant meaning that it is caused by an initial displacement that is caused by a gap between the PIR and the steel. The difference is equal to 2 mm, meaning that at location 2 there is an initial gap difference between the PIR and the steel that is equal to 2 mm.

Figure 32 shows the results of all the tests in a combined graph, it is noticeable to see that the same development of force vs displacement curves happens. For all tests, position 1 have bigger displacement values than position 2 for the same force.

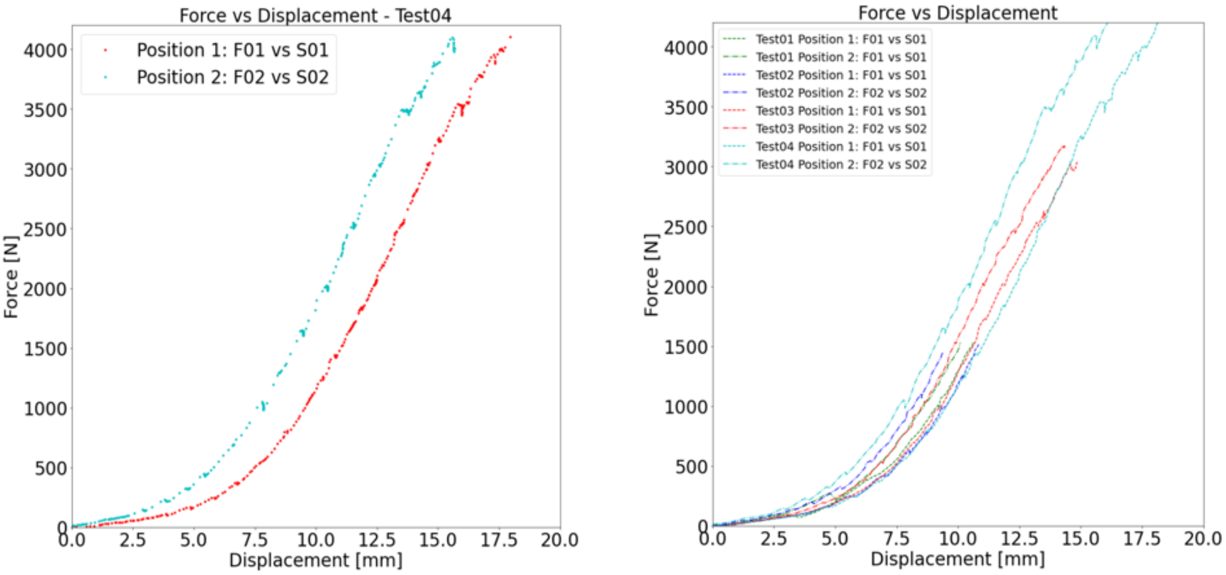

Figure 32 Force vs displacement at load positions measured by the string potentiometer.

Tables 3-5 show the difference of displacements between the two loading positions is for all tests and at loads of 1500 N, 3000 N and 4000 N

Table 3 Difference in displacement between the two loading positions at 1500 N.

Load	F = 1500 N		
Test	Position 1	Position 2	Difference
1	10	10.5	0.5 mm
2	9.5	10.5	1 mm
3	9.75	10.25	0.5 mm
4	10.9	9.85	1.05 mm

Table 4 Difference in displacement between the two loading positions at 3000 N.

Load	F = 3000 N		
Test	Position 1	Position 2	Difference
3	14.7	13.75	0.95
4	14	12.5	1.5

Table 5 Difference in displacement between the two loading positions at 4000 N.

Load	F = 4000 N		
Test	Position 1	Position 2	Difference
4	17.4	15.25	2.15 mm

3.6.2 Results of strain gauges

Nine strain gauges were used for the first experiment, the locations of the strain gauges are shown in Figure 33. The result of the strains for every location is determined for the load of 4000 N. Similar distribution is observed for loads equal to 3000 N and 1500 N, this is included in Appendix A. Also, the results for the strain development for different loads at the 7 bottom flange locations in the steel is shown in Appendix A.

Figure 33 shows the values of the strain gauges that are placed in the bottom flange, meaning the strain gauges that are subjected to tension. These locations are 1 to 9, except location 3 and 7 which were placed in the top flange of the sheet and subjected to compression.

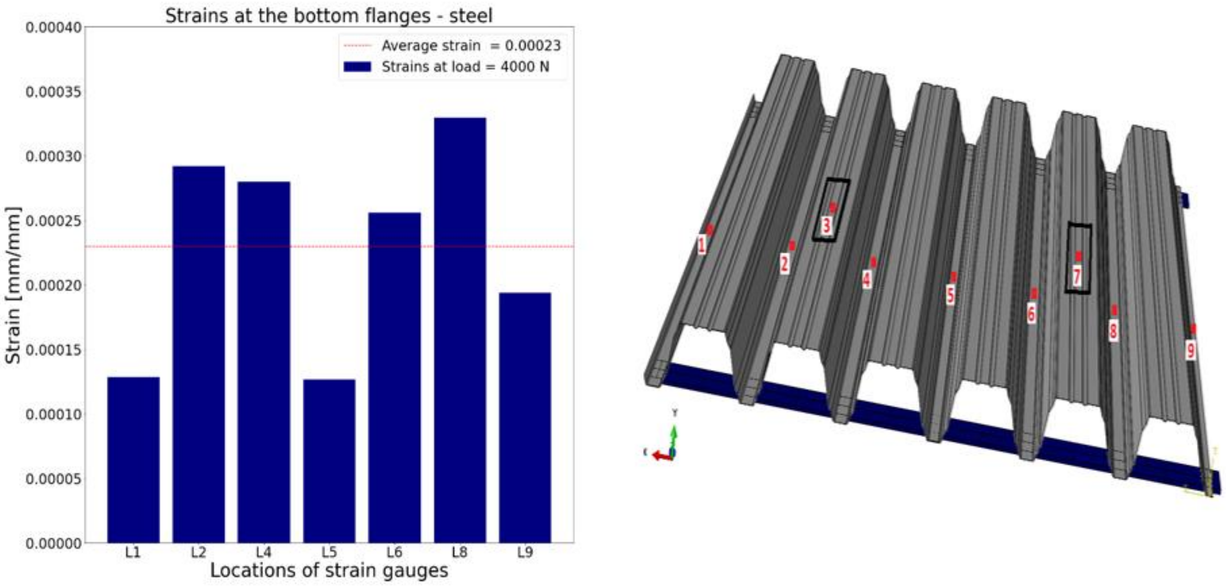

Figure 33 Strains of gauges on the bottom flange of the steel sheet for the load of 4000 N.

The distribution of strains is given in Table 6, with the values of strains at these locations and how much percent each location has when it is normalized to the maximum strain.

Table 6 Percentage of each strain value for a location normalized to the maximum value.

Experiment raw: Load case A, Span = 2 m							
Load = 2*4000 N (at midspan)							
Locations	L1	L2	L4	L5	L6	**L8**	L9
Ribs	1	2	3	4	5	**6**	7
Strains [$*10^{-6}$] [mm/mm]	128.4	291.9	280	126.4	255.8	**329.7**	193.7
Percentage [%]	**38.9**	**88.5**	**84.9**	**38.3**	**77.6**	**100**	**58.8**

It is noticeable in the results that location 2 & 4 and 6 & 8 have higher values that the average line. This is expected because the load occurs at location 3 which is between location 2 & 4. The same goes for locations 6 & 8, as the second load is applied at location 7 which is between 6 & 8. However, the distribution of the strain is not symmetrical as it is seen that location 8 has higher values than location 2 for all three load cases. Also, the strain values in location 4 are higher than location 6 for all three load cases. The same applies for location 1 & 9 with location 9 having a higher value since the two locations are not symmetrical because of the geometry of the steel sheet as shown in Figure 19. The results demonstrate that the strain gauges positioned in the troughs near the applied loads show higher values (maximum), whereas the troughs situated farther away from the load application showcase relatively lower values, as anticipated.

3.6.3 Failure mode

The Failure load was equal to 4070 N as rupture in the PIR occurred. The displacement that was reached for 4070 N in the PIR was equal to approximately 17 mm for position 1 and 15 mm for position 2, meaning that the rupture happens when the deformation of the PIR exceeds 10% of the thickness which is 14 mm of 140 mm thick PIR insulation layer. Figure 34 shows the failure of the PIR insulation which occurs first before the buckling and yielding of the steel. The steel sheet did not show any signs of failure before the PIR rupture load of 4070 N was reached. Figure 35 shows the steel sheet after the rupture of the PIR.

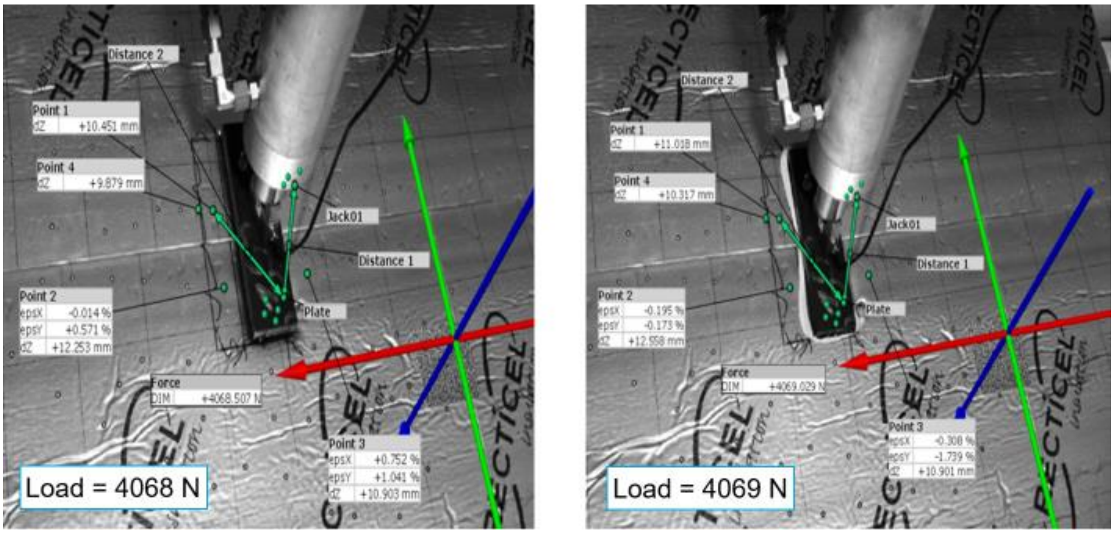

Figure 34 Rupture of PIR insulation when the load equals to 4070 N.

Figure 35 Failure of the PIR after testing (on the left) and the steel sheet after testing (on the right).

3.6.4 Failure modes

The specimen was dismantled after testing it up to failure. There was no deformation observed in the bolts connecting the PIR insulation to the steel. Figure 36 shows the steel sheet after dismantling where local buckling in the flanges and webs at load location were observed. Figure 37 shows the development of the crack in the PIR insulation with a trapezoidal shape being formed along the thickness of the PIR. This was observed after the split of the two PIR layers in the middle of the applied surface load. The trapezoidal shape started at 70 mm width at the loading surface and continued to grow until the width reaches 300 mm. The angle of failure in the PIR was equal to 39°.

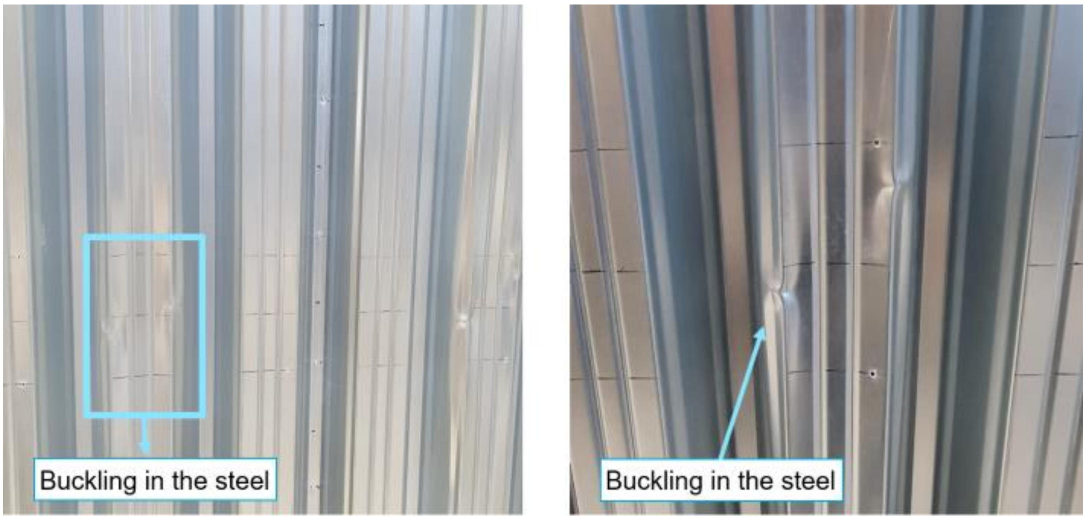

Figure 36 Buckling in the steel sheet after testing at load locations.

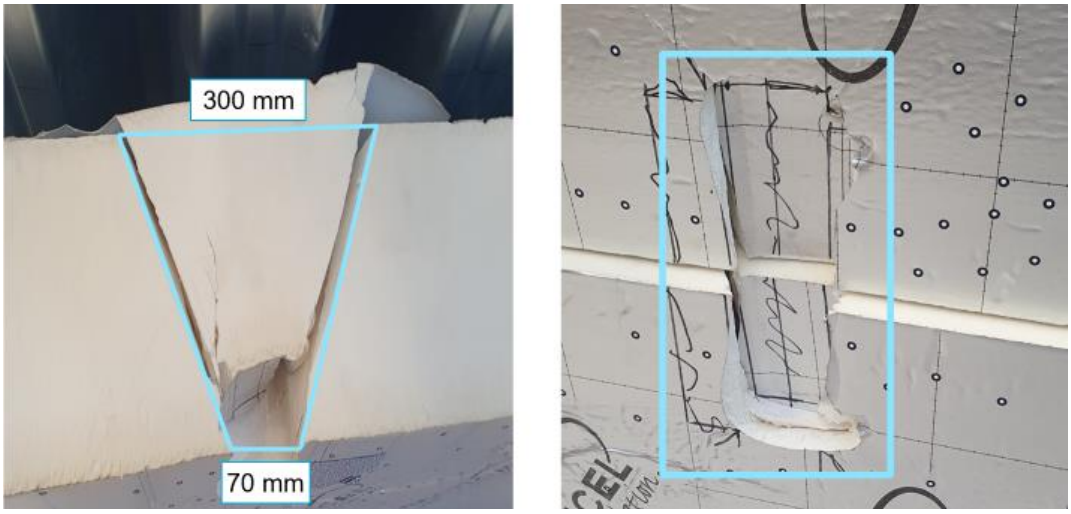

Figure 37 Failure in the PIR.

3.7 Experiment 2: Load case B

The second experiment was conducted with one load cell which applied the load at the middle of the PIR layer, and resemble load case B. The application of the load is shown in Figure 38. A string potentiometer and DIC were used for contacting measurements as described in the first experiment. Rubber was also placed on the top of the load cell, as shown in Figure 31. Multiple tests were conducted, consisting of two tests with loads up to 1500 N, two tests with loads up to 3000 N, two tests with loads up to 4500 N, and one final test carried out until failure occurred. Since there is only one load position, there is only one position for the placing of the DIC cameras that measure the top and bottom vertical displacement of the specimen at load location. As discussed, earlier glued targets were placed on the PIR insulation for the DIC camera to track the vertical displacement of these (glued) targets. The DIC did not give accurate results for the strains, because the DIC does not give accurate results for the horizontal deformation. It was chosen to apply (glued) targets on the steel sheet as well to measure only the vertical displacement, as these were accurately measured by the DIC. The (glued) targets on the PIR and the steel are shown in Figure 39.

There were 7 tests performed on the same specimen and the difference between each test was the applied maximum load. For the first two tests the specimen was subjected to 1500 N, after un-loading the specimen was subjected to a maximum of 3000 N for the third and fourth test. The fourth and fifth tests reached a maximum applied of 4500 N and for the final test the load was applied until the specimen failed.

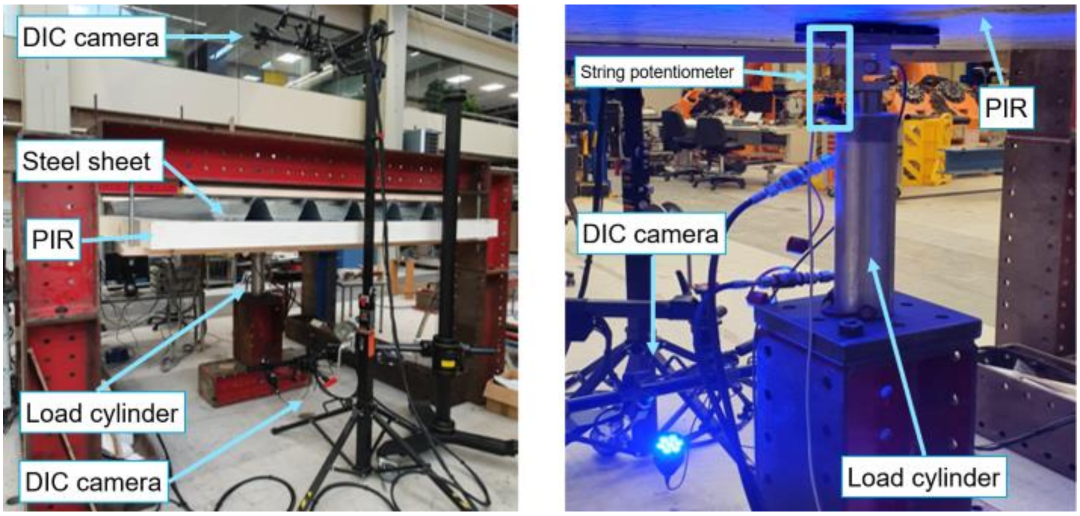

Figure 38 Application of the surface load.

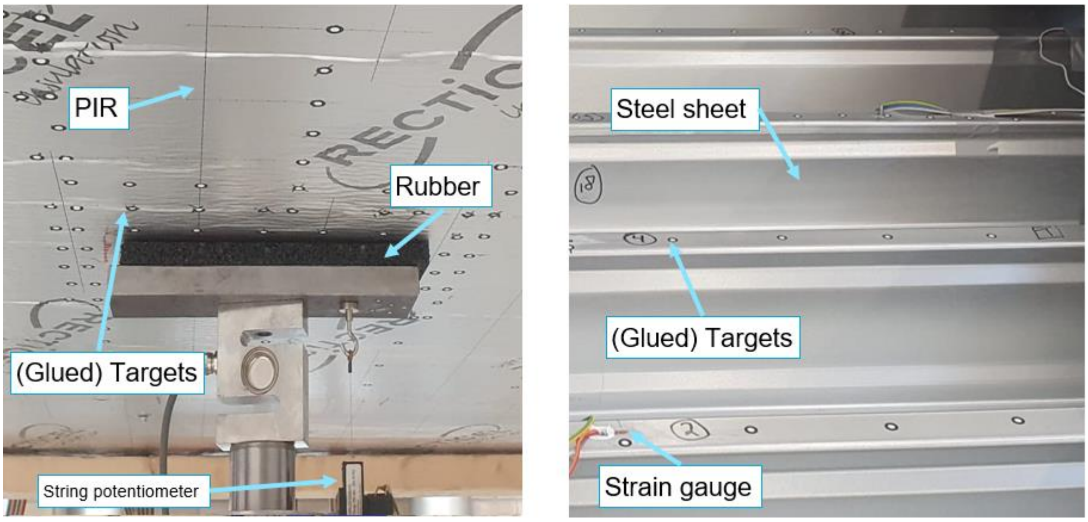

Figure 39 DIC (glued) targets on the PIR (on the left) and on the steel (on the right).

3.8 Results of experiment 2: Load case B

3.8.1 Force vs displacements at load location

In this experimental study, the potentiometer, and Digital Image Correlation (DIC) techniques were applied to analyse the force-displacement behaviour of a steel roofing sheet with PIR insulation. The potentiometer was positioned at the load location on the jack, enabling the measurement of force against displacements at that specific location. The results obtained from the second experiment are presented in Figure 40.

Upon analysing Figure 40, a change in the force vs. displacement curve was evident at a load of 5000 N. This load marked the failure of the PIR insulation, with the PIR layer experiencing a displacement of 15 mm that exceeded 10% of its deformation capacity. Also, cracks started to develop at corners of the rectangular surface load when the load was equal to 5000 N. The development of these cracks is visually presented in Figure 43. The graphs of the potentiometers for all different tests show comparable results with the rupture happening when the load is equal to 8000 N with a displacement of 30 mm. The descending branch is also shown where the loading jack pushes through the PIR insulation after rupturing it to cause buckling and yielding in the steel sheet. The deformation of the PIR insulation is also measured with the DIC cameras which give matching results to the deformations measured by the string potentiometer. On the other side, the deformation of the of the steel is measured by the top DIC camera, the results are also shown in figure 40.

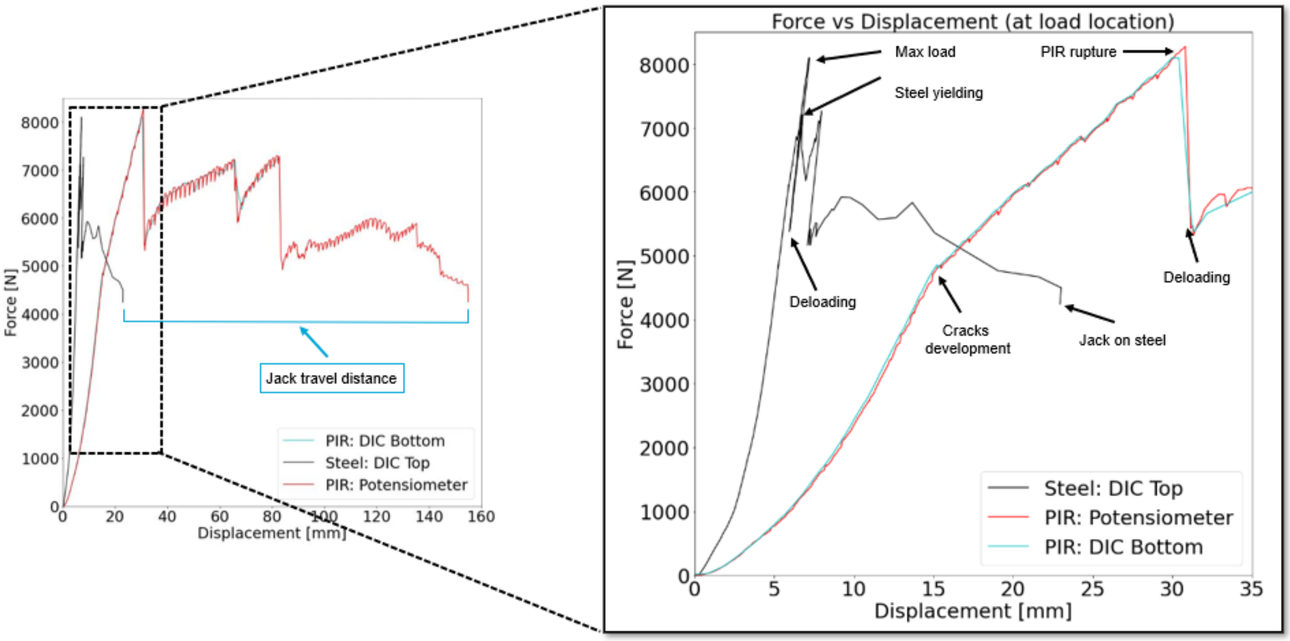

Figure 40 Force vs displacement at load position measured by the string potentiometer.

3.8.2 Results of strain gauges

The results of the same locations the strain gauges are used for the second experiment to compare it to the first experiment, the locations of the strain gauges are shown in Figure 28 for the second experiment. The result of the strains for every location is determined for the load of 6000 N. Similar distribution is observed for loads equal to 4500 N, 3000 N and 1500 N, this is included in Appendix B. Also, the results for the strain development for different loads at the 7 bottom flange locations in the steel is shown in Appendix B. Figure 41 shows the values of the strain gauges that are placed in the bottom flange, meaning the strain gauges that are subjected to tension. These locations are 1 to 9, except location 3 and 7 which were subjected to compression.

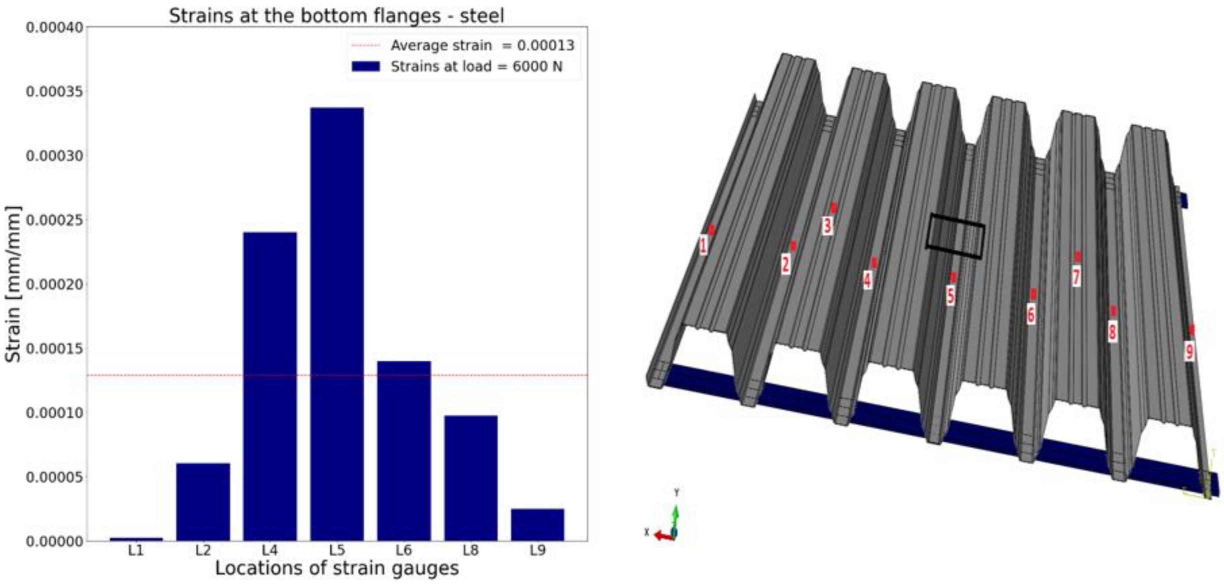

Figure 41 Strains of gauges on the bottom flange of the steel sheet for the load of 6000 N

The distribution of strains is given in Table 7, with the values of strains at these locations and the percentage of each location normalized to the maximum strain.

Table 7 Percentage of each strain value for a location normalized to the maximum value.

Experiment raw: Load case B, Span = 2 m							
Load = 6000 N (at midspan)							
Locations	L1	L2	L4	**L5**	L6	L8	L9
Ribs	1	2	3	**4**	5	6	7
Strains [$*10^{-6}$] [mm/mm]	2.1	60.2	240	**337.1**	139.4	97.4	24.6
Percentage [%]	**0.6**	**17.9**	**71.2**	**100**	**41.4**	**28.9**	**7.3**

The results demonstrate that the strain gauges positioned in the troughs near the applied loads show maximum values, this is shown for the maximum strain value at location 5 whereas the troughs situated farther away from the load application showcase relatively lower values, as anticipated.

3.8.3 Failure load

Seven tests were performed on the same specimen with two tests going to the load up to 1500 N, two tests up to 3000 N, two tests up to 4500 and the seventh tests up to the failure load. The failure of the PIR layer was experienced at 5000 N, as the vertical displacement of the PIR exceeded 10% of the thickness of the PIR layer. The rupture of the PIR occurred when the load reached 8000 N. When 8000 N was reached the steel also failed due to buckling. Figure 42 shows the stages of the specimen when 6000 and 8000 N were reached.

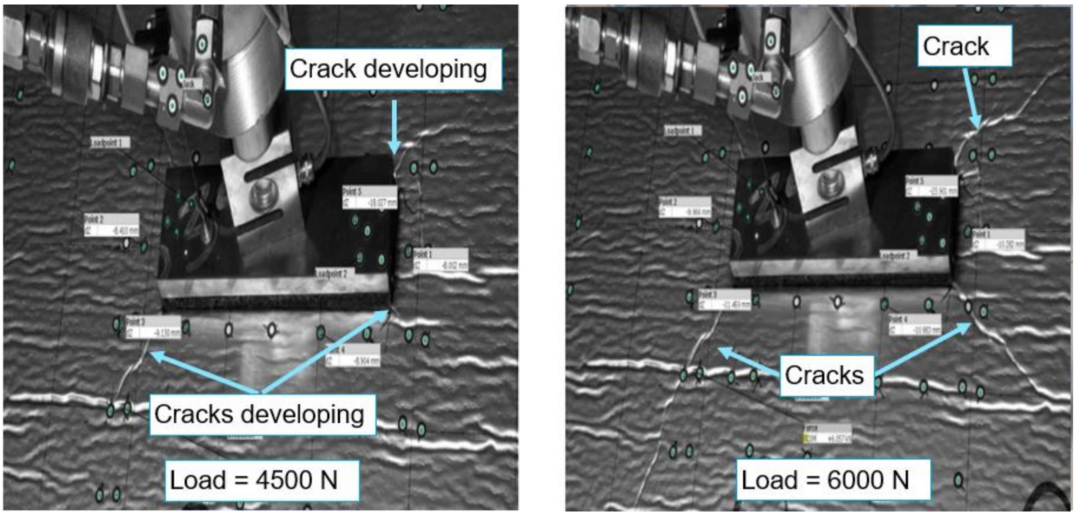

Figure 42 Failure of the PIR (Load case B).

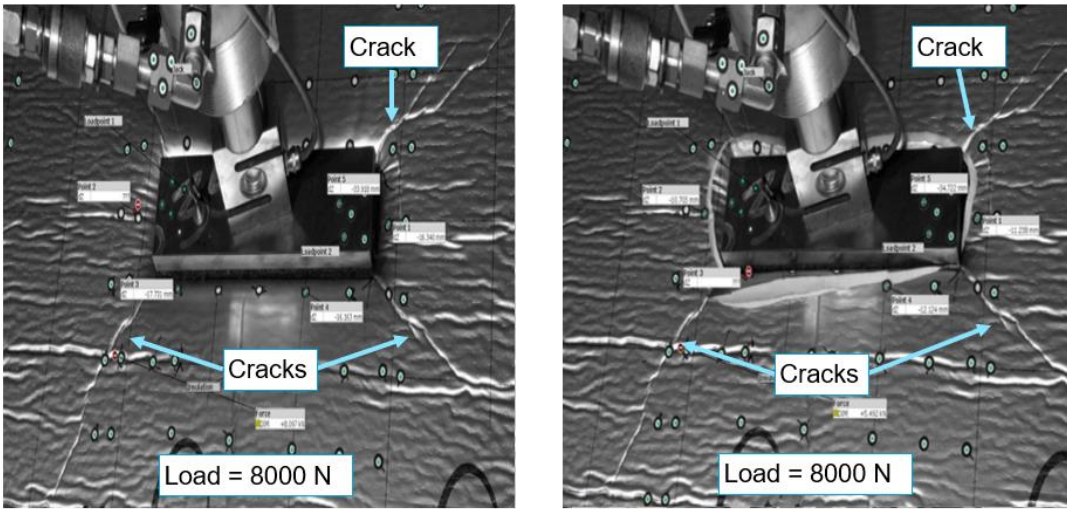

Figure 43 Failure of PIR at 8000 N (Load case B)

It is noticeable that the cracks developed at the corners of the applied rectangular load when the load reached the value of 5000 N. The development of the cracks can be seen in Figure 43 up until the rupture occurs. On the other side, Figure 44 shows the buckling of the steel that is happening at load 8000 N when the rupture of the PIR already occurred.

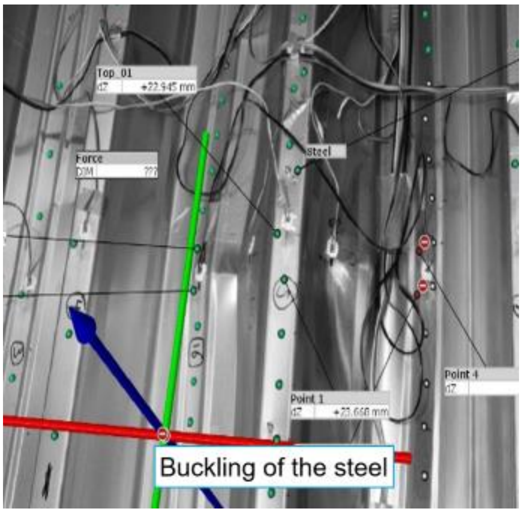

Figure 44 Buckling of the steel (Load case B) after the rupture of the PIR at load 8000 N.

3.8.4 The specimen after the experiment

The specimen was dismantled after testing it up to failure. There is no deformation visible in the bolts that connect the PIR insulation to the steel. Figure 45 shows the steel sheet after dismantling where it is shown that the steel has local buckling at load location. Figures 46 shows the damaged area in the PIR insulation with a circular form occurring, the development of the crack in the PIR insulation is comparable to the first test with a trapezoidal shape being formed along the thickness of the PIR. In this case, the specimen does not have a split at load location, so it is cut in the middle as shown in Figure 46. The trapezium shape starts at 250 mm width at the loading surface and continues to grow until the width reaches 430 mm. There are two angles of failure occurring in the PIR, because of unsymmetric than can be caused by material scattering and properties. The angles are equal to 44° & 18°.

Figure 45 Buckling in the steel at load location.

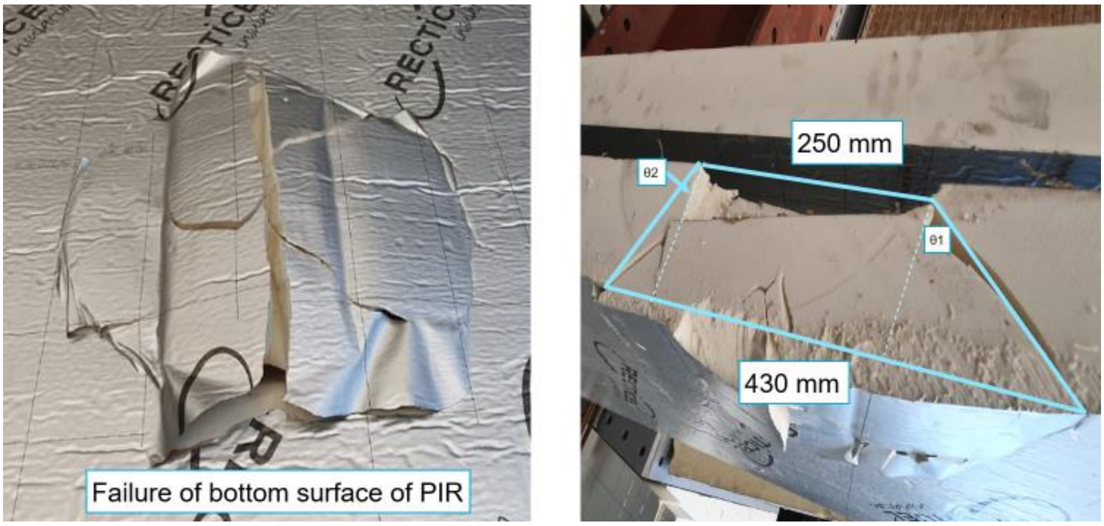

Figure 46 Failure in the PIR at load location.

3.9 Experiments on Determining the E modulus in compression of PIR insulation

Since the E modulus of the PIR insulation is not known, a compression test is performed to get the value of the E modulus in compression. The European EN 826 2013 is followed to perform this experiment. Five specimens are squarely cut with a condition that the width of the specimen should be larger than the thickness (which is 140 mm). The dimensions that are chosen for the square shaped specimens are 200 x 200 mm with the thickness kept as the original 140 mm.

The specimen is compressed a constant rate of displacement equal to 0.1d/min which is equal to 14 mm/min. The compression of the specimen will be applied until the specimen yields or if 10% strain is reached. If the specimen yields, then the stress value is the compressive strength and if the specimen does not yield and 10% strain is reached then a value is registered for the stress that corresponds to 10% strain. The vertical displacement is registered, by sensors on the jack, while the force is being applied. The testing is carried out at room temperature (23+- 5) °C.

The experiment will be repeated after placing 5 other specimens outside for a month to include the outside weather conditions. As a result of the experiment a Force-displacement curve is obtained. The calculation of the E modulus in compression is done with the following formula:

$$E_c = \frac{\sigma}{\varepsilon_c} = \frac{\left(\frac{F}{A_0}\right)}{\left(\frac{X_m}{d_0}\right)} \qquad (3)$$

With:

d_0 = Thickness of specimen [mm]
X_m = Vertical displacement [mm]
F = Applied force [N]
A_0 = Area of specimen [mm2]

Two plates are placed above and under the specimen to give it a sandwich shape. This is done to make sure that all the displacement are applied to the whole surface of the specimen. The bottom plate is fixed which prevents it from moving. A hinge is placed under the loadcell on top of the top plate to make sure that the load is uniformly distributed in the specimen. The load is applied in the vertical direction as the load cells are prevented from moving horizontally by placing timber blocks on the side of the load cell.

Figure 47 Compression test of PIR insulation.

3.10 Results of compression test of PIR insulation

3.10.1 Failure load

Figure 48 show the permanent damage that occurs on all the specimens. The damage is visible when the load of 6250 N is reached as the specimen fails and start yielding. However, the failure of the specimens does not have an arch shape on the sides, but rather a shape that occurs at a certain height. The pictures of PIR05 shows the permanent damage as this 5th specimen is loaded further after the yield point. The height of the failure location is equal to nearly 60 mm all the specimens. Table 8 below shows the failure location height measured from the bottom surface of the specimen.

Table 8 Vertical location of damage in PIR insulation when it is compressed.

Specimen	Vertical distance from the bottom to failure [mm]	Total thickness after testing [mm]
1	59	138
2	58	139
3	57	140
4	60	138
5	60	139

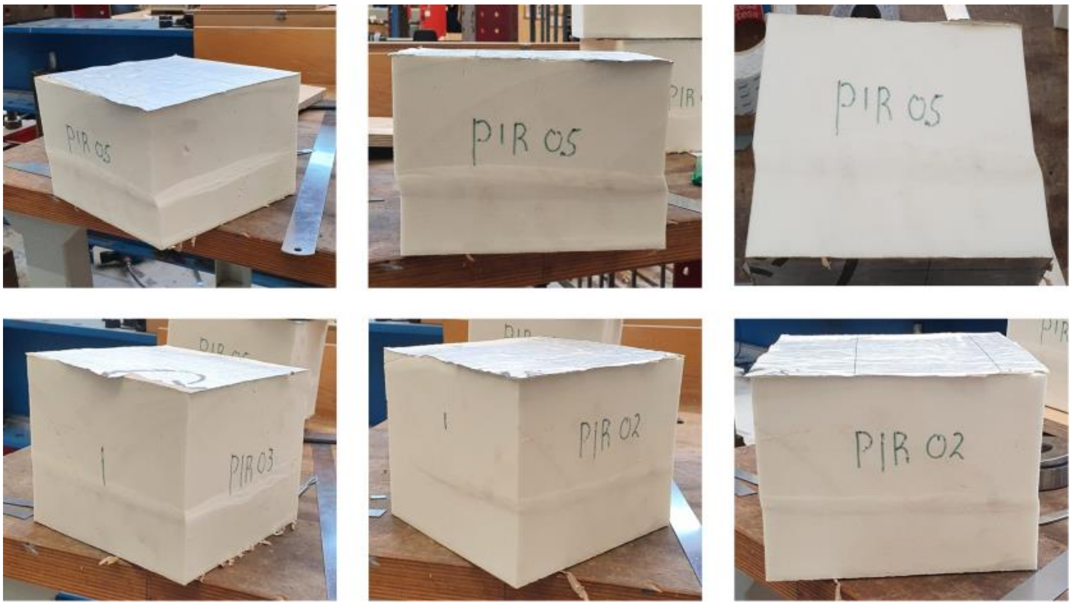

Figure 48 PIR specimens after compression testing.

3.10.2 Calculation of E modulus in compression for PIR insulation

Figure 49 shows the applied force against the vertical displacement of the 5 specimens, it is noticeable to see that the specimens yield at the load of 6250 N. This is observed while testing as the damage has occurred at this load. According to EN 826 2013, the value of X_m can be determined by Figure 51, which implies that the specimen yields at a certain load. The E modulus in compression is calculated after getting the value of X_m.

The value of X_m is gained from Figure 49 by taking the yield displacement and subtracting it from the initial displacement as described in EN 826 2013, the initial displacement is the intersection of the linear part of the curve with the horizontal axis. X_m is equal to 6 mm – 0.4 mm = 5.7 mm. The thickness d0 is equal to 140 mm. Compression stress is calculated by taking the force where the yielding of the specimen occurs and dividing it by the area of the specimen. The value of F is equal to 6250 N while the applied area A_0 is equal to 200*200 mm^2.

Equation 3 (from EN 826 2013) is the division of the compression by the compressive strain (in vertical direction) which gives a value for the E modulus in compression. After filling in the variables in equation 3, the E modulus in compression is calculated and it is equal to **3.9 MPa**. This E modulus value is expected for room temperature since there is a known expected range of 0-4 MPa for the E modulus of the PIR insulation.

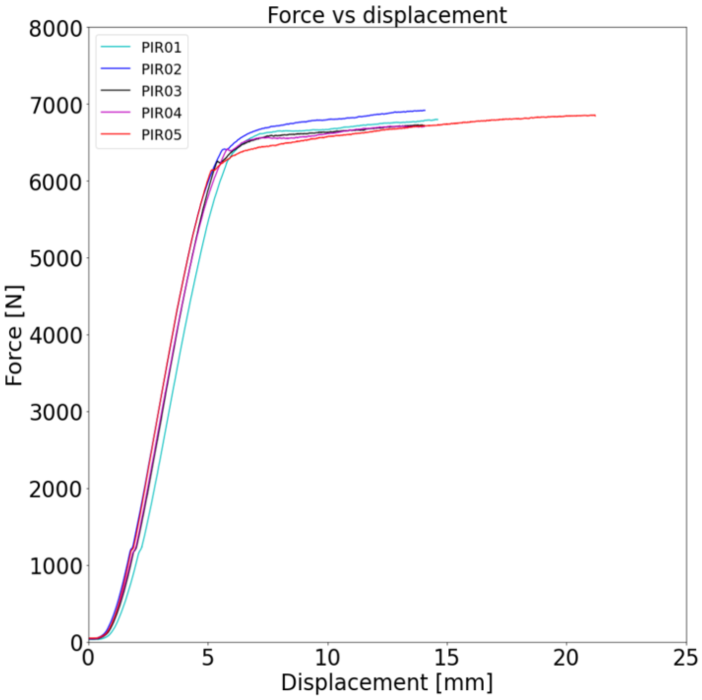

Figure 49 Force vs displacements for PIR insulation specimens when they are compressed.

4 The linear numerical model

4.1 Linear FEM model

A model is created using ABAQUS (Simulia, 2021) which is a finite element software that allows the user to create numerical models using the finite element method. The two SAB135R/90 steel sheets are modelled as solid elements as one sheet consisting of 6 ribs with double thickness of 2*0.88 mm at the middle to simulate the overlapping that is caused by the connection of two steel sheets of 3 ribs, this is shown in Figure 50. The geometry of the steel sheets is given in Figure 19. The two strips are placed under the steel sheet and the PIR insulation is placed above the steel sheet. Linear analysis is performed to predict the load distribution in the elastic phase. The mesh size of the quadrangle element in the steel sheet is equal to 5 mm and 30 mm for PIR insulation. The strip mesh size is equal to 5 mm.

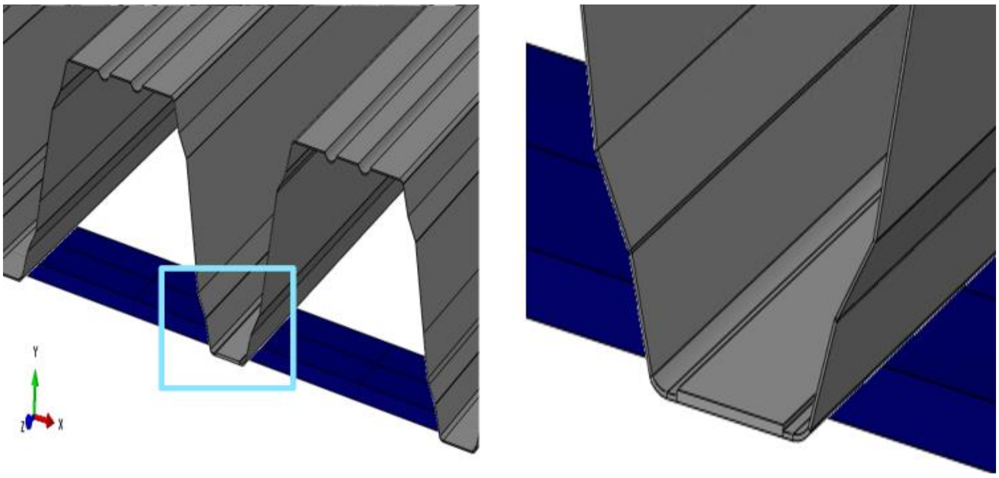

Figure 50 Two steel sheets of 3 ribs are assumed to be one sheet with 6 ribs with double thickness in the middle.

4.1.1 Interactions, mesh, and material properties

Since the model consist of 3 elements being steel sheet, strips, and PIR insulation layer, it is required to define interaction between these elements. The interaction between the bottom surface of the steel sheet and the top surface of the strips is defined as hard contact with “tie” constraints attached to the surfaces. When two surfaces have tie constraint in the model, it means that these two surfaces are fused together. The interaction between the steel sheet and the PIR insulation layer cannot defined with tie constraint because the connection is done with bolts in the experimental specimen. However, the bolts in the experimental are used only to keep the PIR layer on top of the steel. The steel has smooth surface which means that the bolts have minimum effect on force distribution. To make a simple interaction between the PIR and the steel sheet in the finite element model, four very small surfaces of area equal to 400 mm^2 are created on the bottom surface of the PIR. The four small, created areas of the PIR, are tied with the corresponding top surface of the steel sheet, this is shown in Figure 51. Besides this, a general interaction between two surfaces of the PIR and the steel is defined with a penalty given in the form of very low friction coefficient that is equal to 0.1. The model is run with different values of friction coefficient to see whether the results are influenced by the value of the friction coefficient. Thus, the model is tested with a friction coefficient of 0.01 and it showed similar results as the model with 0.1 friction coefficient, which is expected because the steel has smooth surface interaction with the PIR which eliminates friction effects. The mesh that is used for the steel and the PIR is uniform mesh with the size of 30 mm for the PIR and 15 mm for the steel.

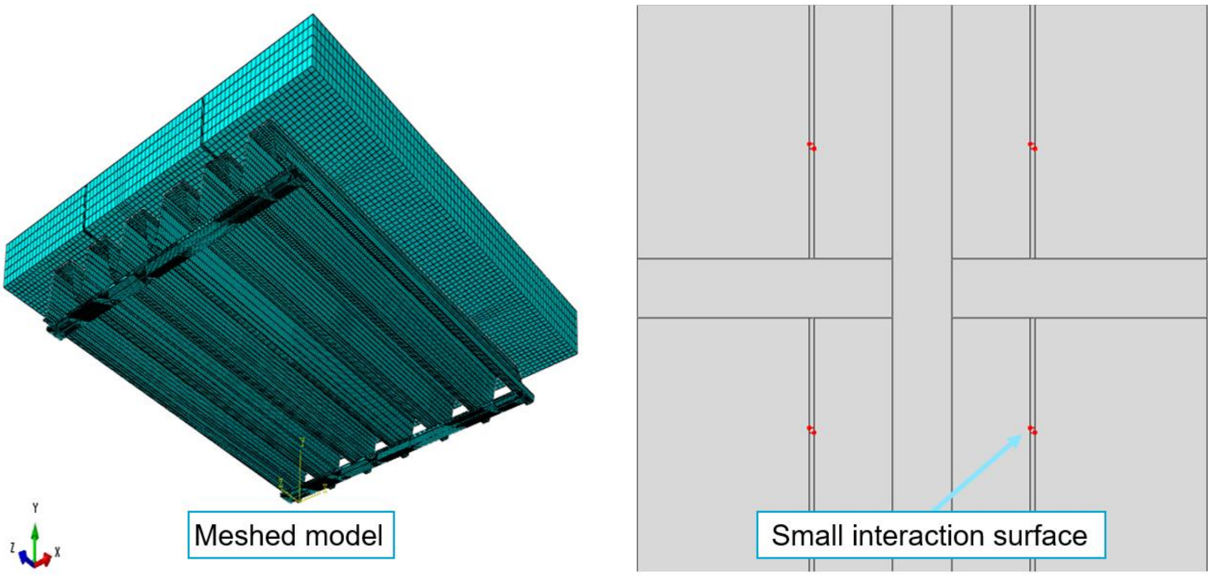

Figure 51 Meshed model (on the left) and interactions in bottom surface of PIR (on the right).

4.1.2 Loading and boundary conditions

The self-weight of the PIR and the steel sheet is calculated, and it is applied as a load that is upwards. This is done because the self-weight works against the applied surface loads. The surface loads are upwards in the experiment, so when looking at the model the situation in the experiment is upside down. The surface loads are applied downwards in the model and are placed on the load positions that corresponds to the positions of the loads in the experiment. Figure 52 show the applied loads on the model.

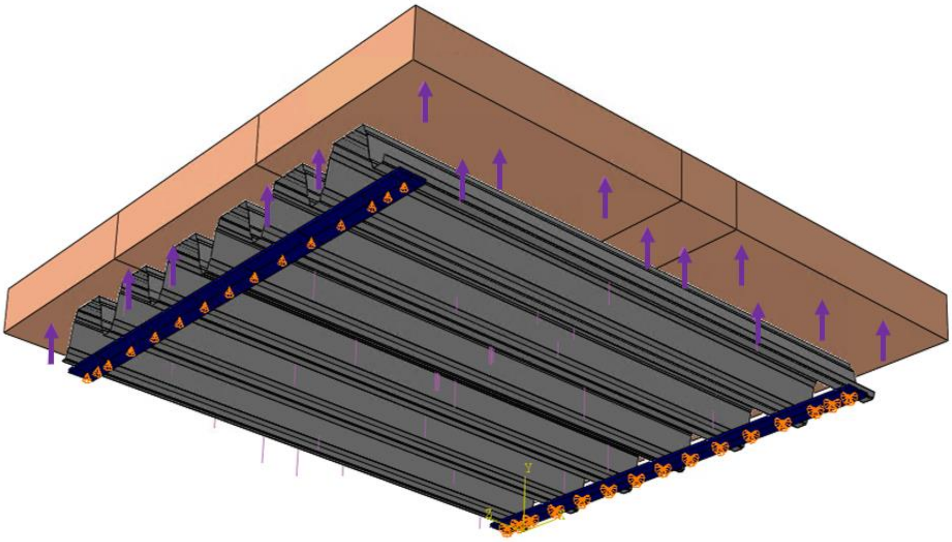

Figure 52 FEM model of the specimen.

Figure 53 shows what the loads are on the specimen. The two strips are simply supported in the model, as the middle line of the bottom surface of the surface is pinned in x, y and z directions. The amount of self-weight is calculated, and the value of the surface load F is inserted. The calculation of the mass is performed by ABAQUS, which calculates the volume inserted and then multiply it by the density. The value of F equals 2*4000 N for load case A and 6000 N for load case B.

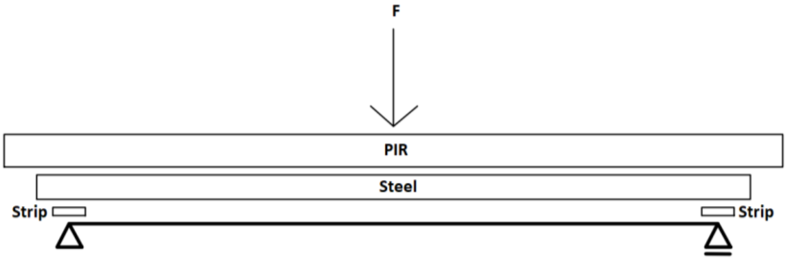

Figure 53 The loads on the specimen.

The results of the support reactions of the model should be equal to the calculation of Table 9 below:

Table 9 Support reactions calculation.

Part	**Mass [kg]**	**Weight [kN]**	**Length of part [m]**
PIR	25	0.24525	2.4
Steel sheet	41	0.40221	2.2
Total	66	0.64746	
Total / 2	48	0.32373	
Vertical support reaction		0.32373 + F/2	

4.2 Results of the linear FEM model

4.2.1 Strains

The stains at midspan at 7 different locations of the bottom flange are given in Figure 54 with Table 10 and 11 showing how much percent each location has when is normalized to the maximum strain.

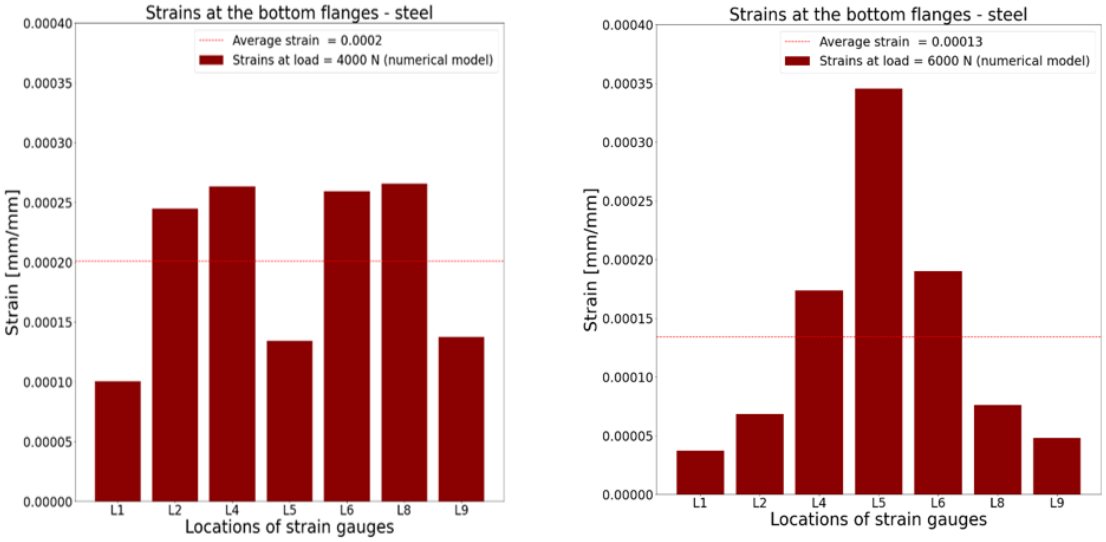

Figure 54 Strains at midspan from the model, Load case A (left) & Load case B (right)

Table 10 Percentage of each strain value for a location normalized to the maximum value.

Model: Load case A, Span = 2 m							
Load = 2*4000 N (at midspan)							
Locations	L1	L2	L4	L5	L6	**L8**	L9
Ribs	1	2	3	4	5	**6**	7
Strains [*10^{-6}] [mm/mm]	100.2	244.7	263.1	134	259	**265.6**	137.2
Percentage [%]	**37.7**	**92.1**	**99.1**	**50.5**	**97.5**	**100**	**51.7**

Table 11 Percentage of each strain value for a location normalized to the maximum value.

Model: Load case B, Span = 2 m							
Load = 6000 N (at midspan)							
Locations	L1	L2	L4	**L5**	L6	L8	L9
Ribs	1	2	3	**4**	5	6	7
Strains [*10^{-6}] [mm/mm]	37	68.5	173.7	**348**	189.8	75.8	48
Percentage [%]	**10.6**	**19.7**	**49.9**	**100**	**54.5**	**21.8**	**13.8**

4.2.2 Shear stress in the PIR

As shown previously, the PIR layer failed in punching shear failure mode. The shear stresses developed in the PIR insulation can be analysed using the Tresca criterion, which relies on the maximum ($\sigma 1$) and minimum ($\sigma 2$) principal stress values obtained from the finite element method (FEM) results. In ABAQUS, the equation below is used to generate shear stress contours. Figures 55 and 56 present cross-sectional cuts (through 140 mm thickness of PIR) below the loading surface for both load case A and B, illustrating the development of shear stresses in the elastic phase of the PIR insulation.

$$\tau = \frac{(\sigma 1 - \sigma 2)}{2} \qquad (4)$$

In Figures 57 and 58, the distribution of shear stress is shown at an angle of 32.7 degrees for both load case A and load case B. It is important to note that this angle is obtained from the elastic PIR insulation layer, which remains undamaged in the numerical models. In contrast, the angles obtained from the experiments represent the angle of failure of the PIR, resulting from both shear stresses and the development of cracks caused by imperfections in the PIR.

For load case A, the experiment yielded a symmetrical shape with an angle of failure of 39 degrees, whereas load case B resulted in an asymmetrical shape with angles of failure equal to 18 degrees and 44 degrees. These differences in the angles of failure demonstrate the influence of the load distribution and the specific conditions on the behaviour of the PIR insulation layer in the experiments.

Figure 55 Shear stress at cross section cut under the load (LCA, step 2: load = 4000 N)

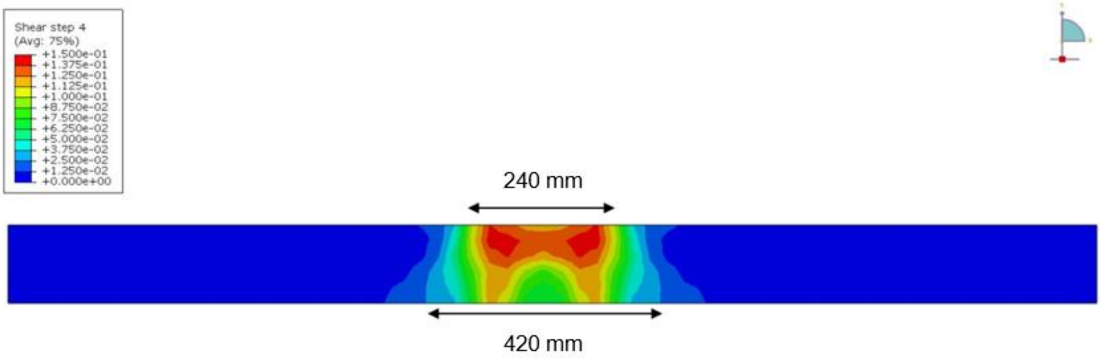

Figure 56 Shear stress at cross section cut under the load (LCB, step 4: load = 8000 N).

4.3 Linear numerical model vs experiments

4.3.1 Load case A

The results that are obtained by the experiments is compared to the results of the finite element model. A sensitivity analysis is performed where only E modulus of PIR layer is changed. The rest of the parameters are kept the same with E modulus of the steel being equal to 210000 MPa and Poisson's ratio of 0.3. For the PIR layer the E modulus is given in the literature as a range between 0 to 4 MPa with a Poisson's ratio of 0.25.

Strains: Experiment vs Model

Table 13 shows the results of the experiment compared to the model results with the usage of the value of E = 4 MPa for the PIR insulation. Here the strains of the 7 locations of the experiment are compared to the element value of the steel in the model at the same location. Table 12 shows the chosen element in the model for each location.

Table 12 Elements in the model for each strain gauge location of the experiment.

Location 1	Location 2	Location 4	Location 5	Location 6	Location 8	Location 9
Element 89155	Element 73278	Element 57844	Element 47254	Element 30796	Element 14184	Element 808

Figure 57 shows the ratio between the experimental and numerical values for each strain gauge location. The experimental values are bigger than numerical if the value of the ratio is bigger than one. Ideally, the ratio should be equal to one, so whenever the ratio is close to one the better the comparison results between the model and the experiment.

Table 13 Experimental vs Numerical values.

Load case A, Span = 2 m							
Load = 2*4000 N (at midspan)							
Locations	L1	L2	L4	L5	L6	L8	L9
Ribs	1	2	3	4	5	6	7
Experimental strains [*10-6] [mm/mm]	128.4	291.9	280	126.4	255.8	329.7	193.7
Numerical strains [*10-6] [mm/mm]	100.2	244.7	263.1	134	259	265.6	137.2
Ratio = Experimental / Numerical	**1.28**	**1.19**	**1.06**	**0.94**	**0.98**	**1.24**	**1.41**
Difference	+28 %	+19 %	+6 %	-6 %	-2 %	+24 %	+41%

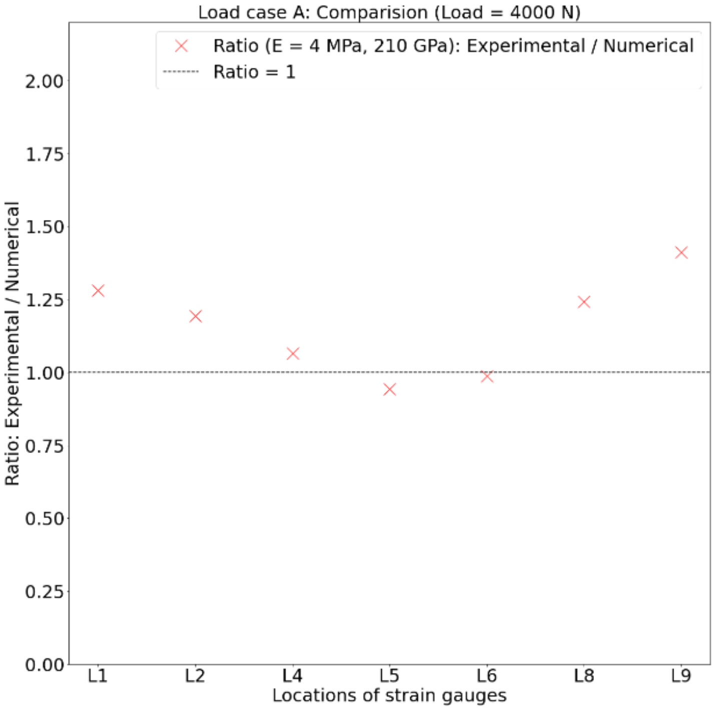

Figure 57 Ratio: Experimental / Numerical values.

Displacements: Experiment vs Model

PIR

The results that are obtained from the experiment at load location, which is measured by the potentiometers and the DIC (at jack) is compared to the finite element model results at the same location. The results are shown in Figure 58. In this figure, it is shown the experimental value is not linear at the beginning up until reaching 500 N. This can be explained by the behaviour of the rubber that is applied below the loading jack. The rubber gives nonlinear displacement at the beginning until a certain point. Figure 58 shows the same experimental results with the exclusion of the effect of the rubber by drawing a tangent line to the linear part of the experimental value where the E modulus stabilises. The tangent line is shifted to 0,0 by subtracting the initial displacement caused by the nonlinear start of the experimental curve.

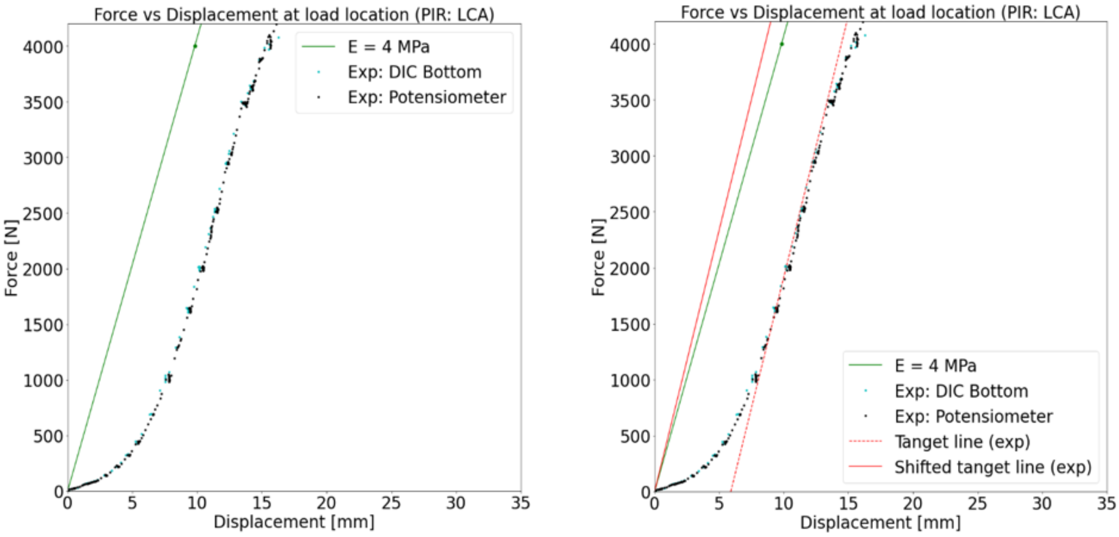

Figure 58 Experimental vs Numerical displacements (PIR).

Steel

A comparison is made between the experimental and numerical values for the displacement on point 4 which is at load location. The results are shown in Figure 59. The experimental values do not have a linear relation at the beginning. As stated before, this is because of the rubber that is applied on top of the PIR layer underneath the loading jack. Figure 59 shows the same experimental results with the exclusion of the effect of the rubber by drawing a tangent line to the linear part of the experimental value where the E modulus stabilises. The tangent line is shifted to 0,0 by subtracting the initial displacement caused by the nonlinear start of the experimental curve. The slope of the green line (model) is equal to 1333 N/mm, while the slope of the red line (experiment) is equal to 903 N/mm.

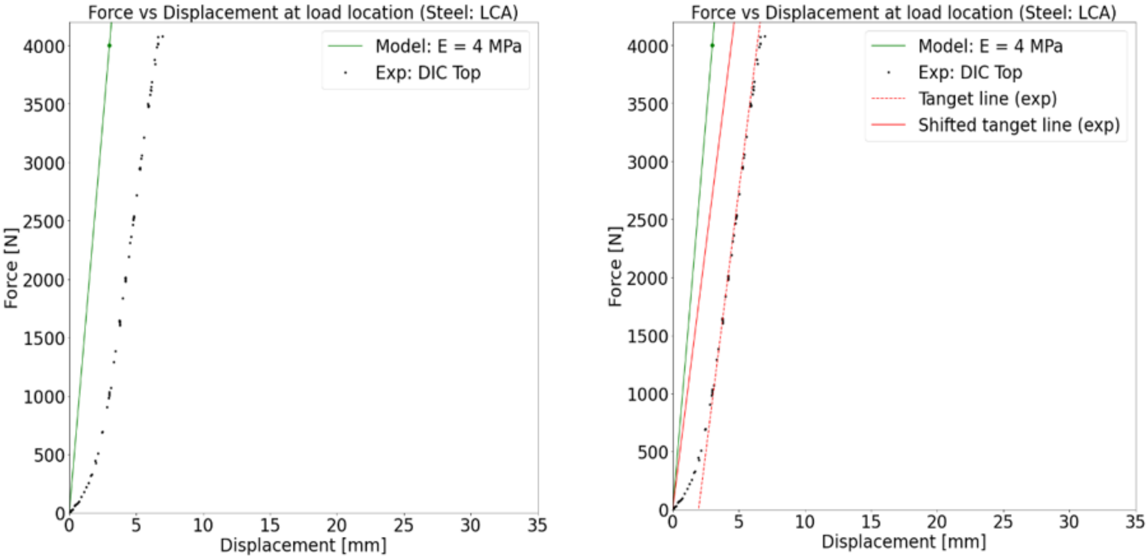

Figure 59 Experimental vs Numerical displacements (steel).

4.3.2 Load case B

Strains: Experiment vs Model

Table 15 shows the results of the experiment compared to the model results with the usage of the value of E = 4 MPa for the PIR insulation. Here the strains of the 7 locations of the experiment are compared to the element value of the steel in the model at the same location. Table 14 shows the chosen element in the model for each location.

Table 14 Elements in the model for each strain gauge location of the experiment.

Location 1	Location 2	Location 4	Location 5	Location 6	Location 8	Location 9
Element 89155	Element 73278	Element 57844	Element 47254	Element 30796	Element 14184	Element 808

Figure 60 shows the ratio between the experimental and numerical values for each strain gauge location. The experimental values are bigger than numerical if the value of the ratio is bigger than one. Ideally, the ratio should be equal to one, so whenever the ratio is close to one the better the comparison results between the model and the experiment. The experimental values for L1 and L9 are not representative, as the strain gauges show nearly zero values. This could be since these strains are far from the location of load application, and the presence of imperfections in the steel may prevent the activation of these strains. The values for L1 and L2, which are necessary for calculating the ratio between experimental and numerical results, are not included. Figure 81 in the annex illustrates that the strains at these locations remain close to zero for all applied loads.

Table 15 Experimental vs Numerical values.

Load case B, Span = 2 m							
Load = 6000 N (at midspan)							
Locations	L1	L2	L4	L5	L6	L8	L9
Ribs	1	2	3	4	5	6	7
Experimental strains [*10-6] [mm/mm]	2.1	60.2	240	**337.1**	139.4	97.4	24.6
Numerical strains [*10-6] [mm/mm]	37	68.5	173.7	348	189.8	75.8	48
Ratio = Experimental / Numerical		**0.88**	**1.38**	**0.97**	**0.73**	**1.28**	
Difference		+12 %	+38 %	-2 %	-27 %	+28 %	

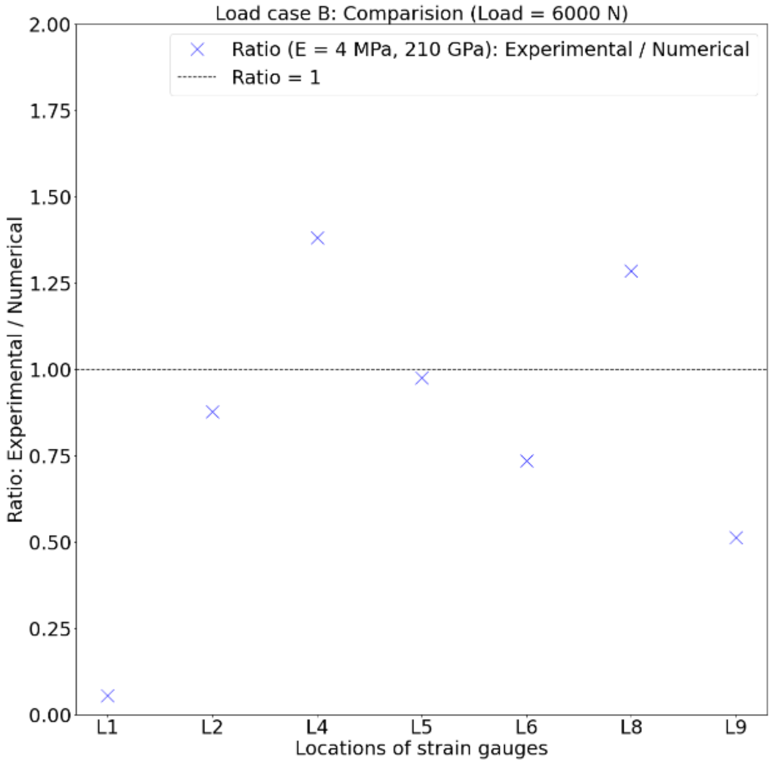

Figure 60 Ratio: Experimental / Numerical values.

Displacements: Experiment vs Model

PIR

The results that are obtained from the experiment at load location, which is measured by the potentiometers and the DIC (at jack) is compared to the finite element model results at the same location. The results are shown in Figure 61. In this figure, it is visible to see that the experimental value is not linear at the beginning. This can be explained by the behaviour of the rubber that is applied below the loading jack. The rubber gives nonlinear curves for the displacement at the beginning. Figure 61 shows the same experimental results with the exclusion of the effect of the rubber by drawing a tangent line to the linear part of the experimental value where the E modulus stabilises. The tangent line is shifted to 0,0 by subtracting the initial displacement of 5 mm caused by the nonlinear start of the experimental curve.

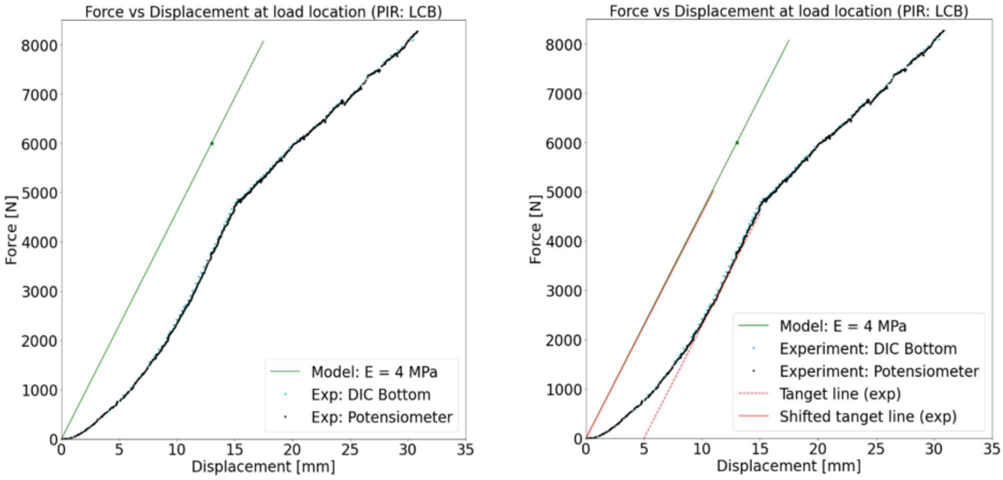

Figure 61 Experimental vs Numerical displacement (PIR).

Steel

A comparison is made between the experimental and numerical values for the displacement at load location. The results are shown in Figure 62. The experimental values do not have a linear relation at the beginning. As stated before, this is because of the rubber that is applied on top of the PIR layer underneath the loading jack. Figure 62 the same experimental results with the exclusion of the effect of the rubber by drawing a tangent line to the linear part of the experimental value where the E modulus stabilises. The tangent line is shifted to 0,0 by subtracting the initial displacement caused by the nonlinear start of the experimental curve. The slope of the green line (model) is equal to 3400 N/mm, while the slop of the red line (experiment) is equal to 1600 N/mm.

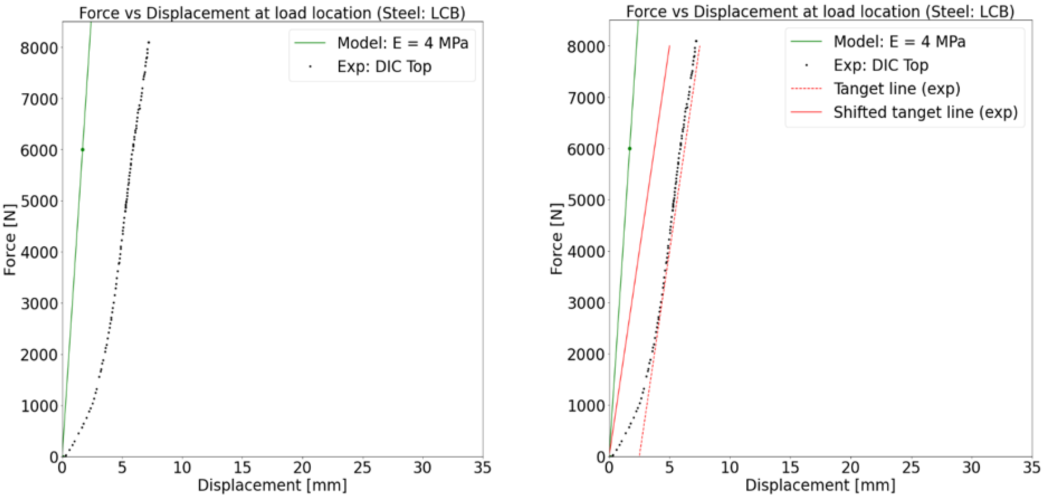

Figure 62 Experimental vs Numerical displacement (steel).

5 Expanding model span

5.1 Changing the span from 2 to 6 meters

An expansion of the model is required to accommodate the dimensions and span of a larger model. The distance between the support reactions has been increased from 2 meters to 6 meters. The width of the steel sheet in the x direction remains unchanged, maintaining the same cross section consisting of 6 ribs. Additionally, the PIR insulation layer is placed on top of the steel sheet using the same interaction definition as the small-scale model with a 2-meter span. Four small rectangular shapes measuring 20 by 20 mm are created on the bottom of the PIR layer and attached to the top surface of the steel sheet, like the small-scale model. Figure 63 illustrates the model for the larger span of 6 m. The boundary conditions are also kept identical to the small-scale model, and the application of load remains the same for both load case A and B, with surface loads applied at midspan as shown in Figure 63 and Figure 64.

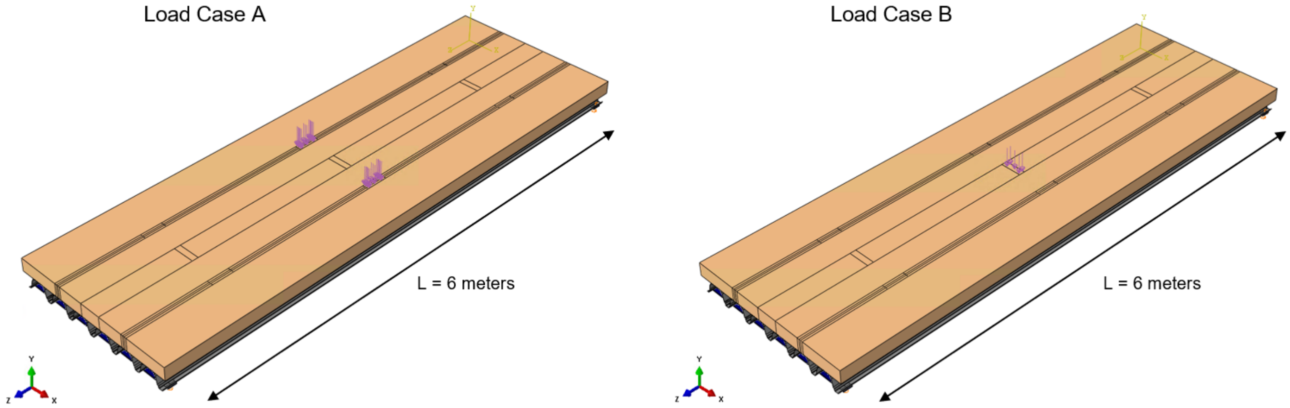

Figure 63 Load case A (left) and Load case B (right).

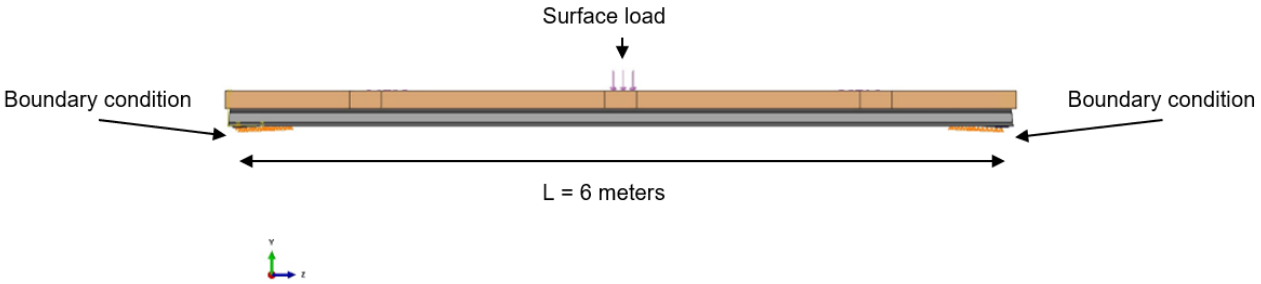

Figure 64 Large model – side view.

5.2 Results: Loading at midspan (2-meter vs 6-meter model)

Tables 16-19 provide an overview of the results obtained from both the small and large-scale models for load cases A and B. The load is applied at L=3 m, corresponding to the midspan location. Strain values are measured for each rib, and the strain distribution is presented as a percentage value relative to the maximum strain observed.

In load case B, where the load is applied at rib 5, this rib contributes 100% to the load distribution, serving as the reference for the adjacent ribs. With the increase in span from 2 to 6 meters in the large-scale model, the midspan location moves further away from the support reactions. As a result, the steel sheet at midspan becomes less rigid. This explains the increased strains and their influence when the midspan is farther from the support reactions. Moreover, in load case B, ribs 3 and 5 show higher percentage values in the large-scale model, indicating their greater contribution to the load distribution.

In load case A, the load is applied between ribs 2 and 3, as well as between ribs 5 and 6, with rib 8 having the highest value set as 100%. Analysing the contribution of these ribs reveals a similar effect as in load case B. The percentage values of ribs 2 and 3, as well as the region between ribs 5 and 6, are higher in the large-scale model compared to the small-scale model. Additionally, the adjacent ribs near the load locations demonstrate increased percentage values, suggesting a more evenly distributed load as the span is increased.

Table 16 Distribution of strains of the small model (LCA) at midspan.

Model (span = 2 m): LCA, self-weight excluded							
Load = 2 * 4000 N							
Locations	1	2	4	5	6	**8**	9
Ribs	1	2	3	4	5	**6**	7
Strain [$*10^{-6}$] [mm/mm]	109.8	257.2	269.1	138.7	265.1	**279.5**	152.1
Percentage [%]	**39.3**	**92**	**96.3**	**49.6**	**94.8**	**100**	**54.4**

Table 17 Distribution of strains of the large model (LCA) at midspan.

Model (span = 6 m): LCA, self-weight excluded							
Load = 2 * 4000 N							
Locations	1	2	4	5	6	**8**	9
Ribs	1	2	3	4	5	**6**	7
Strain [$*10^{-6}$] [mm/mm]	482	728	741	564	657	**761**	617
Percentage [%]	**63.3**	**95.7**	**97.4**	**74.1**	**86.3**	**100**	**81.1**

Table 18 Distribution of strains of the small model (LCB) at midspan.

Model (span = 2 m): LCB, self-weight excluded							
Load = 6000 N							
Locations	1	2	4	5	6	**8**	9
Ribs	1	2	3	4	5	**6**	7
Strain [*10^{-6}] [mm/mm]	41.7	75.5	186.8	**350**	202	83.8	54
Percentage [%]	**11.9**	**21.6**	**53.4**	**100**	**57.7**	**23.9**	**15.4**

Table 19 Distribution of strains of the large model (LCB) at midspan.

Model (span = 6 m): LCB, self-weight excluded							
Load = 6000 N							
Locations	1	2	4	**5**	6	**8**	9
Ribs	1	2	3	**4**	5	**6**	7
Strain [*10^{-6}] [mm/mm]	272	360	547	**791**	554	379	339
Percentage [%]	**34.4**	**45.5**	**69.2**	**100**	**70**	**47.9**	**42.9**

5.3 Results: Loading at three locations (6-meter model)

Figure 65 shows that the distance between the rubber feet is 2 meters. As a result, there are three possible surface load locations that can be applied within a 6-meter span. Figures 65 and 66 illustrate the application of loads for both load case A and B, incorporating three load application positions: L = 1 meter, L = 3 meters (midspan), and L = 5 meters. This arrangement transforms the problem from a simply supported scenario with a single load at midspan to a simply supported problem with three loads.

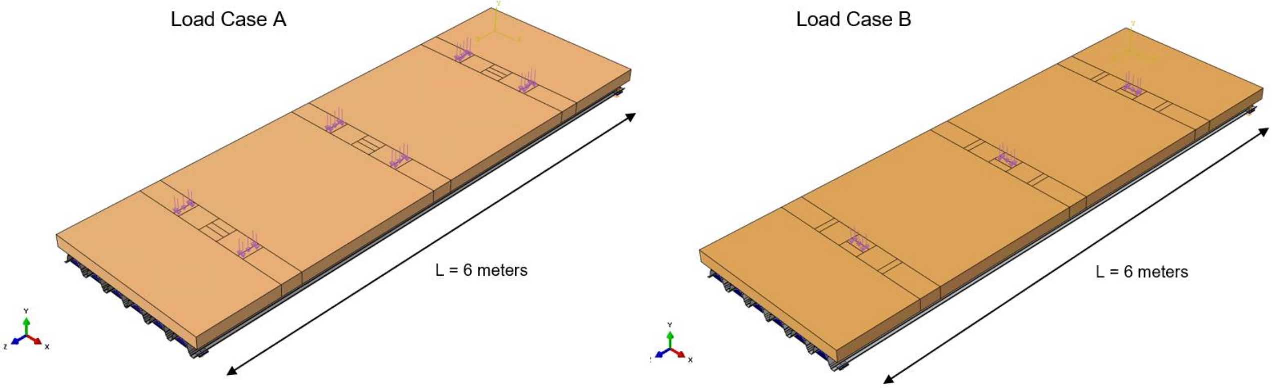

Figure 65 Load case A (left) and Load case B (right).

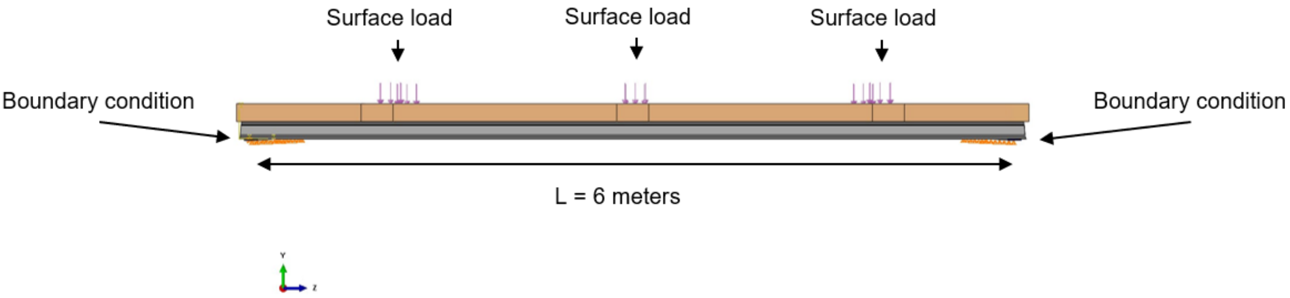

Figure 66 Large model (three surface loads) (side view).

Tables 20-25 show the strain values of each rib for 3 different locations, as stated before the first location is at L=1 m, the second at L=3 m (mid span) and the third is at L=5. Simultaneously applying loads at three locations results in a more balanced load distribution among the ribs, as illustrated in the tables below. The strain values, normalized to the maximum strain, indicate that the load distribution at midspan is more evident when compared to the case with a single load. The loads at L=1 m and L=5 m have an influence on the distribution at midspan, resulting in increased strains in the adjacent ribs to the rib where the load is applied.

Table 20 Distribution of strains at L = 3 m (LCA) midspan.

Model (span = 6 m): LCA, self-weight excluded							
Load = 3* (2 * 4000) N							
L = 3 m							
Locations	1	2	4	5	6	**8**	9
Ribs	1	2	3	4	5	**6**	7
Strain [$*10^{-6}$] [mm/mm]	894.7	1156	1185.8	1028	1215	**1223**	1121
Percentage [%]	**73.2**	**94.5**	**97**	**84.1**	**99.3**	**100**	**91.7**

Table 21 Distribution of strains at L = 1 m (LCA).

Model (span = 6 m): LCA, self-weight excluded							
Load = 3* (2 * 4000) N							
L = 1 m							
Locations	1	2	4	5	6	**8**	9
Ribs	1	2	3	4	5	**6**	7
Strain [$*10^{-6}$] [mm/mm]	524	709	729	616	740	**757**	638
Percentage [%]	**69.2**	**93.7**	**96.3**	**81.4**	**97.8**	**100**	**84.3**

Table 22 Distribution of strains at L = 5 m (LCA).

Model (span = 6 m): LCA, self-weight excluded							
Load = 3* (2 * 4000) N							
L = 5 m							
Locations	1	2	4	5	6	**8**	9
Ribs	1	2	3	4	5	**6**	7
Strain [$*10^{-6}$] [mm/mm]	590	704	728	649	772	**791**	719
Percentage [%]	**74.6**	**89**	**92**	**82**	**97.6**	**100**	**90.9**

Table 23 Distribution of strains at L = 3 m (LCB) midspan.

Model (span = 6 m): LCB, self-weight excluded							
Load = 3* (6000) N							
L = 3 m							
Locations	1	2	4	**5**	6	8	9
Ribs	1	2	3	**4**	5	6	7
Strain [*10^{-6}] [mm/mm]	539.7	686.3	895.3	**1138.4**	908.5	722.9	670.1
Percentage [%]	**47.4**	**60.3**	**78.6**	**100**	**79.8**	**63.5**	**58.9**

Table 24 Distribution of strains at L = 1 m (LCB).

Model (span = 6 m): LCB, self-weight excluded							
Load = 3* (6000) N							
L = 1 m							
Locations	1	2	4	**5**	6	8	9
Ribs	1	2	3	**4**	5	6	7
Strain [*10^{-6}] [mm/mm]	299	395	555	**725**	581	422	359
Percentage [%]	**41.2**	**54.5**	**76.6**	**100**	**80.1**	**58.2**	**49.5**

Table 25 Distribution of strains at L = 5 m (LCB).

Model (span = 6 m): LCB, self-weight excluded							
Load = 3* (6000) N							
L = 5 m							
Locations	1	2	4	**5**	6	8	9
Ribs	1	2	3	**4**	5	6	7
Strain [*10^{-6}] [mm/mm]	437	437	514	**636**	551	506	525
Percentage [%]	**68.7**	**68.7**	**80.8**	**100**	**86.6**	**79.6**	**82.5**

6 The nonlinear numerical model

6.1 Load application: on the PIR and directly on the steel sheet

In Figure 67, the nonlinear model is shown without including imperfections. Two scenarios are considered: in the first, PIR insulation is included, whereas in the second, it is excluded. In the former scenario, the load is applied to the PIR insulation, while in the latter, it is applied directly to the steel sheet. The same two load cases of the experiments are considered for each scenario. The objective is to see the impact of the PIR insulation on the failure load. The PIR insulation is modelled as an elastic material due to the challenges involved in capturing its plastic properties and cracks. This way the failure load is obtained for the case with and without the inclusion of PIR insulation.

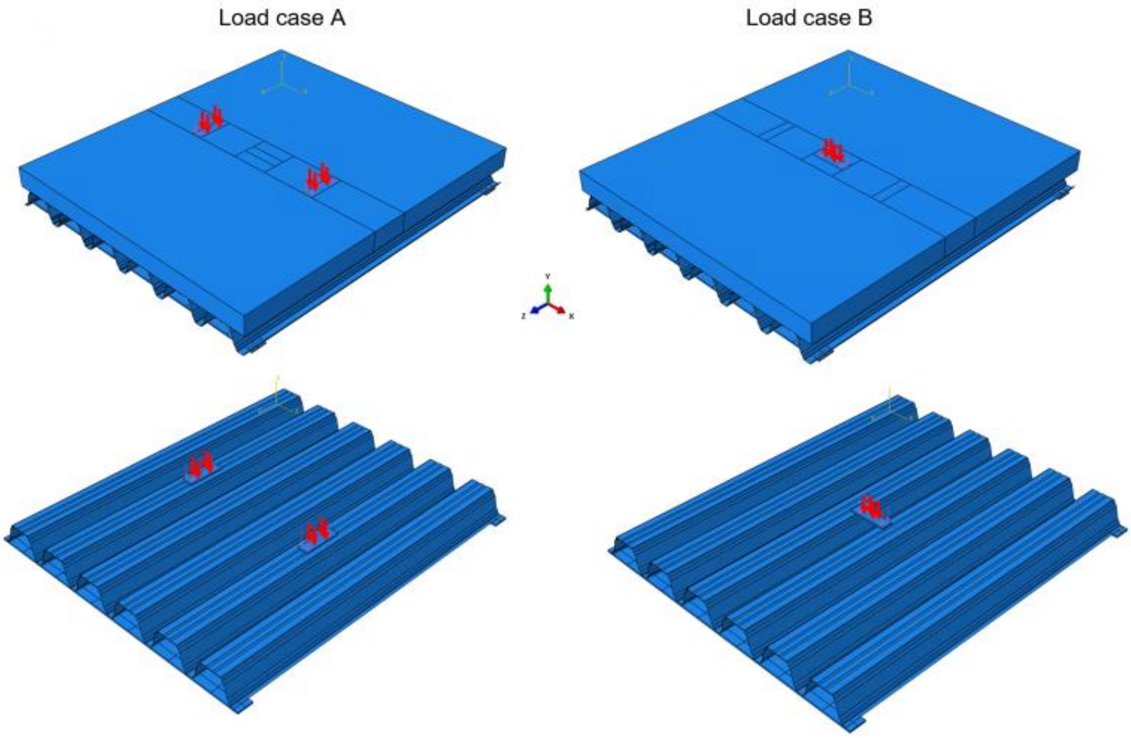

Figure 67 Load application on the PIR and on the steel sheet.

6.2 Results of the nonlinear models

The graphs in Figure 68 shows the force vs displacement curves illustrating the comparison between two scenarios. As stated before, the difference between the two scenarios is the inclusion of the PIR insulation. PIR insulation is assumed to remain in the elastic phase when it is considered, while the non-linear model incorporates plastic properties and includes non-linearity in the steel sheet. Both scenarios have the same load cases as the ones in the experiments. For load case A, the measurement node is situated at the top flange of the load location, while for load case B, it is positioned at the bottom flange due to the absence of a top flange beneath the load location in this specific case. The results, shown in Figure 68, reveal that the nonlinearity for load case A occurs at approximately 12000 N when the load is applied on the PIR insulation and at 8000 N when the load is applied directly on the steel sheet. Similarly, for load case B, the nonlinearity occurs approximately at 12000 N when the load is applied on the PIR insulation and 8000 N when the load is applied directly on the steel sheet. The PIR insulation is modelled as linear elastic, which means that the damage is not included in the analysis. A horizontal line is drawn at load of 6250 N, this load is obtained from the compression test results of Figure 49. This is done to illustrate that the red curve in Figure 68 (when accounting for PIR insulation) cannot be effectively compared with the experimental results once this load is exceeded. For design purposes, it is recommended not to factor in scenarios involving PIR insulation for loads exceeding the 6250 N limit.

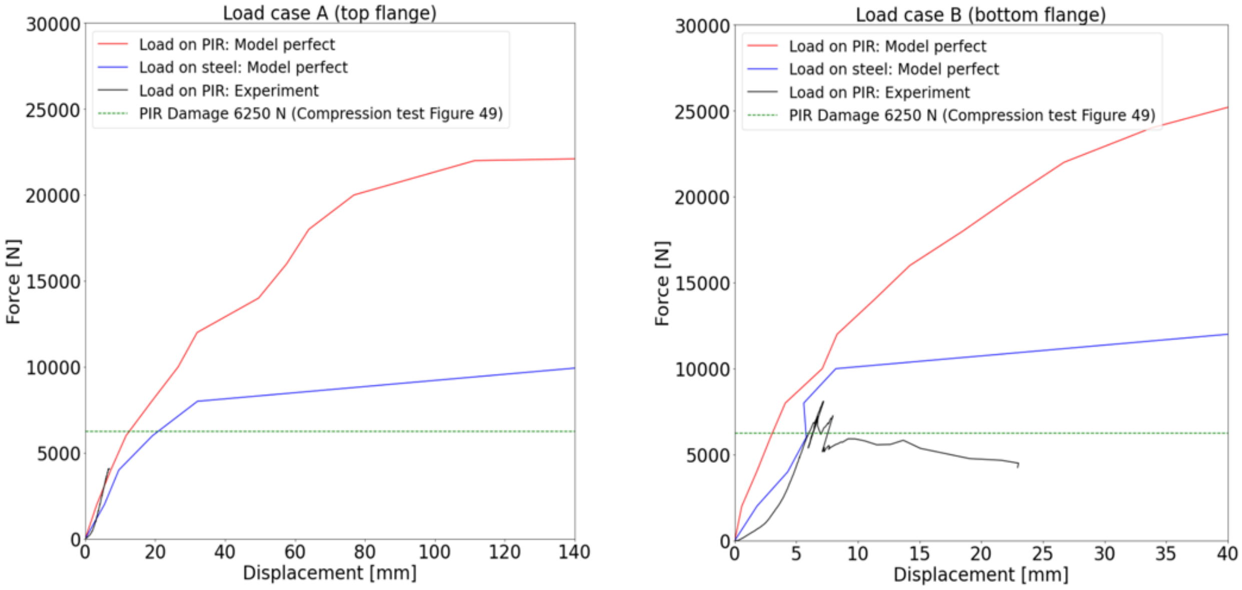

Figure 68 Force vs displacement (Load on steel vs Load on PIR).

A key question arises regarding whether the load that triggers nonlinearity in the steel sheet will also lead to plastic deformation. To address this, the longitudinal stress in the z direction is monitored at each loading step in the numerical model that includes the PIR. The yield strength of 355 MPa is surpassed when 10000 N is applied for load case A (step 5) and 10000 N (step 5) is applied for load case B. This aligns with the occurrence of nonlinear behaviour illustrated in Figure 70; however, it shows that the yield strength is surpassed at 10000 N instead of 12000 N. When the load is directly applied on the steel, plasticity appear at a load of 4000 N for both load case A and B as the yield strength is surpassed. The nonlinear behaviour can be explained due to geometric instability in flanges and webs in the region of the where external load is applied accompanied with plastic deformation where the stress reaches the yield stress 355MPa.

The longitudinal stress contours are given in Figure 69 and 70, where it is shown that the yield strength is surpassed at the top flange of load case B while the measured experimental point at the bottom flange does not show plasticity at this load.

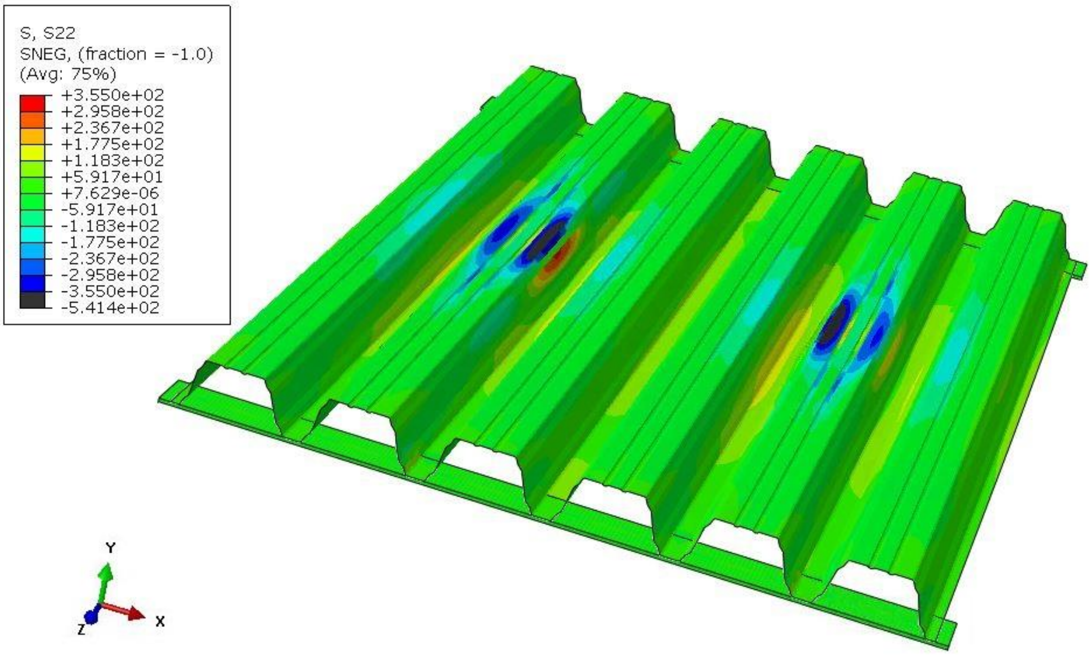

Figure 69 longitudinal stress (z direction) (PIR included) - LCA: Step 5, Load = 10000 N.

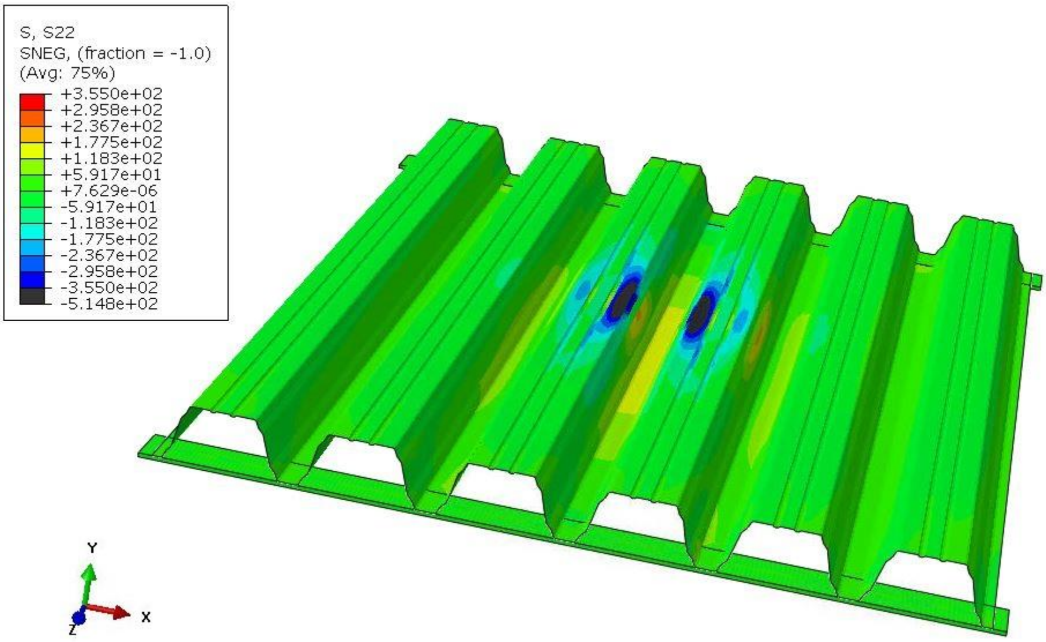

Figure 70 longitudinal stress (z direction) (PIR included) - LCB: Step 5, Load = 10000 N.

7 Buckling and post buckling analysis

The cold-formed steel sheet used in this study does not possess perfect geometry due to the rolling process. Even slight asymmetries can result in unsymmetrical outcomes due to the thinness of the steel sheets. Cold-formed sections have imperfections as they are not produced with precise rolling techniques. Because of these imperfections, the steel sheet displays non-symmetrical behaviour when subjected to bending. The top flanges of the steel sheet may not align precisely on the same level surface, leading to differences in the connection between the PIR (Polyisocyanurate) insulation and the steel. In certain areas, gaps may exist between the steel sheet and the PIR insulation, causing variations in force transfer. The presence of initial gaps results in delayed load transfer from the PIR to the steel as the PIR must first push against the gap before interacting with the steel surface.

In the finite element method model, an assumption is made of a perfect geometry without any imperfections, which is verified through experimental validation in the previous chapter. To incorporate imperfections in the steel sheet, a detailed analysis of buckling and post-buckling is conducted. During the buckling analysis, an axial load is applied to the steel sheet to induce multiple buckling mode shapes. A specific magnitude of displacements associated with a selected buckling mode shape is then implemented as the initial geometry in the post-buckling analysis model. This approach allows for the inclusion of imperfections represented by the buckling mode shape. The updated geometry of the steel sheet is utilized in the analysis.

7.1 Linear buckling analysis

To determine the buckling shape of the corrugated steel sheet, an axial load is applied at the edge of the steel sheet in the z-direction. The boundary conditions for the analysis are set as follows.
The edge of the steel sheet where the load is applied has fully clamped boundary conditions, except for the z-direction, which is left free to allow for the buckling shape to emerge. On the opposite side, the other edge surface is fully clamped. The side edges are simply supported, with zero displacement in the x-direction, to simulate the continuity of the steel sheet. Figure 71 shows the application of the boundary conditions. For this analysis, only the steel sheet is considered, excluding the PIR insulation and the strips. It should be noted that the steel sheet used in this study has symmetric geometry in terms of the edges, this is done to obtain a symmetrical buckling shape.

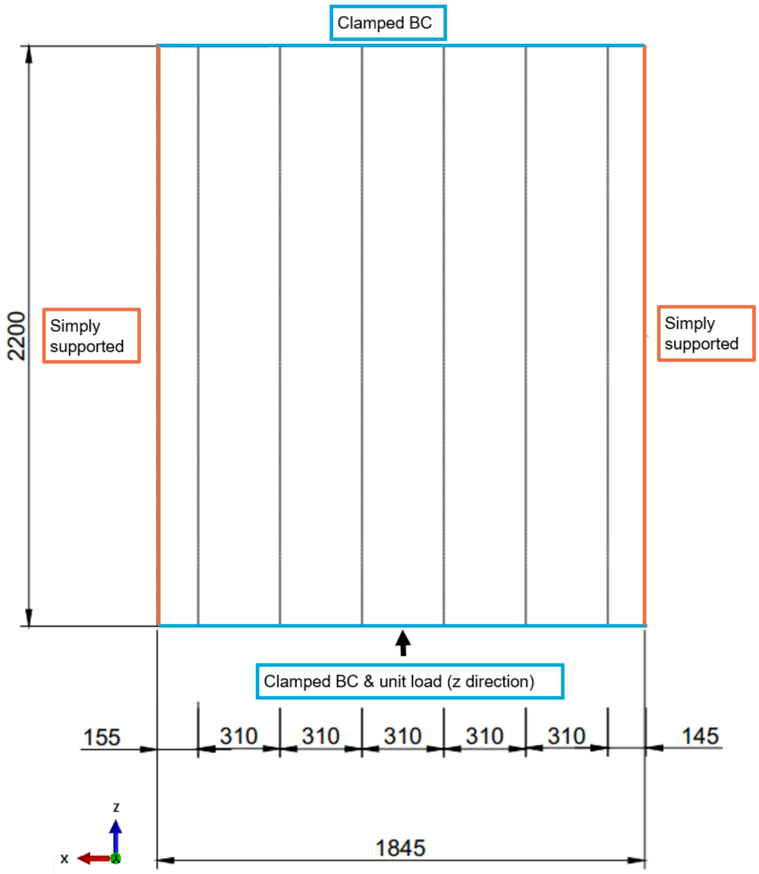

Figure 71 Boundary conditions on the steel sheet, loaded axially in the z direction.

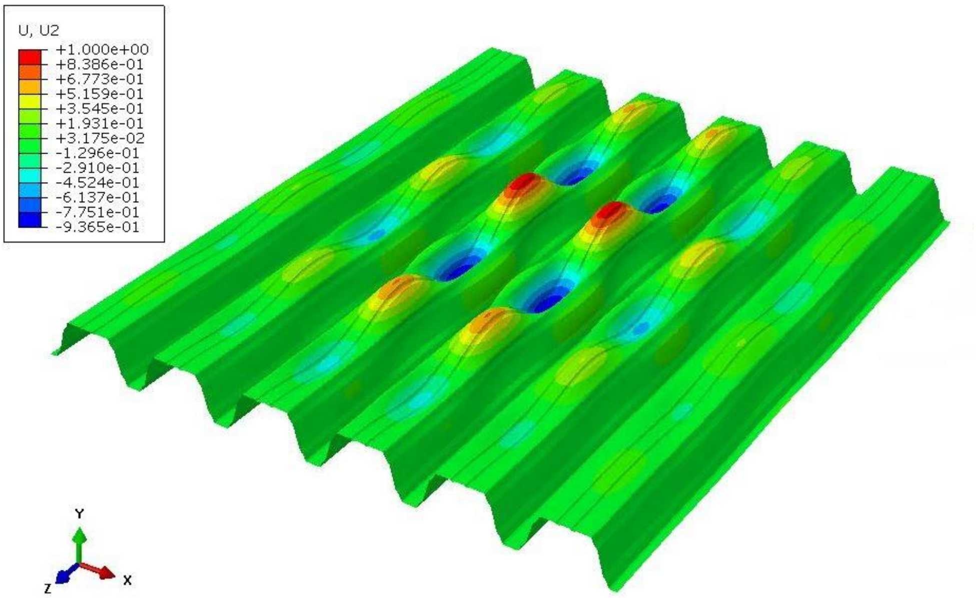

Figure 72 Buckling mode shape (symmetric sheet) – BC on the sides (x=0).

7.2 Post buckling analysis

To conduct a post-buckling analysis, the buckling mode shape is imported to introduce imperfections in the geometry of the steel sheet. These imperfections are characterized displacements resulting from the buckling of the steel sheet, with a certain magnitude, which is then applied to the steel sheet. The initial geometry of the steel sheet is modified by incorporating these displacement magnitudes.

To perform the post-buckling analysis, a separate model is created by copying the buckling analysis model and making necessary adjustments. The primary adjustment involves changing the step solver to a static general explicit solver instead of linear perturbation. Additionally, the boundary conditions, interactions, and load application are reverted to their original configurations from the linear elastic model with the loads being applied directly on the steel sheet.

The post-buckling analysis primarily focuses on the steel sheet, because of the implementation of yield strength and imperfections. The PIR insulation is excluded in the post buckling analysis. Figures 73 and 74 provide visual representations of the post-buckling behaviour of the steel sheet for load cases A and B. Here, the strips are hidden from the presentation. These illustrations offer a clear understanding of how the steel sheet responds during the post-buckling phase.

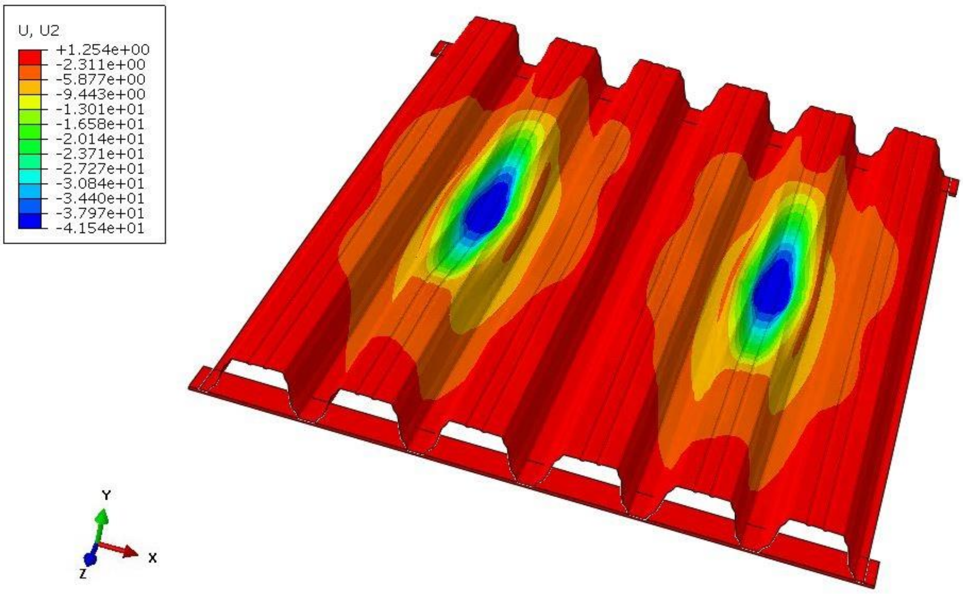

Figure 73 Post buckling (Load case A) Step 4, Load = 8000 N.

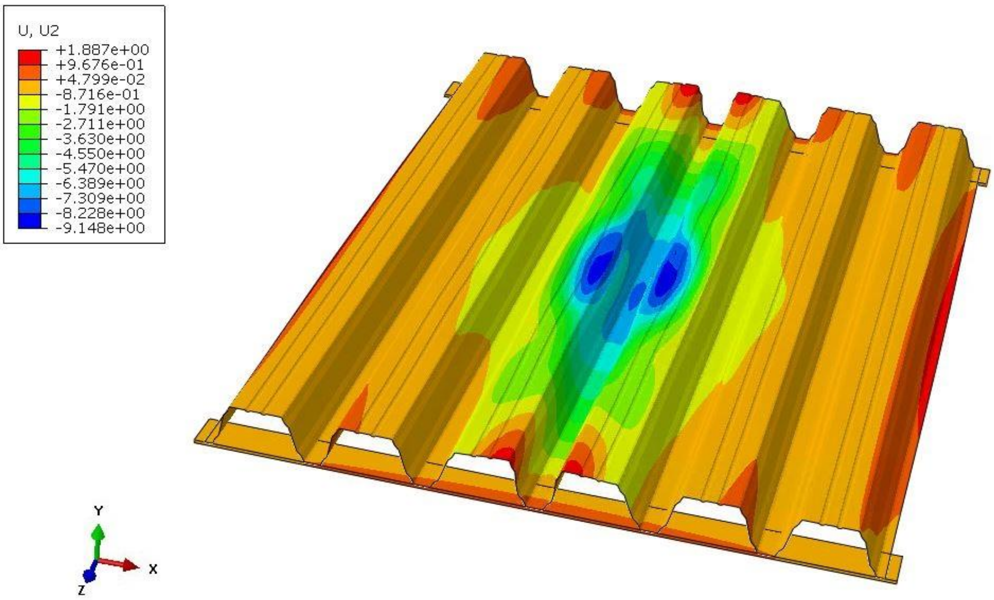

Figure 74 Post buckling (Load case B) Step 4, Load = 8000 N.

Figure 75 illustrates the comparison between the steel sheet with perfect geometry and the steel sheet with included imperfections, representing a magnitude of B/200 which is equal to 10 times the displacement caused by the selected buckling shape (shown in Figure 72). The value of B is equal to 2000 mm which is equal to the distance between the two vertical supports. The measurement point for load case A is located at the top flange, while for load case B, it is positioned at the bottom flange. Figure 75 demonstrates that the curve of the imperfect geometry displays a lower load versus displacement response compared to the perfect geometry. It is important to note that the load is applied directly to the steel, which is not the case in the experiments. In the experiments the yielding and buckling of the steel occur after the PIR insulation is ruptured. Notably, the buckling shape primarily shows buckling in the top flange and minimal buckling in the bottom flange. For load case B, both curves show similar values until 4000 N is reached, indicating no significant difference in the behaviour of the sheet with the included imperfections. However, after 4000 N is reached, for load case B, small difference is observed in the post buckling behaviour which is shown in the right graph of Figure 75. This small difference can be attributed to the limited impact of the implemented imperfections from the buckling mode shape on the bottom flange.

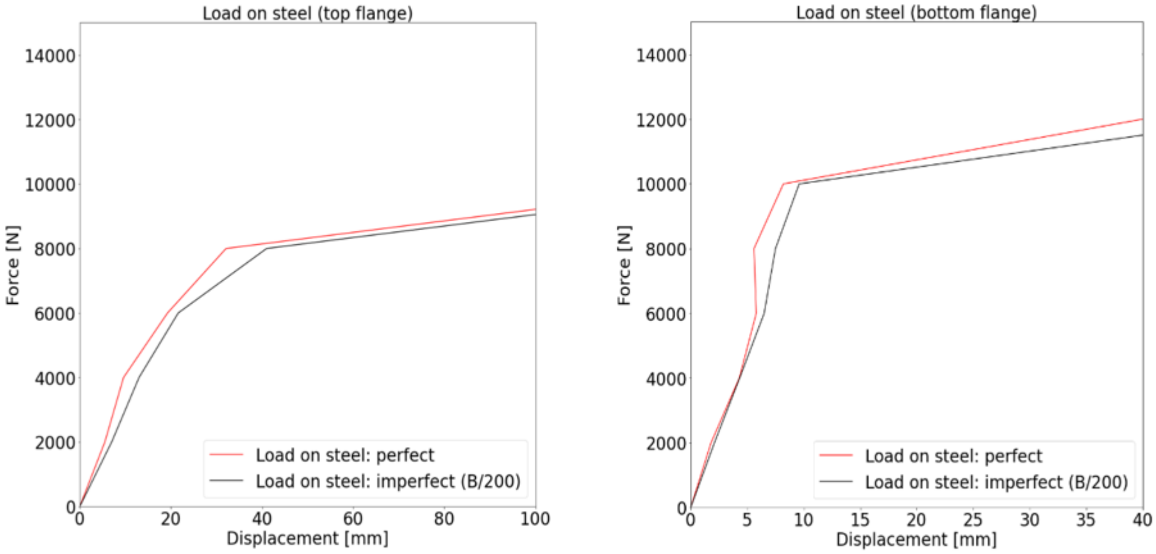

Figure 75 perfect vs imperfect geometry results (Load applied directly on the steel).

8 Discussion

8.1 Experiments vs Linear numerical model

The experiments and the linear model demonstrate a clear surface load distribution within the steel sheet. Strain gauges positioned at the bottom flanges of each rib at midspan offer valuable data regarding this load distribution. By comparing the strain values obtained from the experiments to the corresponding locations in the numerical model, the influence of adding the PIR layer on the distribution of surface loads into the steel sheet is set. The experimental results not only serve to validate the linear model but also highlight the dominant role of the PIR insulation. It is observed that the PIR insulation layer undergoes rupture without any plastic deformation occurring in the steel sheet. A specific maximum load is determined for each loading condition that can be applied to the PIR insulation layer.

The numerical model presents a more symmetrical pattern of strains compared to the experimental setup. This difference can be attributed to the absence of imperfections in the model, whereas they exist in the tested specimen.

Table 26 and 27 illustrate the surface load distribution for both applied loading conditions, with the strain values of each rib normalized relative to the maximum strain value. The tables demonstrate the involvement of multiple ribs in transferring the load from the surface to the support reaction. The measured strains indicate that the highest values are observed at the load location, as expected. However, it is important to note that the load is not exclusively carried by a single rib, but rather distributed among multiple ribs. This load distribution provides design flexibility, allowing engineers to consider a more realistic distribution of applied load. Without taking load distribution into account, engineers would have to design each rib to individually bear the entire load, potentially resulting in unnecessary material and design requirements. By considering load distribution, the applied load on each rib can be reduced, as neighbouring ribs actively contribute to load support when a load is applied to a specific rib.

Table 26 Percentage of each strain value for a location normalized to the maximum value.

Model: Load case A, Span = 2 m							
Load = 2*4000 N (at midspan)							
Locations	L1	L2	L4	L5	L6	**L8**	L9
Ribs	1	2	3	4	5	**6**	7
Strains [*10^{-6}] [mm/mm]	100.2	244.7	263.1	134	259	**265.6**	137.2
Percentage [%]	**37.7**	**92.1**	**99.1**	**50.5**	**97.5**	**100**	**51.7**

Table 27 Percentage of each strain value for a location normalized to the maximum value.

Model: Load case B, Span = 2 m							
Load = 6000 N (at midspan)							
Locations	L1	L2	L4	**L5**	L6	L8	L9
Ribs	1	2	3	**4**	5	6	7
Strains [*10^{-6}] [mm/mm]	37	68.5	173.7	**348**	189.8	75.8	48
Percentage [%]	**10.6**	**19.7**	**49.9**	**100**	**54.5**	**21.8**	**13.8**

The linear model provides the opportunity to investigate the influence of the roof structure's span on the distribution of surface loads at midspan.

8.2 Increasing the span of the linear model

By changing the span from 2 to 6 meters while keeping other variables such as interactions, material properties, and cross-section geometry constant, notable changes in load distribution are observed.

In the larger model with an increased span, it is observed that the adjacent ribs to the load location contribute more significantly. This can be attributed to the steel being less rigid at the load location due to the increased distance from the supports. This means that less force is required in the longer span model to cause the same level of strains and deformation observed in the smaller 2-meter model. Despite the increased span, it is anticipated that the PIR will still govern the failure, and the predetermined failure load obtained from the small-scale experiment will remain applicable for rupturing the PIR. This assumption implies that the steel is assumed to remain in the elastic phase.

Table 28 Distribution of strains of the large model (LCA) at midspan.

Model (span = 6 m): LCA, self-weight excluded							
Load = 2 * 4000 N							
Locations	1	2	4	5	6	**8**	9
Ribs	1	2	3	4	5	**6**	7
Strain [*10^{-6}] [mm/mm]	482	728	741	564	657	**761**	617
Percentage [%]	**63.3**	**95.7**	**97.4**	**74.1**	**86.3**	**100**	**81.1**

Table 29 Distribution of strains of the large model (LCB) at midspan.

Model (span = 6 m): LCB, self-weight excluded							
Load = 6000 N							
Locations	1	2	4	**5**	6	**8**	9
Ribs	1	2	3	**4**	5	**6**	7
Strain [*10^{-6}] [mm/mm]	272	360	547	**791**	554	379	339
Percentage [%]	**34.4**	**45.5**	**69.2**	**100**	**70**	**47.9**	**42.9**

8.3 Increasing the span of the linear model and applying loads on multiple locations

Another scenario in the model involves a larger-scale application with a 6-meter span, where loads are applied at multiple locations on the PIR instead of exclusively at midspan. The results of this load application demonstrate a different load distribution at midspan compared to the previous scenario. In this case, the strains at midspan are influenced not only by the load at midspan but also by the effects of load distribution at L = 1 and L = 5 meters. As a result, the load is distributed more evenly among the ribs. This is evident when examining the normalized strain values, which indicate the contributions of various ribs to the overall load distribution.

Table 30 Distribution of strains at L = 3 m (LCA) midspan.

Model (span = 6 m): LCA, self-weight excluded							
Load = 3* (2 * 4000) N							
L = 3 m							
Locations	1	2	4	5	6	**8**	9
Ribs	1	2	3	4	5	**6**	7
Strain [*10^{-6}] [mm/mm]	894.7	1156	1185.8	1028	1215	**1223**	1121
Percentage [%]	**73.2**	**94.5**	**97**	**84.1**	**99.3**	**100**	**91.7**

Table 31 Distribution of strains at L = 3 m (LCB) midspan.

Model (span = 6 m): LCB, self-weight excluded							
Load = 3* (6000) N							
L = 3 m							
Locations	1	2	4	**5**	6	8	9
Ribs	1	2	3	**4**	5	6	7
Strain [*10^{-6}] [mm/mm]	539.7	686.3	895.3	**1138.4**	908.5	722.9	670.1
Percentage [%]	**47.4**	**60.3**	**78.6**	**100**	**79.8**	**63.5**	**58.9**

8.4 The nonlinear model

The results reveal that nonlinearity for load case A occurs at 12000 N when the load is applied on the PIR insulation and at 8000 N when the load is applied directly on the steel sheet. Similarly, for load case B, the nonlinearity occurs at 12000 N when the load is applied on the PIR insulation and 8000 N when the load is applied directly on the steel sheet. The obtained from the compression tests is equal to 6250 N. For design purposes, it is recommended not to factor in scenarios involving PIR insulation for loads exceeding the 6250 N limit.

The results reveal a nonlinear force versus displacement curve in the steel at the load location. The occurrence of nonlinearity in the steel sheet indicates an ultimate load, although it is important to note that the PIR insulation layer remains in the elastic linear phase. Modelling the nonlinearity and cracks of the PIR insulation layer presents challenges and the experimental results show that the PIR insulation layer experiences rupture first and governs the failure of the specimen. It should be noted that the obtained load when nonlinearity occurs in the numerical model is higher than the load observed in the experiments. This difference can be attributed to the presence of multiple imperfections in the experimental specimens, whereas the numerical model includes only a magnitude of a buckling mode shape as an imperfection.

8.5 Buckling and post buckling

The buckling and post-buckling analyses are conducted to incorporate the magnitude of the buckling mode shape, resulting from axial loading, as initial imperfections in the steel sheet model. The post-buckling model incorporates plastic properties and considers the nonlinear development of the geometry. The comparison between the steel sheet with perfect geometry and the sheet with included imperfections reveals that the imperfect geometry causes a higher load-displacement response. This difference can be attributed to the influence of the implemented imperfections, particularly affecting the top flange. Load case B shows similar behaviour for both geometries, suggesting limited impact from the imperfections on the bottom flange. On the other hand, load case A demonstrates a difference because the imperfections are taken from the buckling shape that shows buckling at the top flange. The lowest curve in the graph is chosen for further analysis as it represents the least favourable scenario.

9 Conclusion and recommendations

9.1 Conclusion

The influence of PIR insulation on the transverse distribution of small surface loads on corrugated steel roofing sheets is a critical aspect of understanding the behaviour roofing systems. Through a series of experiments and numerical models, various factors affecting load distribution have been investigated. In examining the main question regarding the influence of PIR insulation on load distribution, it has been established that the presence of PIR insulation significantly affects how small surface loads are distributed across the roofing sheets. The insulation layer plays a key role in distributing the load among multiple ribs.

To address the first question on the variables affecting load distribution in the presence of PIR insulation, several factors have been identified. The span of the roofing sheets is a crucial variable, as changes in the span length from 2 to 6 meters can result in noticeable alterations in load distribution. Expanding the span from 2 to 6 meters with a single mid-span surface load (load case B) increases the adjacent rib contribution by 20%, meaning that their normalized strain values relative to the load location's maximum strain grow by 20% in the elastic phase. The rigidity of the steel sheet at the load location also plays a significant role, with adjacent ribs to the load location contributing more significantly to load distribution in cases where steel rigidity is reduced but still within the elastic phase. Moreover, the location and magnitude of applied loads, as well as the presence of multiple load locations on the PIR insulation, are essential variables influencing load distribution.

Regarding the distribution angle of the load in the PIR insulation (second question), numerical models suggest a shear stress distribution angle of approximately 32.7 degrees for the elastic PIR insulation layer. However, it is essential to consider that experimental setups demonstrate varying angles of failure for the PIR insulation for load case B, ranging from 18 to 44 degrees, due to shear stresses and the development of cracks caused by imperfections in the PIR. The angle of failure of load case A is equal to 39 degrees.

Finally, the third question relates to the failure criteria and the failure load of the roof structure. The experiments reveal that the failure mode of the roof structure is primarily governed by the rupture of the PIR insulation, which occurs before any yielding in the steel sheet. The experiments show yielding of the steel at 7300 N after the loading jack ruptures the PIR and reaches the steel (load case B). The non-linear numerical models show that the ultimate load is found to be 8000 N when a single surface load (load case B) is applied directly on the steel sheet. For design purposes, it is recommended not to factor in scenarios involving PIR insulation for loads exceeding the 6250 N limit, because this is the load where damage appears in the PIR when it is tested in compression.

In conclusion, PIR insulation significantly impacts the transverse distribution of small surface loads on corrugated steel roofing sheets. It provides design flexibility, leading to a more realistic distribution of applied loads among multiple ribs. The variables affecting load distribution include span length, steel rigidity, location, and magnitude of applied loads. The distribution angle of the load in the PIR insulation varies depending on the specific conditions and loading scenarios. Lastly, the failure criteria for the roof structure are primarily associated with the rupture of the PIR insulation, which occurs prior to yielding in the steel sheet. Understanding these aspects is crucial for ensuring the safety and structural integrity of roofing systems with PIR insulation, allowing for informed design and implementation decisions.

9.2 Recommendations

Further research can explore various approaches to improve the accuracy of the steel sheet results, such as considering different initial imperfections in the geometry. This can be done in the form of different assumptions such as the use of buckling mode shapes that are obtained from vertical loads instead of axial loads. Additionally, investigating the behaviour of the PIR insulation when the span is increased would provide insights into whether the rupture of the PIR still governs before yielding of the steel. Conducting large-scale experiments on bigger spans would be beneficial for this purpose. Furthermore, further research can focus on examining the relationship between the angle of failure of the PIR due to punching shear failure and the shear stresses in both the elastic and non-elastic phases. In the nonlinear analysis, this study assumed the PIR insulation to be linear elastic. Future research can investigate the feasibility of incorporating the actual material properties of the PIR insulation and simulating the presence of cracks, which would allow for a more accurate representation of load transfer to the steel sheet.

10 Appendix

10.1 Appendix A: Force vs Strains (First experiment – Load case A)

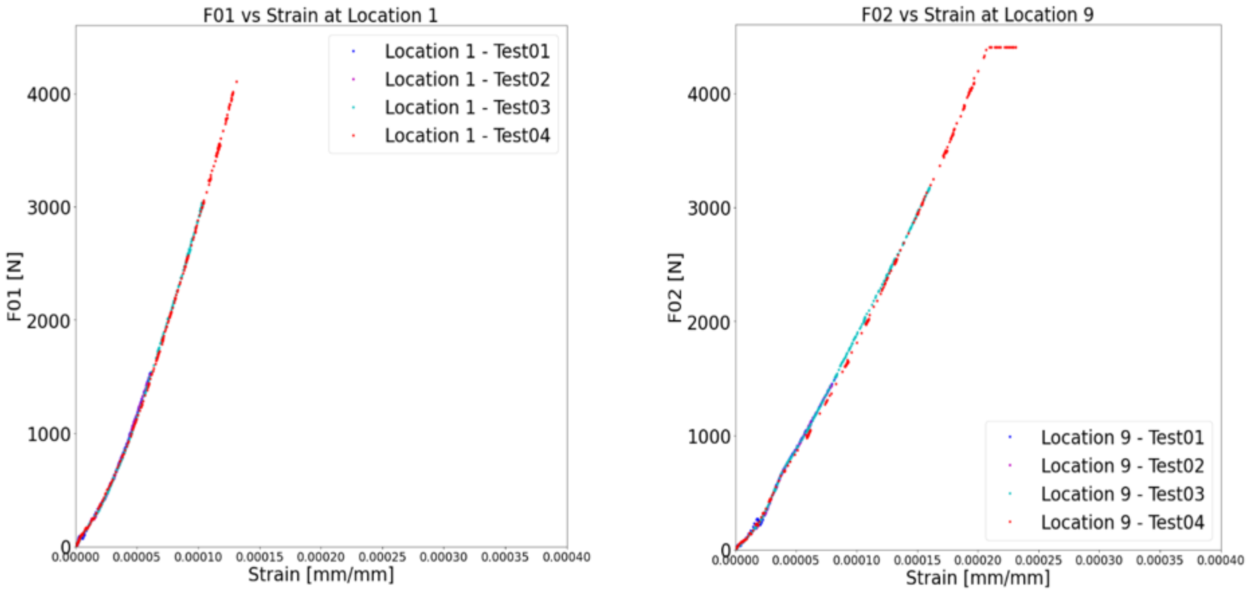

Figure 76 Strains at locations (1 & 9) – LCA.

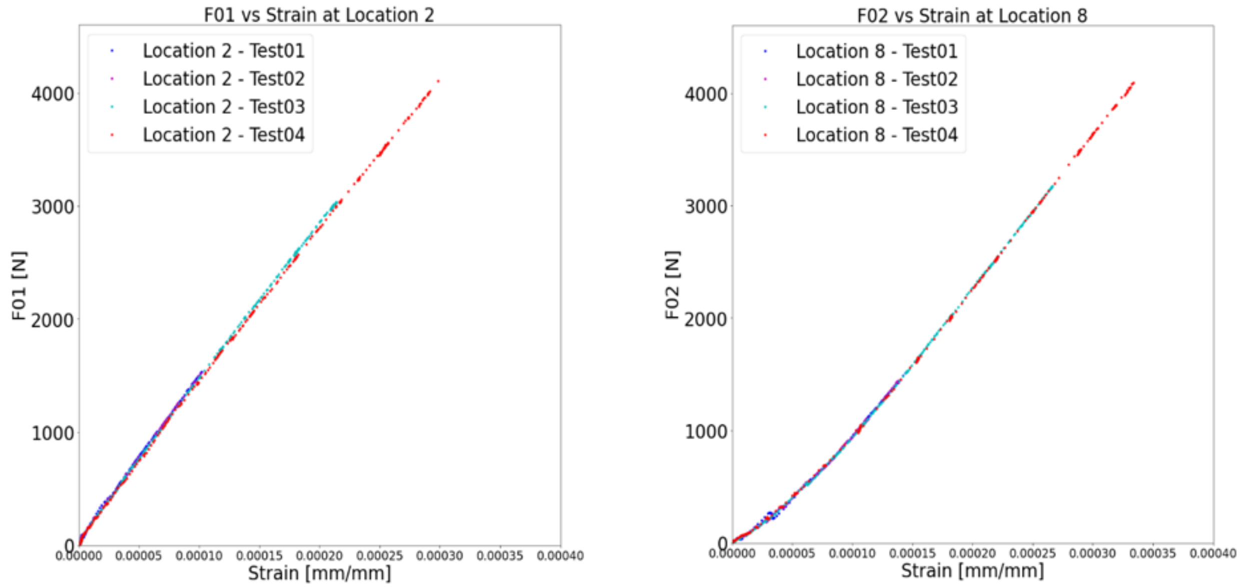

Figure 77 Strains at locations (2 & 8) – LCA.

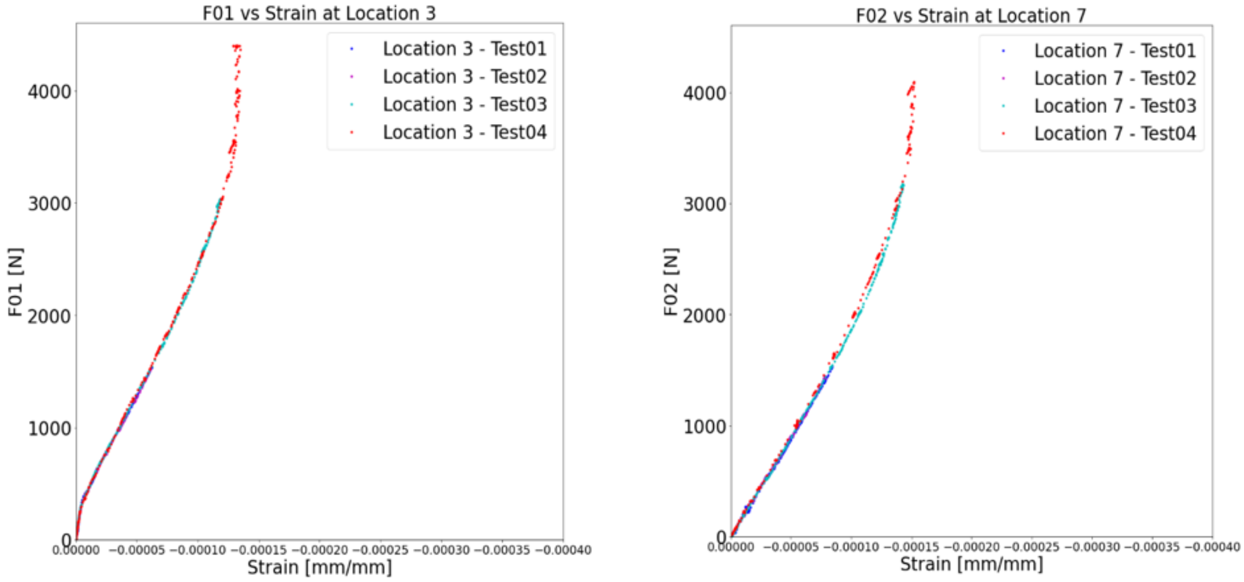

Figure 78 Strains at locations (3 & 7) – LCA.

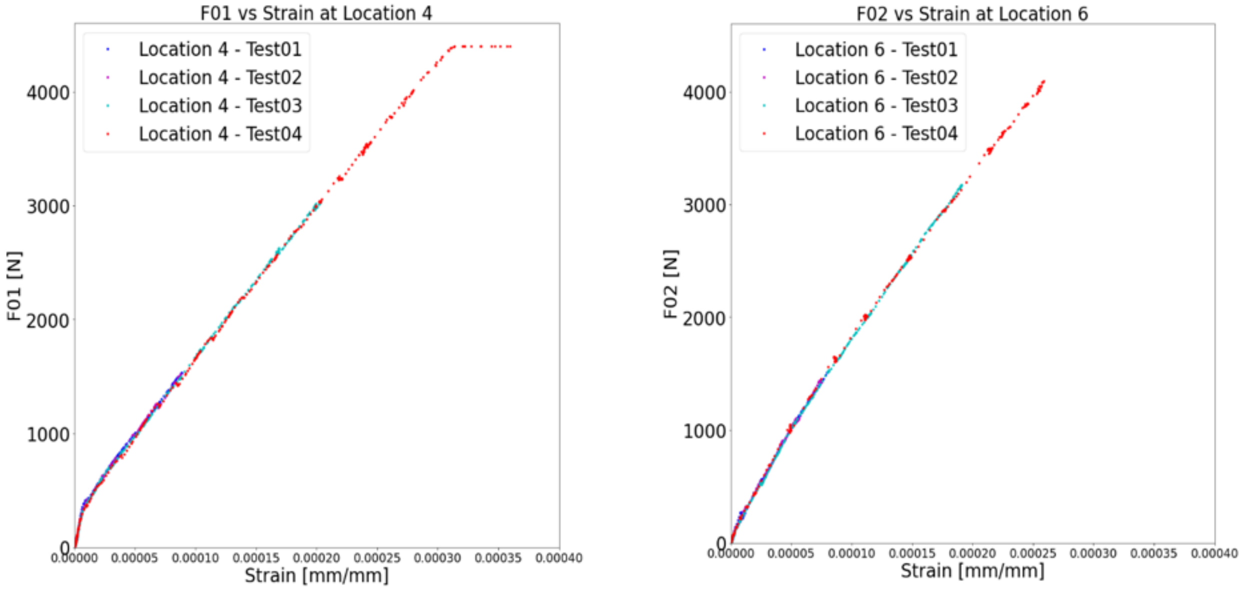

Figure 79 Strains at locations (4 & 6) – LCA.

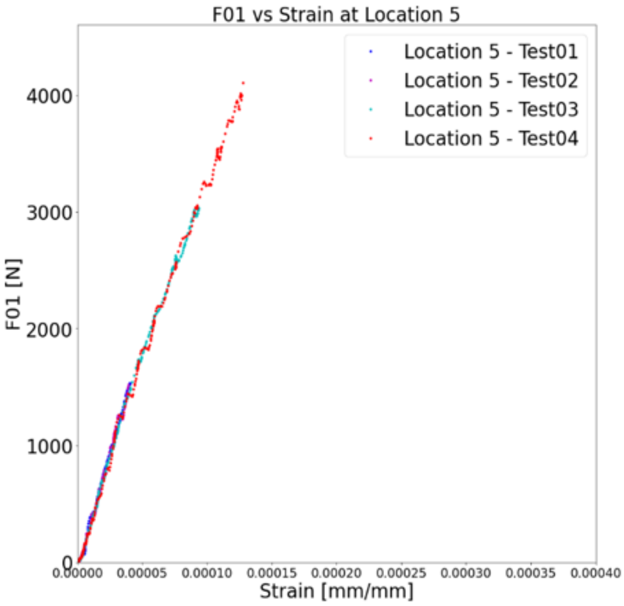

Figure 80 Strains at location (5) – LCA.

10.2 Appendix B: Force vs Strains (Second experiment – Load case B)

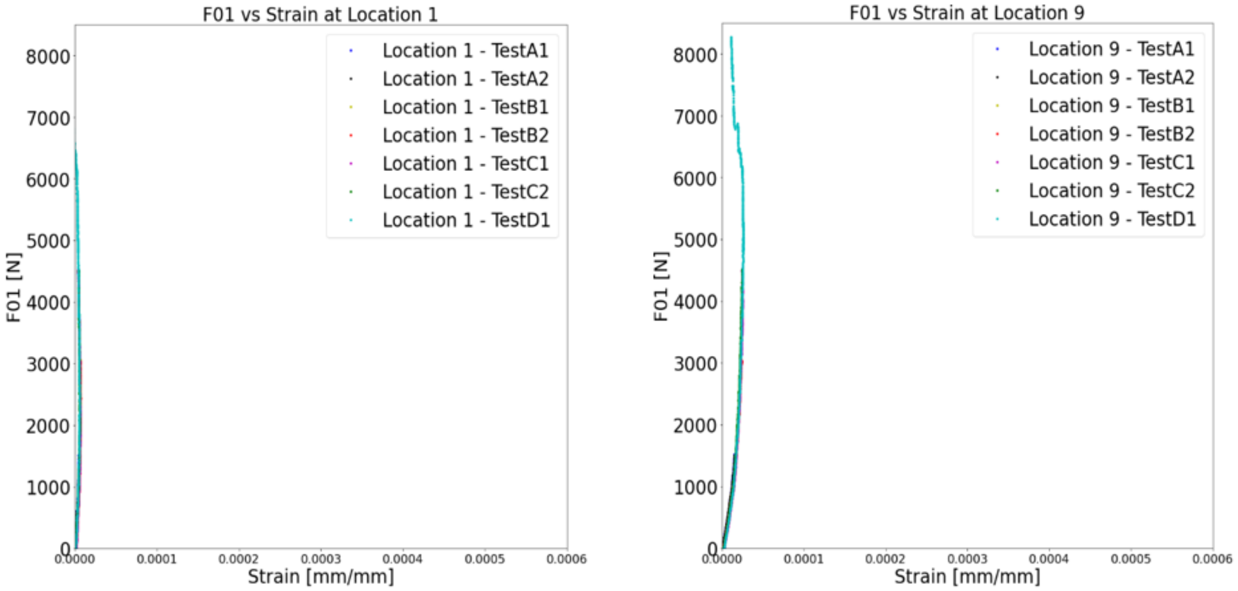

Figure 81 Strains at locations (1 & 9) – LCB.

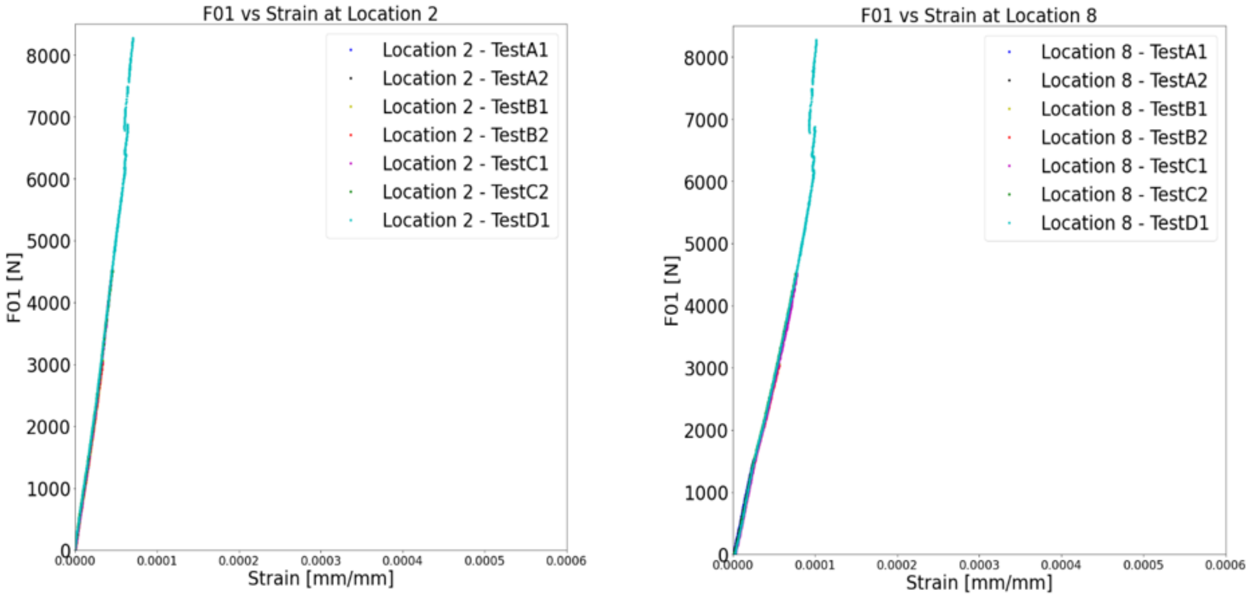

Figure 82 Strains at locations (2 & 8) – LCB.

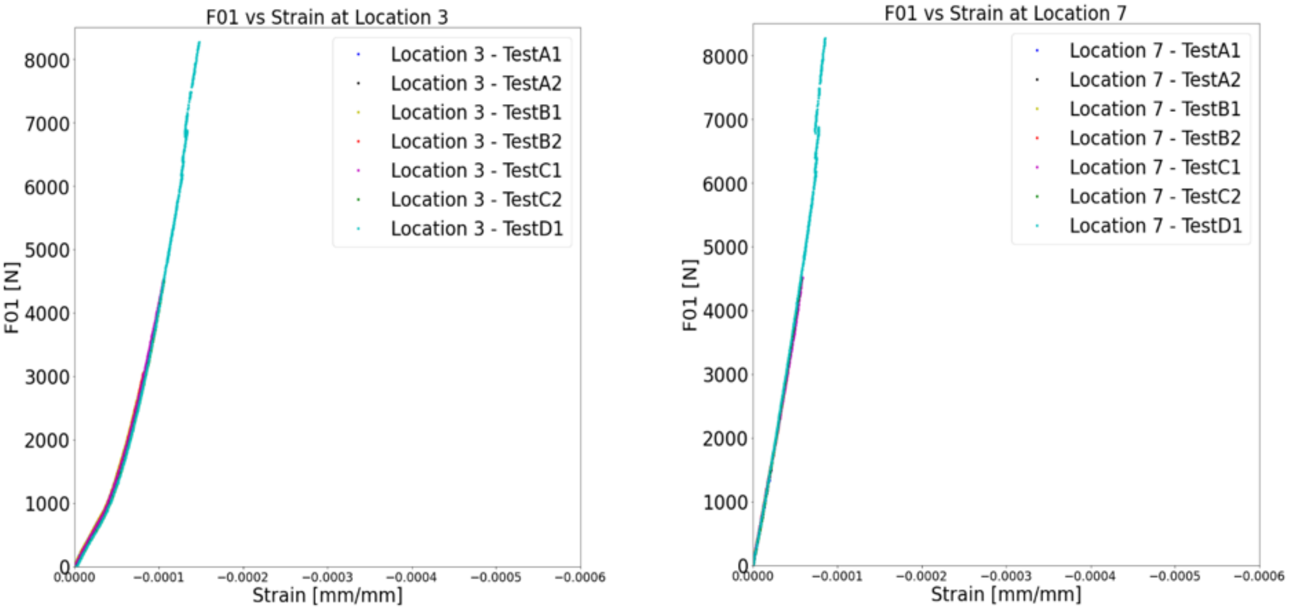

Figure 83 Strains at locations (3 & 7) – LCB.

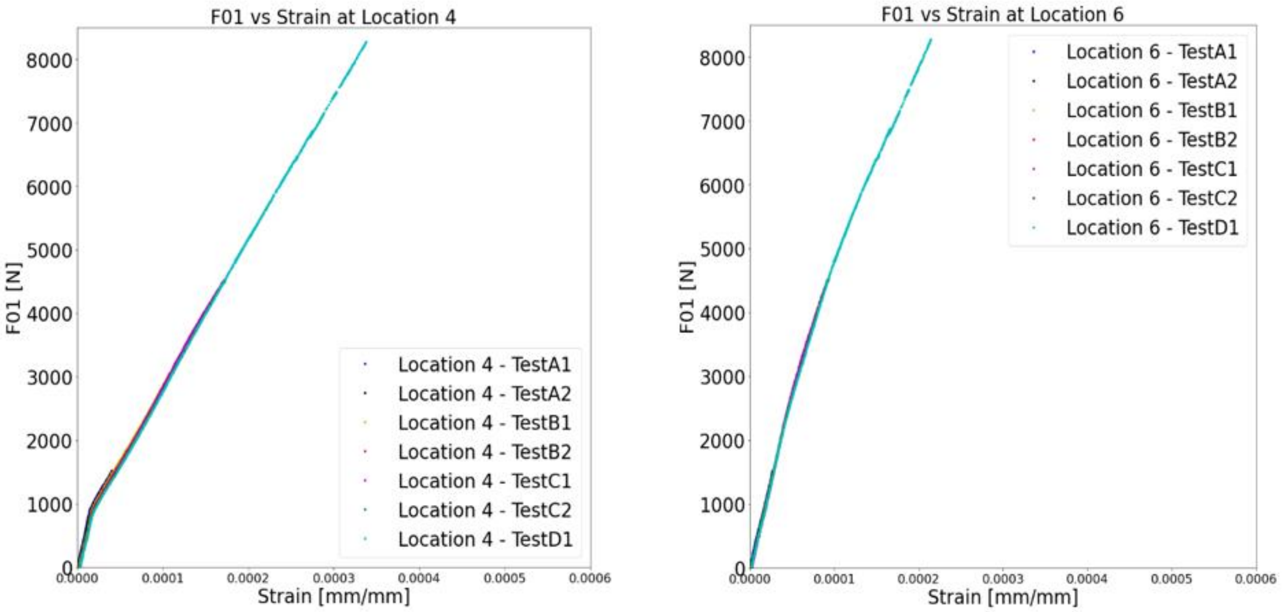

Figure 84 Strains at locations (4 & 8) – LCB.

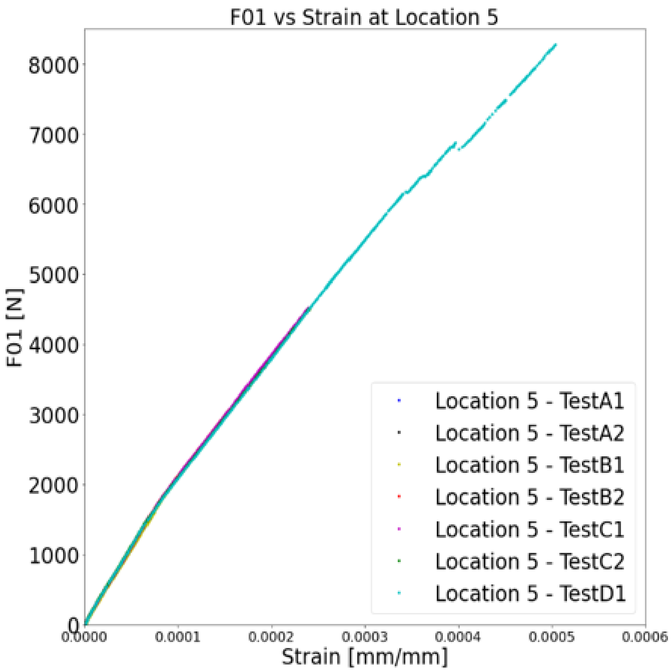

Figure 85 Strains at location (5) – LCB.

10.3 Contour plots

10.3.1 Load case A

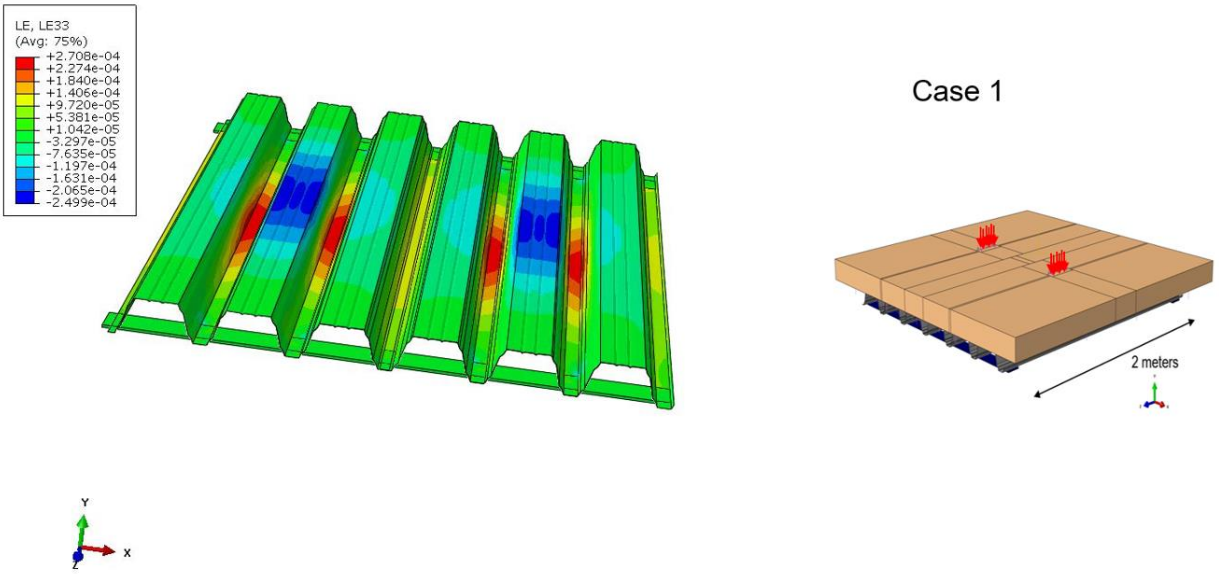

*Figure 86 Longitudinal strains (z direction): Load case A, span = 2 m, load = 2*4 kN.*

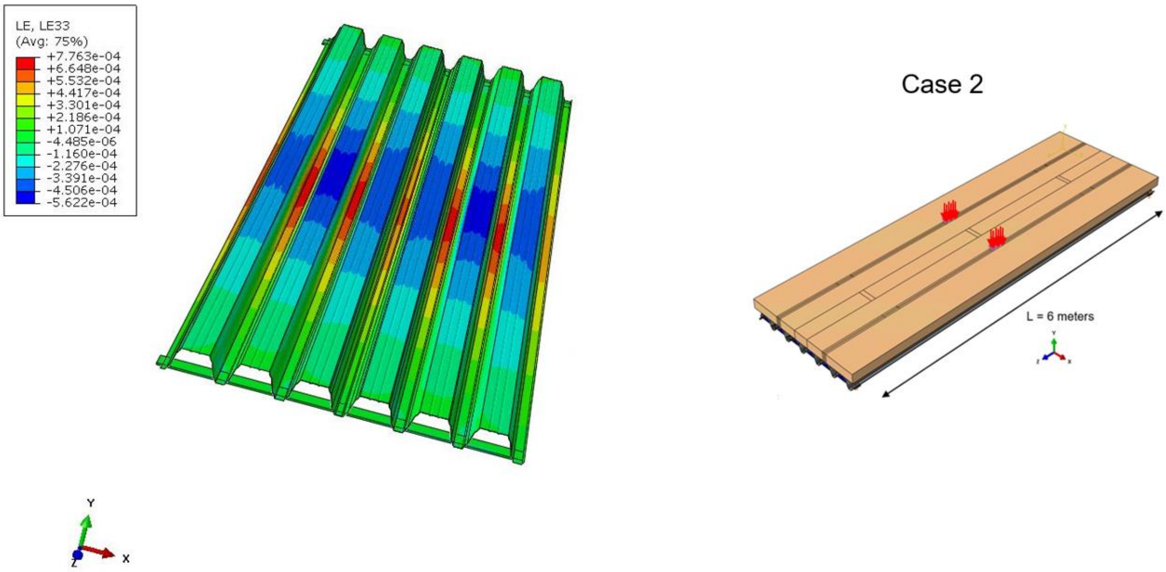

*Figure 87 Longitudinal strains (z direction): Load case A, span = 6 m, load = 2*4 kN.*

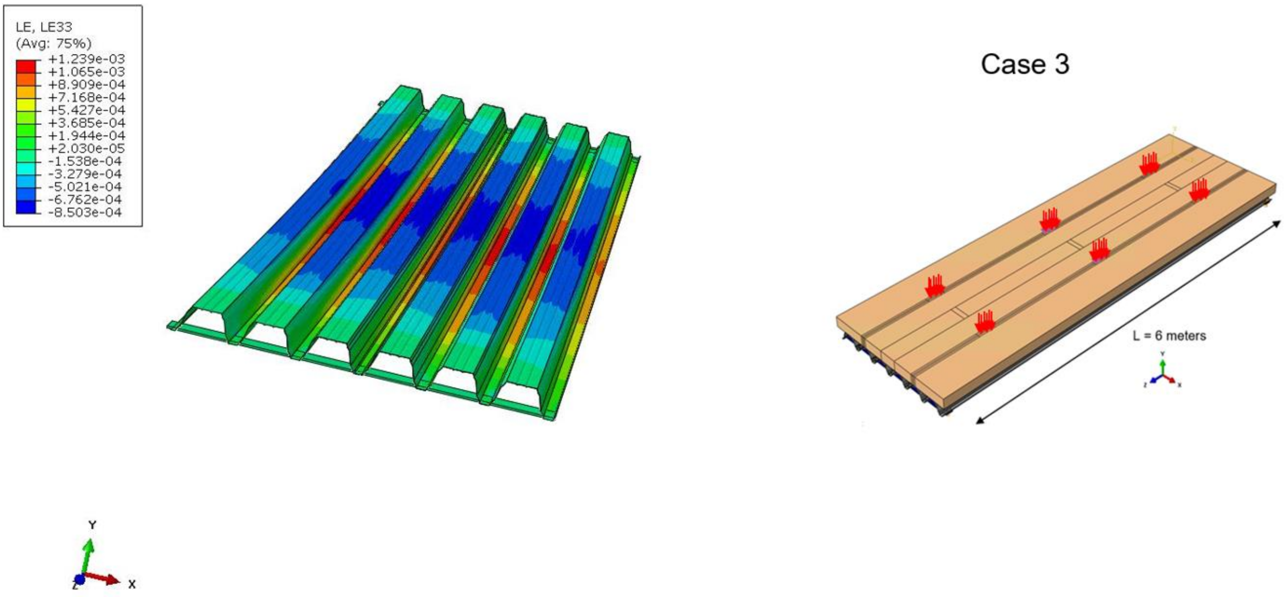

*Figure 88 Longitudinal strains (z direction): Load case A, span = 6 m, load = 3*2*4 kN.*

10.3.2 Load case B

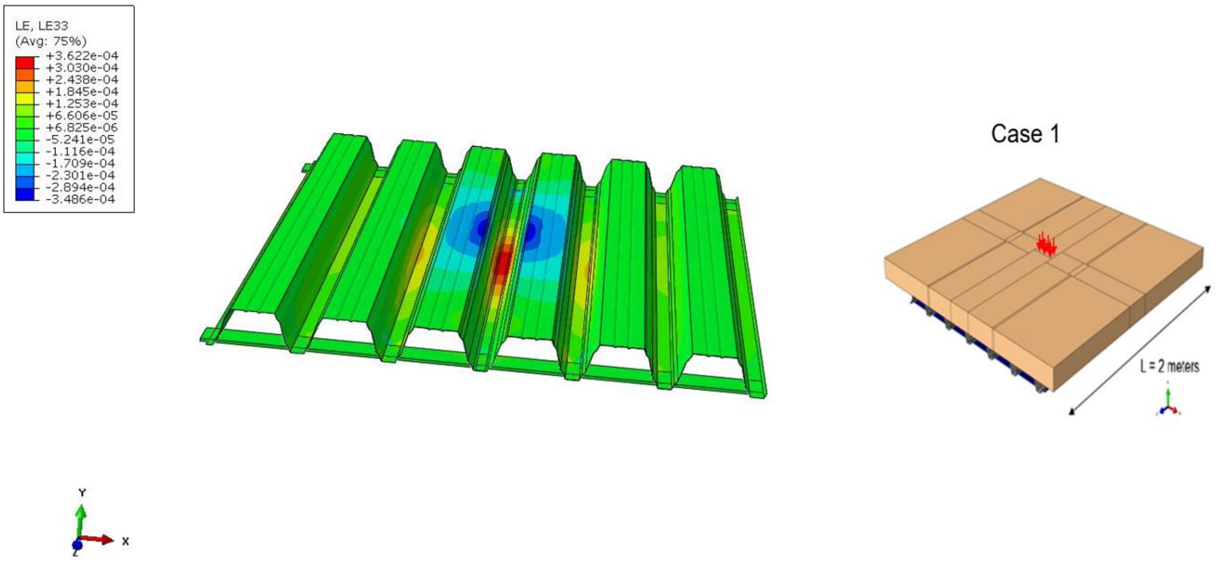

Figure 89 Longitudinal strains (z direction): Load case B, span = 2 m, load = 6 kN.

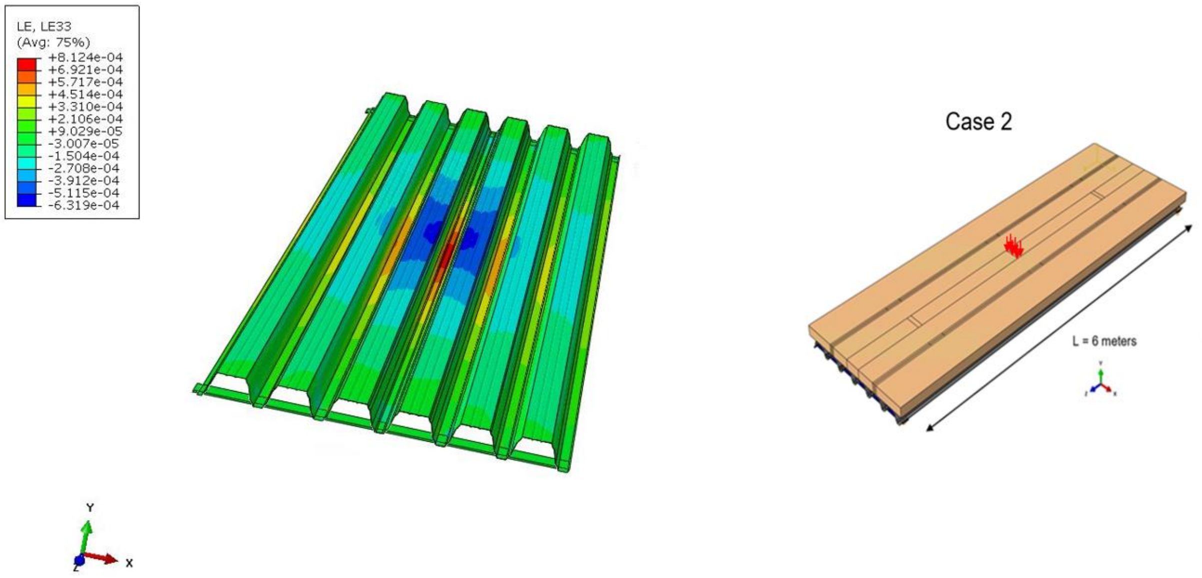

Figure 90 Longitudinal strains (z direction): Load case B, span = 6 m, load = 6 kN.

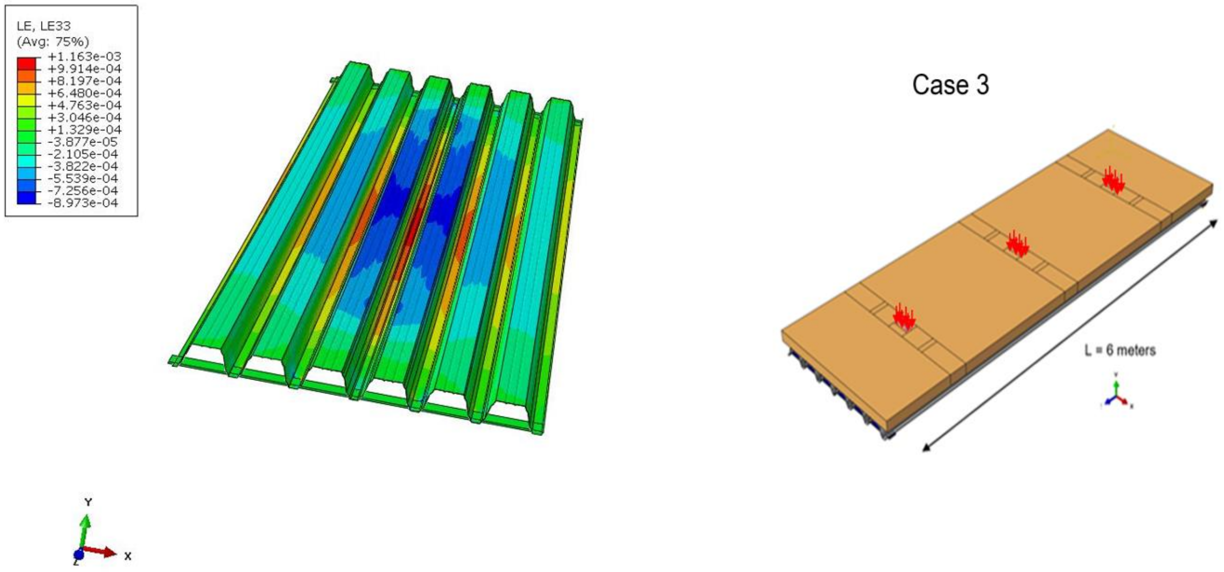

*Figure 91 Longitudinal strains (z direction): Load case B, span = 6 m, load = 3*6 kN.*

List of Figures and Tables

Bibliography

Geim, A. K., & ter Tisha, H. A. M. S. (2001). Detection of earth rotation with a diamagnetically levitating gyroscope. Physica B: Condensed Matter, 294–295, 736.

Dutch Solar Quarterly. (2021). Q4 2020. Retrieved from https://www.solarquarterly.nl/wp-content/uploads/2021/03/SolarQuarterly-2021-Q1-Q4-2020-Engels.pdf.

European Commission. (2020). Communication from the Commission to the European Parliament, the European Council, the Council, the European Economic and Social Committee and the Committee of the Regions: A European Climate Law. Retrieved from https://ec.europa.eu/clima/policies/eu-climate-action/law_en.

International Energy Agency. (2021). Solar PV in the Netherlands. Retrieved from https://www.iea.org/reports/solar-pv-in-the-netherlands.

Ministry of Economic Affairs and Climate Policy. (2020). The Dutch Climate Agreement. Retrieved from https://www.government.nl/topics/climate-change/contents/the-dutch-climate-agreement.

Zhang, H., Fang, W., Li, Y., & Tao, W. (2017). Experimental study of the thermal conductivity of polyurethane foams. Applied Thermal Engineering, 115, 528-538. https://doi.org/10.1016/j.applthermaleng.2016.12.057

Lau, S. C. W. (1988). Distortional buckling of thin-walled columns. (Doctoral dissertation). University of Sydney, Sydney, Australia.

Key, P. W., & Hancock, G. J. (1993). A theoretical investigation of the column behaviour of cold-formed square hollow sections. Thin-walled Structures, 16(1/4), 31–64.

Schafer, B. W., & Pekoz, T. (1997). Computational modelling of cold-formed steel: characterizing geometric imperfections and residual stresses. Journal Title, 47, 193–210.

Vitkauskiene. (2011). Retrieved from https://www.scopus.com/record/display.uri?eid=2-s2.0-80052744557&origin=inward

Cabulis, U., Sevastyanova, I., Anderson, J., & Beverte, I. (2014). Rapeseed oil-based rigid polyisocyanurate foams modified with nanoparticles of various types. Polimery, 59, 207-212. Retrieved from http://polimery.ichp.vot.pl/index.php/p/article/view/625.

Al Nabulsi, A., Cozzula, D., Hagen, T., Leitner, W., & Müller, T. E. (2018). Isocyanurate formation during rigid polyurethane foam assembly: a mechanistic study based on in situ ir and nmr spectroscopy. Polym. Chem., 9, 4891-4899. Retrieved from https://www.sciencedirect.com/science/article/pii/S0142941820321942#bib6.

Czupryński, B., Paciorek-Sadowska, J., & Liszkowska, J. (2009). Properties of rigid polyurethane-polyisocyanurate foams modified with the selected fillers. Journal of Applied Polymer Science. Retrieved from https://onlinelibrary.wiley.com/doi/10.1002/app.30937.

Figueira. (2019). Influence of service temperature on shear creep behaviour of a rigid low-density closed-cell PIR foam. Journal Title. Retrieved from https://www.sciencedirect.com/science/article/pii/S0950061819320227.

Wenberg, J., & Stichel. (2011). Orthotropic Models of Corrugated Sheets in Finite Element Analysis. Retrieved from https://www.researchgate.net/publication/258403300_Orthotropic_Models_of_Corrugated_Sheets_in_Finite_Element_Analysis

Tuwair, H., & Hopkins, M. (2015). Evaluation of sandwich panels with various polyurethane foam-cores and ribs. Journal of Materials Processing Technology. Retrieved from https://www.sciencedirect.com/science/article/abs/pii/S1359836815002619.